# SPATIAL VARIATIONS IN THE MECHANICAL PROPERTIES OF THE THORACIC AORTA

By

Jungsil Kim

#### A DISSERTATION

Submitted to Michigan State University in partial fulfillment of the requirements for the degree of

#### DOCTOR OF PHILOSOPHY

Mechanical Engineering

2011

#### ABSTRACT

## SPATIAL VARIATIONS IN THE MECHANICAL PROPERTIES OF THE THORACIC AORTA

By

#### Jungsil Kim

Cardiovascular disease (CVD) is the leading cause of death in the United States and a major cause of disability worldwide. A common type of vascular diseases in the U.S. is aortic aneurysm. Surgical interventions, such as open surgery or endovascular aneurysm repair (EVAR), are often required to avoid the high risk associated with aneurysm rupture. To better understand the role of biomechanics in aortic diseases and develop their clinical interventions, there is a need to understand the mechanical behavior of healthy as well as diseased aortas and their effects on aneurysm expansion and rupture potential. While it is well known that the mechanical properties of a blood vessel vary with location and age, little attention has been paid to its circumferential variations. Therefore, the goal of this study is to investigate spatial variations in the mechanical behavior of the descending thoracic aorta. Toward this end, the following has been accomplished: 1) a biaxial experimental apparatus with a stereo-vision system, which allows us to track the three-dimensional (3D) motion of the aorta during the inflation test, was developed, 2) the inflation tests at fixed longitudinal stretch ratios were performed for two longitudinal portions – the proximal and distal – and four circumferential regions – the anterior, left lateral, posterior, and right lateral – of the porcine thoracic aorta, 3) stress-strain analysis were developed based on the approximation of the aortic wall surface using a set of continuous base functions in a curvilinear coordinate system, 4) the variations of stretch, stress, stiffness defined as a change in the circumferential stress corresponding to a change in the circumferential stretch, and pressure-strain elastic modulus were statistically analyzed, and 5) material parameters were estimated by a parameter estimation method using a constitutive model based on the constrained mixture approach.

The experimental results showed that the posterior region was much stiffer than the anterior region. However, the physiological stiffness represented by the pressure-strain elastic modulus did not show a significant difference among the circumferential regions for the proximal and distal portions of the thoracic aorta. In addition, the stress showed a significant difference among the circumferential regions, and the stretch was relatively uniform. In the parameter estimation, material parameters of elastin and collagen were dominant in the mechanical response, but the role of the smooth muscle seemed to be insignificant. A significant difference was found in the parameters of the elastin and collagen fiber between the anterior and posterior regions.

In conclusion, this study presents an experimental method and analysis to measure local deformation of a blood vessel. Furthermore, it shows that there exists consistent spatial variations in the mechanical properties of the thoracic aorta. These findings increase our understanding of vascular mechanics and adaptation, and will eventually help to improve clinical treatments and interventions of vascular diseases.

# **Table of Contents**

$\mathbf{Li}$	st of	Figures
1	INT	RODUCTION
	1.1	Anatomy and histology of the aorta
	1.2	Mechanical behavior of the aorta
	1.3	Variation and heterogeneity of the mechanical behavior of the aorta
	1.4	Experimental characterization of mechanical behavior of the aorta
	1.5	Objective of this study
<b>2</b>	EX	PERIMENTAL METHODS
	2.1	Experimental apparatus
		2.1.1 Calibration of sensors
	2.2	Specimen preparation
	2.3	Test protocol
	2.4	Marker tracking and 3D position reconstruction
		2.4.1 Calibration of cameras
		2.4.2 Image processing
		2.4.3 Marker tracking
		2.4.4 3D position reconstruction
	2.5	Histology sample preparation
3	BIC	MECHANICAL ANALYSIS
	3.1	Kinematics in curvilinear coordinate systems
	3.2	Numerical analysis and approximation
		3.2.1 Coordinate transformation
		3.2.2 Deformation gradient
		3.2.3 Approximation of the surface
		3.2.4 Least squares estimation
	3.3	Thickness of the aortic wall
	3.4	Curvature of the aortic wall
	3.5	Stress and strain analysis
	3.6	Statistical analysis
1	CO	NSTITUTIVE RELATIONS AND PARAMETERS

	4.1	Constitutive relations	
		4.1.1 Constitutive models	
		4.1.2 Parameter estimation	
5	RES	SULTS AND DISCUSSION	
	5.1	Validation of the experimental measurements	
	5.2	Validation of the approximation using continuous functions	
	5.3	Variation of the aortic wall thickness	
	5.4	Radius of curvature of the aortic wall	
	5.5	Stress and strain relationship of the aorta	
	5.6	Circumferential variation in the stiffness	
	5.7	Longitudinal variation in the mechanical behavior of the aorta 69	
	5.8	Material parameters	
	5.9	DISCUSSION	
		5.9.1 Nonlinear, anisotropic behavior of the aorta	
		5.9.2 Variation in stiffness	
		5.9.3 Heterogeneous composite of the aorta	
		5.9.4 Relation of heterogeneous mechanical properties with pathological con-	
		ditions	
		5.9.5 Material parameters	
		5.9.6 Limitation of this study	
6	CON	NCLUSION	
U	COI	NOLOGION	
$\mathbf{A}_{]}$	ppend	dices	
$\mathbf{A}$	Met	hods	
	A.1	Camera matrix	
В	Ana	dysis	
	B.1	Derivatives of the parameters for the curvature	
		B.1.1 Reference Configuration	
		B.1.2 Current Configuration	
	B.2	Gaussian quadrature	
$\mathbf{C}$	D	100	
$\mathbf{C}$			
		Information of the aorta sample	
	C.2	Stress-stretch plots	
		Stretch, stress, and stiffness	
	C.4	Material parameters	
Bi	hliog	raphy 126	

# List of Tables

5.1	The mean and standard deviation of material parameters for all aorta samples	71
C.1	Information of all aorta samples	106
C.2	The mean and the standard deviation of the circumferential stretch of the thoracic aorta at the transmural pressure of 8.00 kPa (60 mm Hg), 12.00 kPa (90 mm Hg), and 16.00 kPa (120 mm Hg) for each proximal circumferential region	118
C.3	The mean and the standard deviation of the circumferential stress of the thoracic aorta at the transmural pressure of 8.00 kPa, 12.00 kPa, and 16.00 kPa for each proximal circumferential region (unit: kPa)	119
C.4	The mean and the standard deviation of the circumferential stiffness of the thoracic aorta at the transmural pressure of 8.00 kPa, 12.00 kPa, and 16.00 kPa for each proximal circumferential region (unit: kPa)	120
C.5	The mean and the standard deviation of the pressure-strain elastic modulus of the proximal and distal portions of the thoracic aorta for each proximal circumferential region (unit: kPa)	121
C.6	Material parameters for the sample 1	122
C.7	Material parameters for the sample 2	122
C.8	Material parameters for the sample 3	123
C.9	Material parameters for the sample 4	123
C.10	Material parameters for the sample 5	123
C.11	Material parameters for the sample 6	124
C.12	Material parameters for the sample 7	124
C.13	Material parameters for the sample 8	124

C.14 Material parameters for the sample 9		 •							125
C.15 Material parameters for the sample 10									125
C.16 Material parameters for the sample 11								 •	125

# List of Figures

1.1	Anatomy of the aorta. (For interpretation of the references to color in this and all other figures, the reader is referred to the electronic version of this dissertation)	ç
1.2	Schematic cross section of the wall of an elastic artery. Adapted from (Rhodin, 1980)	4
1.3	Histology of the cross-section of the aorta (a) and its small section stained with hematoxylin and eosin (H & E) (b), Verhoeff-Van Gieson (VVG) (c), picrosirius red (d), and the polarized image of picrosirius red stain (e)	Ę
1.4	Typical stress-strain curves of a circumferential strip of an artery during the uniaxial test (Holzapfel et al., 2000)	6
2.1	Schematic diagram of the experimental set-up for the extension-inflation test.	18
2.2	Schematics of the experimental device	19
2.3	Schematics of the test chamber to show calculation of the transmural pressure	20
2.4	Two camera set-up	21
2.5	Overview of the experimental process using the extension-inflation test device.	22
2.6	Schematic drawing of an upper cannula connector	23
2.7	A representative example for the linear least squares regression of load cell data (a) and pressure transducer data (b)	24
2.8	(a) The porcine aorta sample from the thoracic to the abdominal, (b) the thoracic aorta with surrounding tissues, (c) the thoracic aorta after removing surrounding tissues, and (d) a cannulated aorta specimen with micro spheres	0.5
0.0	attached on the wall	25
2.9	Schematics of a world point and its corresponding image point	27
2.10	Calibration jig and camera set-up	28

2.11	An example of the processing to extract the position of markers in pixel. (a) the entire image, (b) the masked image, and (c) thresholded image	30
2.12	Stereo images from left side camera (a) and right side camera (b), and the reconstructed marker positions in 3D (c)	31
3.1	The surfaces in the reference configuration and the deformed configuration are approximated by continuous functions of two variables, $\overline{\Theta}$ and $\overline{S}$ , convected to the surface. The deformation gradient of the surface corresponding to the mapping is denoted by $\mathbf{F}$	37
3.2	Free body diagram of membrane tissue	44
3.3	(a) Free body diagram of a blood vessel sample during the inflation test and (b) the cross-section of the aortic wall	46
5.1	Comparison of stretch-stress plots before and after the rotation of a specimen.  A: anterior region, L: left lateral region, P: posterior region, and R: right lateral region	58
5.2	Comparison of the distribution of circumferential stretch between two methods: (a) stretch distribution by linear approximation with triangular elements and (b) stretch distribution by the approximation in the present study. Black dots represent markers in the deformed configuration	59
5.3	Mean and standard deviation of the aortic wall thickness along the circumference: (a) the proximal thoracic aorta, (b) the distal thoracic aorta. 0°: the anterior region, 90°: left lateral region, 180°: posterior region, and 270°: right lateral region	61
5.4	A representative example of the distributions of the radius of curvature for the four circumferential regions of one thoracic aorta sample at transmural pressures of 8.00 kPa (60 mm Hg), 12.00 kPa (90 mm Hg), and 16.00 kPa (120 mm Hg), respectively, and a longitudinal stretch ratio ( $\Lambda_Z$ ) of 1.35	62
5.5	A representative example of the five repeated loading and unloading curves of the anterior region of the thoracic aorta	63
5.6	A representative example of the distributions of circumferential stretch for the four circumferential regions of one thoracic aorta sample at transmural pressures of 8.00 kPa, 12.00 kPa, and 16.00 kPa, respectively, and a longitudinal stretch ratio ( $\Lambda_Z$ ) of 1.35	64

5.7	A representative example of the distributions of longitudinal stretch for the four circumferential regions of one thoracic aorta sample at transmural pressures of 8.00 kPa, 12.00 kPa, and 16.00 kPa, respectively, and a longitudinal stretch ratio ( $\Lambda_Z$ ) of 1.35	65
5.8	A representative example of the circumferential Cauchy stress and circumferential stretch curve (a) and the longitudinal stress and circumferential stretch curve (b) at a longitudinal stretch ratio $(\Lambda_Z)$ of 1.35	66
5.9	A representative example of the circumferential stiffness and transmural pressure curve at a longitudinal stretch ratio $(\Lambda_Z)$ of 1.35	67
5.10	Comparison of the mean circumferential stretch of the proximal thoracic aorta at the transmural pressure of 12.00 kPa for each longitudinal stretch ratio $(\Lambda_Z)$ .	68
5.11	Comparison of the mean circumferential Cauchy stress of the proximal thoracic aorta aat the transmural pressure of 12.00 kPa for each longitudinal stretch ratio ( $\Lambda_Z$ ). Asterisk represents the significant difference (*: p<0.05, **: p<0.01, ***: p<0.005)	78
5.12	Comparison of the mean circumferential stiffness of the proximal thoracic aorta among the four circumferential regions at the transmural pressure of 12.00 kPa for each longitudinal stretch ratio $(\Lambda_Z)$	79
5.13	Comparison of the mean pressure-strain elastic modulus of the proximal thoracic aorta at the transmural pressure of 12.00 kPa for each longitudinal stretch ratio $(\Lambda_Z)$	80
5.14	Comparison of the mean stretch at the anterior and posterior regions of the proximal and distal portions of the thoracic aorta at the transmural pressure of 12.00 kPa for each longitudinal stretch ratio $(\Lambda_Z)$	81
5.15	Comparison of the mean circumferential stress at the anterior and posterior regions of the proximal and distal portions of the thoracic aorta at the transmural pressure of 12.00 kPa for each longitudinal stretch ratio $(\Lambda_Z)$	82
5.16	Comparison of the mean circumferential stiffness at the anterior and posterior regions of the proximal and distal portions of the thoracic aorta at the transmural pressure of 12.00 kPa for each longitudinal stretch ratio $(\Lambda_Z)$	83
5.17	Comparison of the mean pressure-strain elastic modulus at the anterior and posterior regions of the proximal and distal portions of the thoracic aorta at the transmural pressure of 12.00 kPa for each longitudinal stretch ratio $(\Lambda_Z)$ .	84

5.18	a representative stress-stretch plot. Stress was calculated by using experimentally measured data and theoretically predicted. M: experimentally measured data, P: theoretically predicted data	85
5.19	Comparison of the mean and standard deviation of material parameter $c_1$ (a) and $c_2$ (b) among the four circumferential regions for the proximal thoracic aorta.	86
5.20	Comparison of the mean and standard deviation of material parameter $c_1$ (a) and $c_2$ (b) between the proximal and distal portions of the thoracic aorta.	87
A.1	Schematics of a world point and its corresponding image point	92
A.2	Image plane and pixel coordinate	93
C.1	Stress-stretch plots for the proximal thoracic aorta at a fixed stretch ratio of 1.35, 1.40, and 1.45 for sample 1	107
C.2	Stress-stretch plots for the proximal thoracic aorta at a fixed stretch ratio of 1.35, 1.40, and 1.45 for sample 2	108
C.3	Stress-stretch plots for the proximal thoracic aorta at a fixed stretch ratio of 1.35, 1.40, and 1.45 for sample 3	109
C.4	Stress-stretch plots for the proximal thoracic aorta at a fixed stretch ratio of 1.35, 1.40, and 1.45 for sample 4	110
C.5	Stress-stretch plots for the proximal thoracic aorta at a fixed stretch ratio of 1.35, 1.40, and 1.45 for sample 5	111
C.6	Stress-stretch plots for the proximal thoracic aorta at a fixed stretch ratio of 1.35, 1.40, and 1.45 for sample 6	112
C.7	Stress-stretch plots for the proximal thoracic aorta at a fixed stretch ratio of 1.35, 1.40, and 1.45 for sample 7	113
C.8	Stress-stretch plots for the distal thoracic aorta at a fixed stretch ratio of 1.35, 1.40, and 1.45 sample 8	114
C.9	Stress-stretch plots for the distal thoracic aorta at a fixed stretch ratio of 1.35, 1.40, and 1.45 sample 9	115
C.10	Stress-stretch plots for the distal thoracic aorta at a fixed stretch ratio of 1.35, 1.40, and 1.45 sample 10	116

C.11 Stress-stretch plots for the distal thoracic aorta at a fixed stretch ratio of	1.35,	
1.40, and 1.45 sample 11		117

## Chapter 1

## INTRODUCTION

Cardiovascular disease (CVD) is the leading cause of death in the United States and a major cause of disability worldwide. In 2007, CVD accounted for 33.6 percent of all deaths, and the direct and indirect cost of CVD was estimated at \$ 286.6 billion in the U.S. (American-Heart-Association, 2011). The high mortality rate of CVD has thus promoted the growth of research on cardiovascular mechanics. Vascular mechanics that has been developed based on continuum mechanics helps to understand the mechanical state of vascular tissue in various physiopathological conditions or in genetic disorders. Although understanding the biomechanics of the blood vessels has been greatly increased for the last three decades, the heterogeneity of vascular mechanics is still largely undisclosed and the state-of-the-art technique is not complete enough to explain regional difference in vascular behavior of either healthy and diseased arteries.

One of the most common types of vascular diseases in the U.S. is aortic aneurysm, an abnormal dilation of the aorta more than 3 cm in diameter (American-Heart-Association, 2011), which occurs mainly among the elderly (Walker et al., 1986). Aortic aneurysms are classified by the location where they occur: aortic root, thoracic, and abdominal aortic aneurysms. Abdominal aortic aneurysms (AAAs) are more common than thoracic aortic aneurysms, and the mortality rate of ruptured AAAs is up to 90% (American-Heart-Association, 2011).

Thus, the majority of studies of aortic aneurysms have been done on the abdominal aorta, and relatively few have focused on the thoracic aorta. Thoracic aortic aneurysms are also serious conditions due to the high risk of rupture, and they frequently occur concomitantly with other diseases such as atherosclerosis and Marfan syndrome (Isselbacher, 2005). The most severe disease of the aorta is aortic dissections, which are caused by a disruption or tear of the intimal layer, resulting in a separation in the aortic wall. Aortic dissections have a higher risk of mortality than thoracic aortic aneurysm and carry a high mortality rate, which increases 1 percent per hour unless patients find treatment within the first 24 hours (Cannon and O'Gara, 2006).

Surgical interventions, such as open surgery or endovascular repair, are often required to avoid the high risk associated with aneurysm rupture. The decision-making for surgical repair, however, depends mainly on physicians' clinical experience. In common practice, a surgical repair is recommended if the maximum diameter of the aneurysmal aorta exceeded a certain size (e.g., 5.5 cm for abdominal aortic aneurysms). In reality, however, some small aortic aneurysms still rupture even before reaching the critical size (Participants, 2002). Hence, the maximum diameter alone is not a sufficient indicator for the risk of rupture.

Abdominal aortic aneurysms grow faster in the anterior side, but their ruptures are found most in the posterolateral sides (Schwartz et al., 2007). It is rather suggested that mechanical failure is a local event and occurs when the local mechanical stress exceeds the local strength (Vorp et al., 1998). Therefore, there is a pressing need for understanding spatial variations in mechanical properties of healthy as well as diseased aortas and their effects on aneurysm expansion and rupture potential.

### 1.1 Anatomy and histology of the aorta

The aorta is the largest artery originating from the left ventricle of the heart and conveys oxygenated blood to organs and tissues of the body. It is generally classified into several

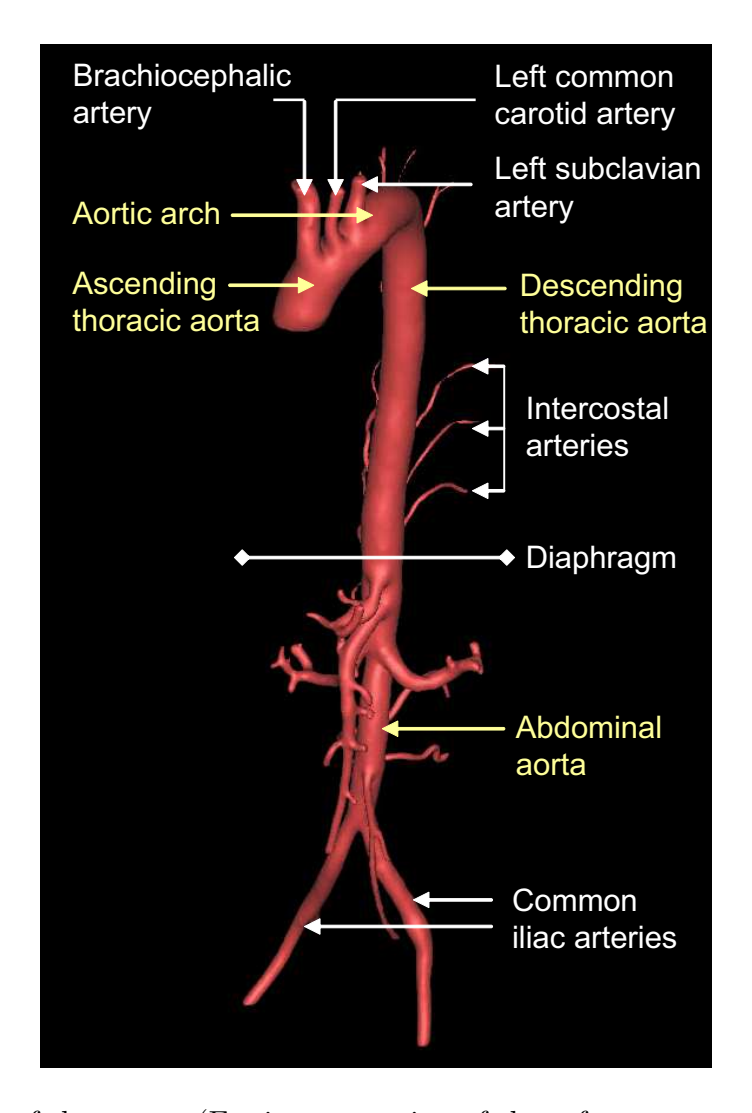


Fig. 1.1: Anatomy of the aorta. (For interpretation of the references to color in this and all other figures, the reader is referred to the electronic version of this dissertation).

portions: ascending aorta, aortic arch, and descending aorta, which is again divided to the thoracic aorta and the abdominal aorta. Fig. 1.1, which was reconstructed from magnetic resonance imaging (MRI) images, shows more detail anatomy of a human aorta. The descending thoracic aorta begins just beyond the aortic arch as the aorta bends down into the body and ends at the diaphragm. It is situated on the left side of the vertebral column, containing several intercostal arteries along its length, which provide blood to the chest area. In humans, the mean inner radius and wall thickness of the thoracic aorta are approximately 1.25 cm and 2 mm, respectively (Humphrey, 2001). Below the diaphragm, the abdominal

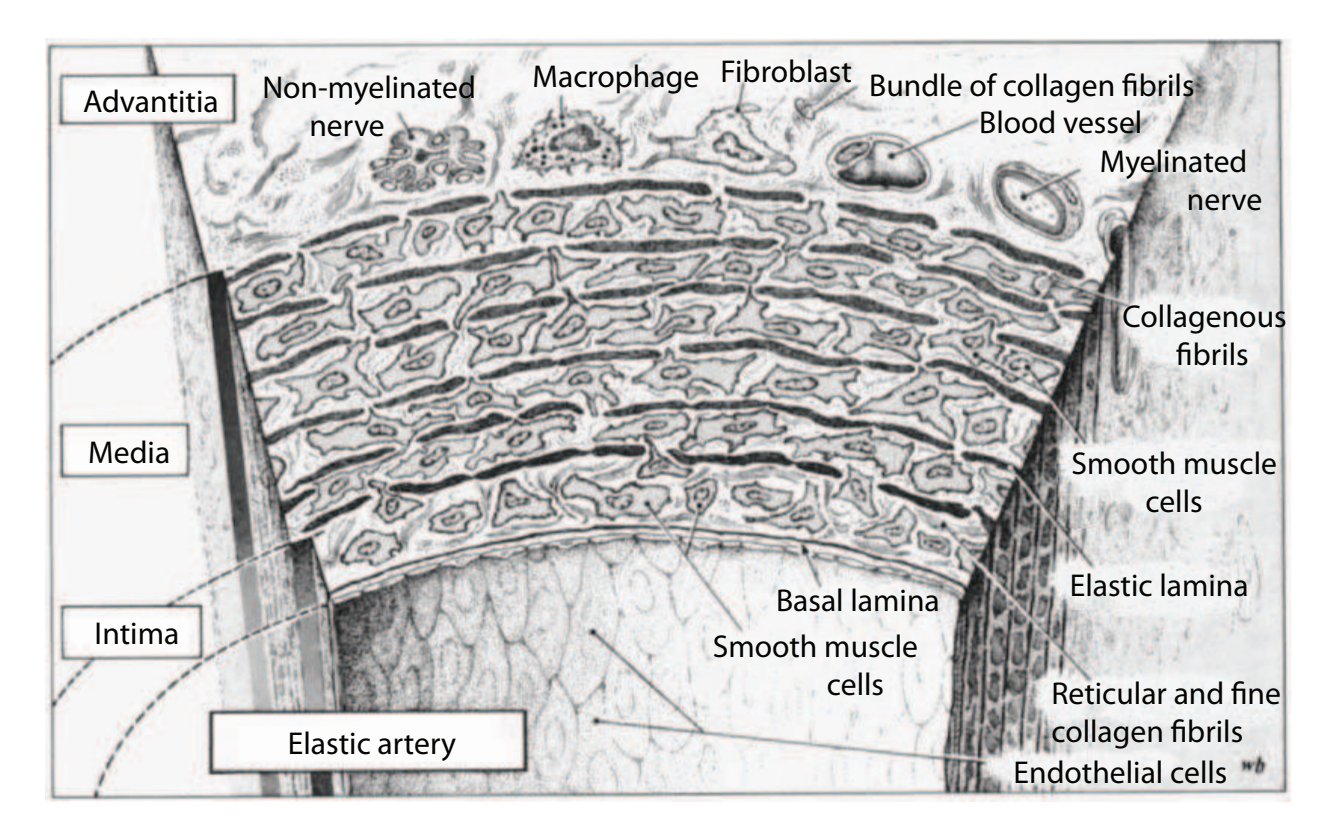


Fig. 1.2: Schematic cross section of the wall of an elastic artery. Adapted from (Rhodin, 1980).

aorta is located in front of the vertebral column, and it bifurcates into the left and right common iliac arteries. The abdominal aorta has several aortic branches, which include the celiac, superior mesenteric, inferior mesenteric, and renal arteries. The aorta becomes narrower in diameter as it separates into branches.

The aortic wall is composed of three distinct layers: the tunica intima, tunica media, and tunica adventitia (Fig. 1.2). The intima is the innermost layer of an aorta and consists of a layer of endothelial cells and a subendothelial layer of connective tissue. The internal elastic lamina separates the intima and the media. The media is the middle layer of concentrically-arranged smooth muscle cells, and contains collagen fibers and elastic fibers. The external elastic lamina separates the media and the adventitia. Finally, the adventitia is the outermost layer of an aorta and primarily composed of longitudinally arranged collagen fibers with elastin and fibroblasts. Compared with an elastic artery, an aorta consists of a thick media

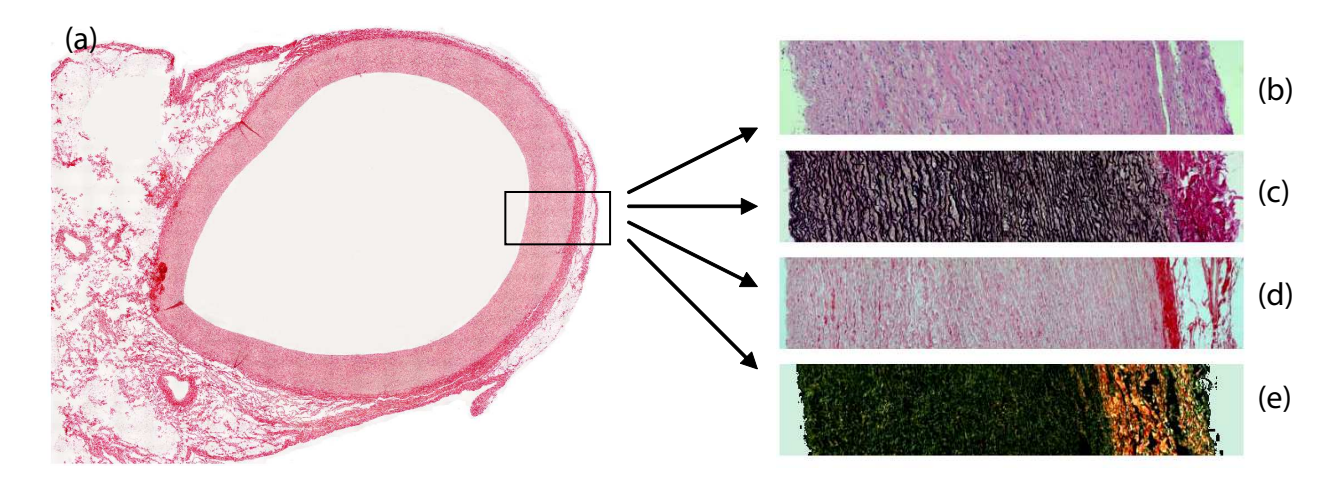


Fig. 1.3: Histology of the cross-section of the aorta (a) and its small section stained with hematoxylin and eosin (H & E) (b), Verhoeff-Van Gieson (VVG) (c), picrosirius red (d), and the polarized image of picrosirius red stain (e).

layer and a relatively thin adventitia layer (Fig. 1.3 (a)). The primary structural proteins of the aortic wall are collagen and elastin.

The cross-sectional histology of the aorta with different stains gives us the information of constituent as shown in Fig. 1.3. The entire aortic ring with surrounding tissue was stained with picrosirius red (Fig. 1.3 (a)), where collagen is colored red. Nuclei are blue with hematoxylin and eosin (H & E) stain (Fig. 1.3 (b)) so that cell density can be estimated. Verhoeff-Van Gieson (VVG) stain is common for examining the elastin because elastic fibers are colored black, and collagen is red (Fig. 1.3 (c)). In order to examine the orientation of collagen fibers, polarized light microscopy can be used (Fig. 1.3 (e)). The density of elastin lamellae varies throughout the aortic wall, and the adventitia layer has denser elastin lamellae than the media layer.

The microstructure of the aortic wall varies among species. The contents of the collagen and elastic tissue differ with regard to the portion of the aorta. In this study, we focus on the descending thoracic aorta and discuss it in detail.

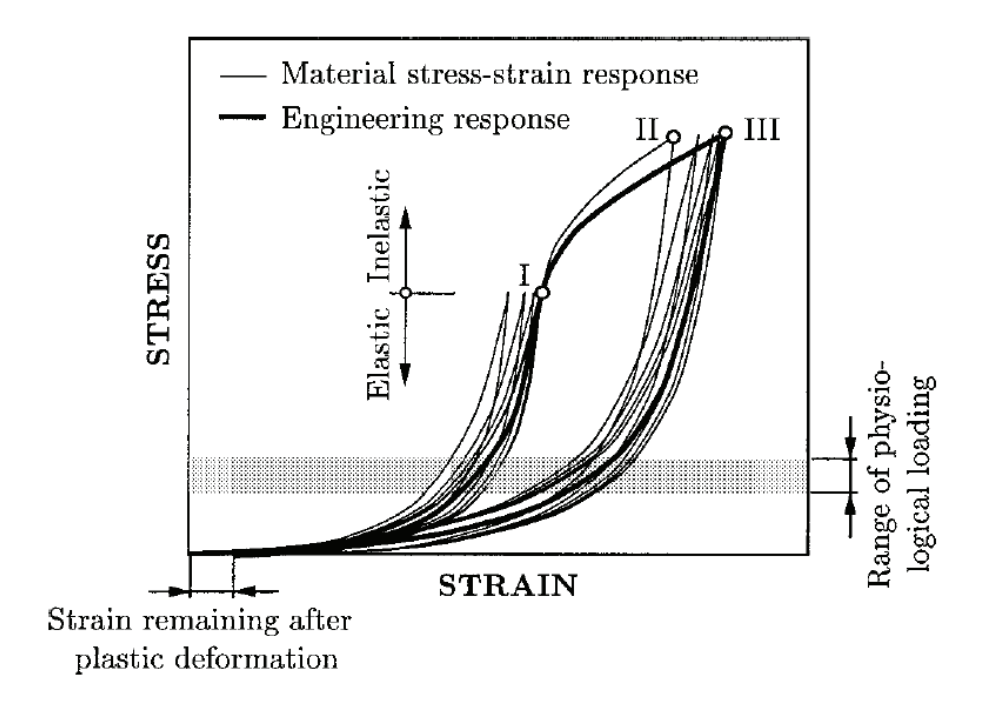


Fig. 1.4: Typical stress-strain curves of a circumferential strip of an artery during the uniaxial test (Holzapfel et al., 2000)

#### 1.2 Mechanical behavior of the aorta

The mechanical properties of an aorta vary with species, age, location, and its pathological conditions. Although there are many documents to report the characteristics of mechanical behavior of the aorta, some important findings are briefly summarized in this section.

Like many other biological soft tissues, an aorta undergoes relatively large deformations and its behavior is nonlinear, inelastic, and anisotropic over finite strains. Fig. 1.4 shows the typical stress-strain response of a circumferential arterial strip during the uniaxial test in passive condition. An arterial tissue displays stress softening during the first few loading cycles, as shown in Fig. 1.4. Then it exhibits a nearly repeatable cycle behavior (Yin and Fung, 1971). Due to the repeatable behavior in cyclic loading, the mechanical behavior of arterial tissues are often described by using pseudoelasticity. For example, Fung et al. (1979) stated that, "Since stress and strain are uniquely related in each branch of a specific cyclic

process, we can treat the material as one elastic material in loading and another elastic material in unloading. Thus, we can borrow the method of the theory of elasticity to handle an inelastic material. To remind us that we are really dealing with an inelastic material, we call it pseudoelasticity". However, the hysteresis, the difference between the loading and unloading curves, is typically small and a majority of experimental studies of a blood vessel have used only loading curves for characterizing the pseudoelastic behavior. Fung et al. (1979) also suggested that it is convenient to simplify a complex property of an artery although the pseudoelasticity is not an intrinsic property.

Long-term vascular adaptation of a blood vessel occurs under various pathophysiological conditions, such as aging (Groenink et al., 1999; Spina et al., 1983) and cardiovascular diseases (Angouras et al., 2000; Thubrikar et al., 2001; Vande Geest et al., 2006). It appears that changes in the mechanical state of a blood vessel wall play important roles in vascular adaptations (Humphrey, 2008). An important goal of vascular mechanics is to accurately estimate the mechanical state of blood vessels in vivo, which is the key determinants of vascular homeostasis. Although the time course and detailed mechanisms of vascular homeostasis remain unclear, many studies have suggested that blood vessels alter their microstructures to restore a preferred (homeostatic) state (Humphrey, 2001).

In the study of vascular mechanics, the discovery of residual stress in an artery has been of great importance. When an arterial ring is cut radially, the ring springs open. Chuong and Fung (1986) reported that the stress resultant and stress moments were zero after the radial cut from the static equilibrium. They identified a stress-free state and showed that circumferential residual strain reduced the transmural gradients of stress and strain (Chuong and Fung, 1986).

During the last several decades, mathematical descriptions for mechanical behavior of blood vessels have been extensively developed. Takamizawa and Hayashi (1987) proposed the uniform transmural circumferential strain hypothesis, but Guo et al. (2005) found that the uniformity of the transmural strain was limited when the opening angles of arteries were smaller than 180°. Zhang et al. (2005) proposed the uniform biaxial strain hypothesis, including the uniformity of the both circumferential and axial strains *in vivo*. Later, it was also shown that the vascular smooth muscle action contributes to more uniform strain and stress distribution throughout the arterial wall (Rachev and Hayashi, 1999).

Many constitutive models have been developed to describe the mechanical behavior of a blood vessel under specific conditions of interest. Strain energy function, commonly in exponential, polynomial, and logarithmic forms, is used to determine a constitutive model in hyperelasticity. The simplest strain-energy function W per unit volume is the neo-Hookean model

$$W = c_1 (I_c - 3) (1.1)$$

where  $c_1$  is a material parameter having the dimension of stress and  $I_c = tr\mathbf{C}$ . It is appropriate for homogeneous, isothermal, and hyperelastic materials. Another commonly used strain energy function for rubber-like material is the Mooney-Rivlin model

$$W = c_2 (I_c - 3) + c_3 (II_c - 3)$$
(1.2)

where  $c_2$  and  $c_3$  are material parameters, and

$$II_c = \frac{1}{2} \left[ (tr\mathbf{C})^2 - tr\mathbf{C}^2 \right]. \tag{1.3}$$

Vaishnav et al. (1973) proposed a two dimensional (2D) strain-energy function in polynomial form to describe the three-dimensional (3D) anisotropic behavior of passive vascular tissue as

$$W = a_1 E_{\Theta\Theta}^2 + a_2 E_{\Theta\Theta} E_{ZZ} + a_3 E_{ZZ}^2 + a_4 E_{\Theta\Theta}^3 + a_5 E_{\Theta\Theta}^2 E_{ZZ} + a_6 E_{\Theta\Theta} E_{ZZ}^2 + a_7 E_{ZZ}^3$$
 (1.4)

where  $a_i (i = 1, \dots, 7)$  are material parameters having in the unit of stress.

A well-known strain energy function for soft tissue was proposed by Chuong and Fung

(1983). It is a 3D strain energy function W per unit initial volume in the undeformed configuration such that

$$W = \frac{1}{2}c_4 \exp\left(Q\right) \tag{1.5}$$

where  $c_4$  is a material parameter having the same unit of stress and Q is given by

$$Q = b_1 E_{RR}^2 + b_2 E_{\Theta\Theta}^2 + b_3 E_{ZZ}^2 + 2b_4 E_{RR} E_{\Theta\Theta} + 2b_5 E_{\Theta\Theta} E_{ZZ} + 2b_6 E_{ZZ} E_{RR}$$
 (1.6)

where  $b_i(i=1,\dots,6)$  are non-dimensional material parameters, and  $E_{IJ}$   $(I,J=R,\Theta,Z)$  are Green's strain components in the cylindrical polar coordinate  $(R,\Theta,Z)$ . Later, a modified 3D strain-energy function of Fung's type form was formulated by Humphrey (1995) with shear terms in the exponential function.

Another type of a 2D strain energy function in logarithmic form was proposed by Takamizawa and Hayashi (1987) as

$$W = -c_5 \operatorname{Ln}(1 - Q') \tag{1.7}$$

where  $c_5$  is a material parameter and the function Q' is given by

$$Q' = \frac{1}{2}d_1E_{\Theta\Theta}^2 + \frac{1}{2}d_2E_{ZZ}^2 + d_3E_{\Theta\Theta}E_{ZZ}.$$
 (1.8)

Here  $d_i(i = 1, 2, 3)$  are non-dimensional material parameters.

A combined polynomial and exponential form of strain energy function was proposed by Holzapfel and Weizsacker (1998) as

$$W = \frac{c_6}{2}(I_c - 3) + \frac{c_7}{2} \left\{ \exp(Q) - 1 \right\}. \tag{1.9}$$

where material parameters  $c_6$  and  $c_7$  having the unit of stress. Later Holzapfel et al. (2000) proposed another strain energy function, which modeled an arterial tissue corresponding to the isotropic deformations and anisotropic deformations, considering two collagen fiber fam-

ilies. To determine the isotropic response, neo-Hookean model was used and the anisotropic response was determined by an exponential function such that

$$W_{aniso}(I_4, I_6) = \frac{k_1}{2k_2} \sum_{i=4,6} \left[ \exp\left\{ k_2 (I_i - 1)^2 \right\} - 1 \right]$$
 (1.10)

where  $k_1$  a material parameter in the unit of stress and  $k_2$  is a dimensionless parameter.  $I_4$  and  $I_6$  are invariants of  $\mathbf{C}$ . Holzapfel and others also developed two-layer model (media and adventitia as a fiber-reinforced composite) with residual strains. Yet another strain energy function was proposed by Zulliger et al. (2004b)

$$W = f_e c_e (I_c - 3)^{3/2} + f_c \left\{ \frac{1}{2} W_c \left( \sqrt{I_4} - 1 \right) + \frac{1}{2} W_c \left( \sqrt{I_6} - 1 \right) \right\}.$$
 (1.11)

where  $f_e$  and  $f_c$  are the area fraction of elastin and collagen, respectively,  $c_e$  the elastic constant, and  $W_c$  the strain-energy function of the collagen. It accounts for wall compositions and structures, such as the wavy nature of the collagen fibers and their angle.

While the aforementioned constitutive models have been developed for traditional stress-strain analysis, the constitutive model based on a constrained mixture approach has been developed to describe continuous growth and remodeling of vascular tissue (Baek et al., 2006; Humphrey and Rajagopal, 2002; Zeinali-Davarani et al.). That is, it deals with not only the separate contribution of each constituent of a blood vessel but also the continuous production and removal of each constituent during the vascular adaptation. Thus, a constrained mixture model can provide the potential role of each constituents, elastin, collagen, and smooth muscle, in the mechanical behavior of stressed material.

# 1.3 Variation and heterogeneity of the mechanical behavior of the aorta

The mechanical properties of the aorta vary with locations on the aortic tree (Han and Fung, 1995), and, indeed, the aortic wall is not isotropic (Weizsacker, 1988; Zou and Zhang, 2009). For example, the dog thoracic aorta in situ was stiffer in the longitudinal than the circumferential direction (Patel et al., 1969), there is the longitudinal variation in circumferential strain and elastic modulus of mouse aortas (Huang et al., 2006), and the stretch ratio and Cauchy stress were lower in the thoracic aorta than the abdominal aorta (Guo and Kassab, 2004).

The arterial wall is a heterogeneous composite consisting mainly of collagen, elastin, and smooth muscle cells. The relative amount of these constituents is responsible for the mechanical properties of a blood vessel and varies with locations along the arterial tree (Fischer and Llaurado, 1966; Halloran et al., 1995; Lillie and Gosline, 2007; Purslow, 1983; Roach and Song, 1994; Stergiopulos et al., 2001). The histology of the aorta is different between the thoracic and abdominal regions. The thoracic aorta contains relatively more elastin, whereas the abdominal aorta contains relatively more collagen (Thubrikar, 2007). Elastin and collagen are the major components of the ascending thoracic aorta, and smooth muscle cells are the major components of the abdominal aorta.

The influence of elastin on the mechanical properties of the aortic tissue has been investigated (Gundiah et al., 2007; Lillie and Gosline, 2007; Zou and Zhang, 2009). Elastin fibers are primarily responsible for the linear behavior of an artery in the low pressure range (Gundiah et al., 2007; Shadwick, 1999; Stergiopulos et al., 2001). On the other hand, collagen is recruited in the higher pressure range and contributes to the nonlinear behavior of arterial tissue with elastin (Groenink et al., 1999; Shadwick, 1999). The orientation of collagen and the amount of cross-linking contribute to the mechanical behaviors of vascular tissue (Haskett et al., 2010; Holzapfel et al., 2002). Stergiopulos et al. (2001) attempted to characterize

the elastic properties and composition of the separated inner and outer halves of porcine aortic media, and they concluded that these properties were similar. The three-dimensional structure of the rat aortic media was observed using 3D confocal microscopy, the number of medial lamellae in anterior region were greater than the posterior (O'Connell et al., 2008).

# 1.4 Experimental characterization of mechanical behavior of the aorta

For the experimental studies, ex vivo including in vitro tests are commonly employed, although in vivo tests would characterize the biomechanical behavior of a blood vessel under actual physiological conditions. It is due to the limitation of in vivo tests such as the complexity of in vivo physiological conditions, difficulty of obtaining accurate strain measurements, and the uneasiness of controlling experiments.

A variety of ex vivo testing methods have been developed to characterize the mechanical properties of vascular tissue using different shapes of tissue specimens, such as strips, flat sheets, rings, or cylindrical tubes. The most common biomechanical test is the uniaxial extension test with a strip for investigating mechanical behavior of the vascular tissue in one direction under cyclic loading (Gundiah et al., 2007; Iliopoulos et al., 2009b; Lally et al., 2004; Okamoto et al., 2002; Sokolis, 2007), but it is not suitable to quantify the anisotropic behavior of vascular tissues. The ring test (Guo and Kassab, 2004; Huang et al., 2006; Lillie and Gosline, 2007) is another type of the uniaxial test on arterial rings. It is commonly used to quantify the yield strength or active smooth muscle tone of a blood vessel in the circumferential direction, but it is insufficient to study the anisotropy of vascular tissues because it does not measure deformation and force in axial direction. A planar biaxial test with excised flat sheet specimens has been popular for investigating biaxial mechanical behavior of aortic tissue (Lally et al., 2004; Okamoto et al., 2002; Tremblay et al., 2010; Vande Geest et al., 2006; Zhou and Fung, 1997). However, lateral excision of the tissue may

alter the spatial distribution of residual stress in the specimen and, thus, it is difficult to simulate the deformation of the artery experienced during the cardiac cycle. On the other hand, the inflation test with a cylindrical tube segment is the preferred test for obtaining biaxial mechanical properties of a blood vessel (Blondel et al., 2001; Humphrey et al., 1993; Langewouters et al., 1984; Schulze-Bauer et al., 2002). This test reflects closely the motion of the aortic wall during the cardiac cycle so that we estimate *in vivo* stress, although the surrounding tissue are not usually taken into account in the *ex vivo* test.

Since vascular tissues experience finite deformation and stress during the test, a video-based tracking technique is typically applied, with multiple markers embedded or affixed to the tissue specimen (Everett et al., 2005; Hu et al., 2007; Hsu et al., 1995; Saravanan et al., 2006; Thubrikar et al., 1990; Zhang et al., 2002). In the traditional ex vivo inflation test, a blood vessel is assumed to be a perfect cylindrical tube and only the outer diameter change of the vessel is measured during the test (Blondel et al., 2001; Langewouters et al., 1984; Schulze-Bauer et al., 2003; Valdez-Jasso et al., 2009). Hence, the spatial distribution of local mechanical properties of the vessel is not commonly characterized in the traditional inflation test.

Recent advances in the 3D medical imaging have allowed one to use a tracking technique to measure nonuniform deformation during the test. For example, Draney et al. (2004) quantified in vivo cyclic strain of porcine aortas using cine phase contrast magnetic resonance imaging (MRI). In their study, the cyclic strain were not uniform along the circumference of the aorta, but their results were highly deviated. Danpinid et al. (2010) proposed a method to investigate the local stress-strain relationship of both normal and pathological murine abdominal aortas using an ultrasound motion estimation technique, and it allowed one to identify the vascular disease. Recently, Genovese (2009) introduced a new optical system with a concave conical mirror, which provides the full-field measurement of 3D deformation of an artery, and Avril et al. (2010) developed an inverse method to determine material parameters using the experimental data under the traditional assumption. The accuracy of

the method and its utility is, however, not yet clearly demonstrated and there is still a need for developing more analysis methods to make full use of 3D spatial information of the artery. Development of such strain measurement techniques promotes the study for characterizing the heterogeneity in the mechanical properties of a blood vessel over a wide range of pressure, and thus more experimental techniques and novel analysis methods need to be developed.

## 1.5 Objective of this study

While it is well known that the mechanical properties of a healthy blood vessel vary with location (Lillie and Gosline, 2007; Sokolis, 2007) and age (Groenink et al., 1999; Spina et al., 1983), their circumferential variations have received little attention. In the majority of biomechanical analysis in vascular studies, an artery has been considered as a hollow conduit with a constant thickness, and uniform stress and strain distribution in the vessel wall has been assumed in the circumferential direction (Chuong and Fung, 1986; Takamizawa and Hayashi, 1987; Zhang et al., 2005). Furthermore, in most previous experimental studies using the inflation test, only outer diameter change associated with a pressure change was measured, and the circumferential variation in the local mechanical properties of the vessel was not usually characterized. Recent biomedical imaging studies, however, showed the non-uniform circumferential behavior of the aorta during the cardiac cycle (Draney et al., 2002, 2004), the asymmetric distension of the aortic wall (van Prehn et al., 2009a,b), and an increased amount of the anterior agric wall motion relative to the posterior (Goergen et al., 2007). Therefore, it is essential to consider nonuniform deformation of the aorta in the circumferential direction to obtain a physiologically more accurate mechanical model. Nonetheless, few experimental studies have quantified the circumferential variation in the mechanical behavior of the aorta.

The goal of this study is to investigate the spatial variations in the mechanical properties of the thoracic aorta. In order to investigate the spatial variation, the aortic wall is classified by the location of the aorta: the proximal and distal portions in the longitudinal direction; and the anterior (A), left lateral (L), posterior (P), and right lateral (R) regions in the circumferential direction. The specific aims of this study are:

- to develop a biaxial experimental apparatus to measure the local deformation of a blood vessel
- to perform the inflation tests at fixed longitudinal stretch ratios for the two longitudinal portions and the four circumferential regions of the porcine thoracic aorta
- to develop a stress-strain analysis using 3D experimental data
- to investigate variations in stretch, stress, stiffness, and pressure-strain elastic modulus and analyze statistically
- and to estimate material parameters using a constrained mixture model

This dissertation consists of six chapters. Chapter 2 describes the experimental apparatus designed and constructed for this study. It includes features of the extension-inflation test device and a stereo vision system that allows us to track 3D motion of the aorta during the test. After that, it describes sample preparation and the protocol of the inflation test. Camera calibration and image processing is addressed lastly. Chapter 3 focuses on biomechanical analysis to determine the local mechanical properties of the thoracic aorta. It introduces the kinematics in the curvilinear coordinate system, approximation of the surface, and then equations of the circumferential stretch, stress, and stiffness in both longitudinal and circumferential directions.

Chapter 4 presents a constitutive model to describe the mechanical response of the both proximal and distal portions of the thoracic agree during the inflation test. It includes the parameter estimation study using a constrained mixture model.

Chapter 5 shows the results of experiments, stress-strain analysis, material parameters, and the statistical analysis. The major finding of this study and discussion are finally

presented.

Lastly, Chapter 6 summarizes this dissertation and contribution of this study and then briefly discusses potential future study.

## Chapter 2

## EXPERIMENTAL METHODS

### 2.1 Experimental apparatus

An extension-inflation test system (Fig. 2.1 and Fig. 2.2) was developed to measure the biaxial deformation of a blood vessel. It consists of three main parts: motion, data acquisition, and vision systems.

A polycarbonate test chamber is placed on the lower crosshead in the center of the test device. Two moving crossheads are driven by a stepper motor in opposite directions, while the center of the device remains fixed. A specimen is connected to a syringe pump (KDS 210, KD Scientific, MA, USA) by a tube. Bidirectional infusion-withdrawal motion of the syringe pump inflates and deflates the specimen.

A 34.47 kPa (5 psi) gauge pressure transducer (FPG2AT, Honeywell-Sensotec, OH, USA) is installed to the tube, which is connected to the specimen. In this study, the transmural pressure is defined as the difference between internal pressure and external pressure of the region where markers attached to the specimen. In Fig. 2.3, transmural pressure can be

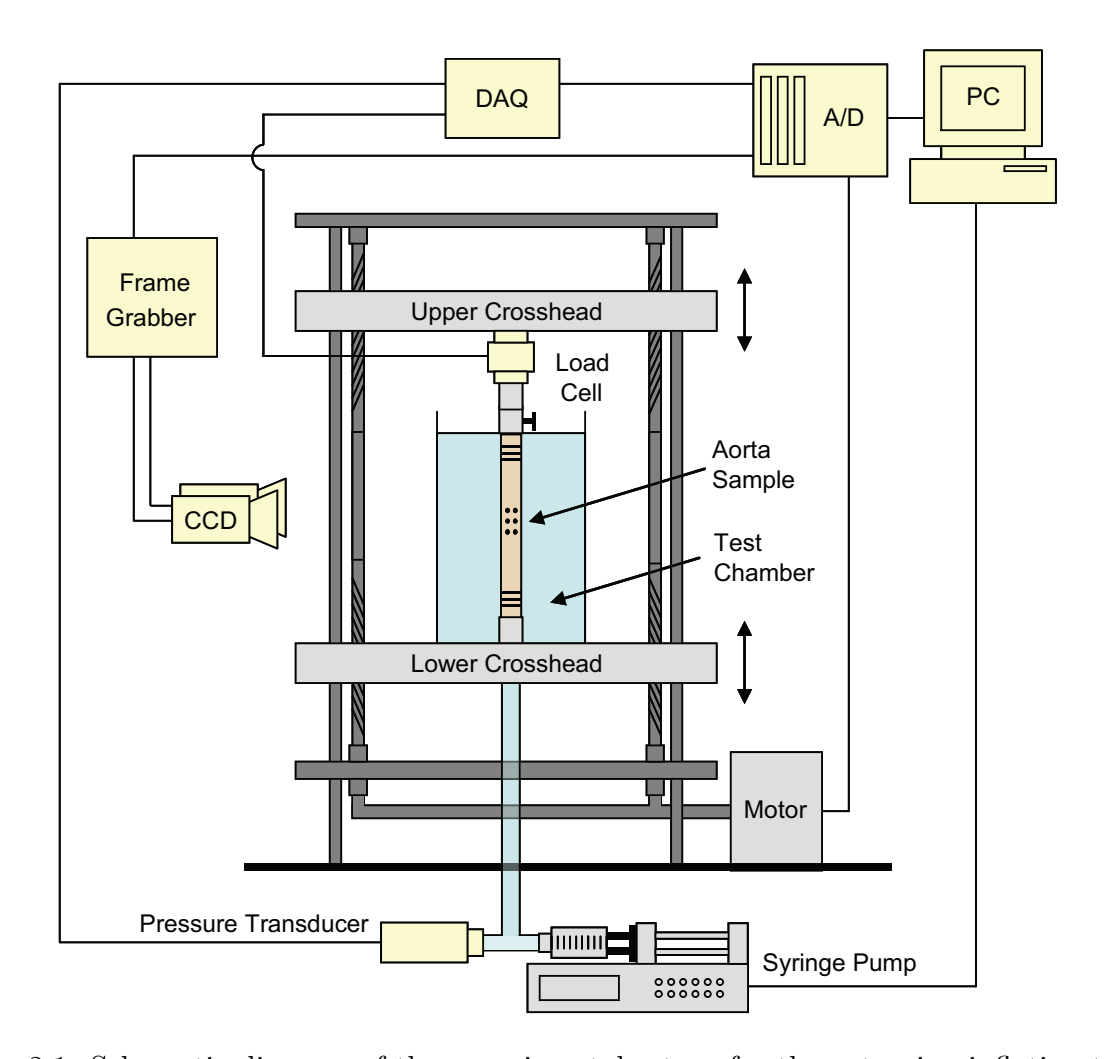


Fig. 2.1: Schematic diagram of the experimental set-up for the extension-inflation test.

calculated via

$$P_B^{trans} = P_B^{inter} - P_B^{exter} (2.1)$$

$$= P_A - \gamma h_1 - \gamma h_2 \tag{2.2}$$

$$=P_A - \gamma \left(h_1 + h_2\right) \tag{2.3}$$

$$= P_A - \gamma h. \tag{2.4}$$

where  $P_A$  and  $P_B$  are the pressure at the location of A and B, respectively, and  $\gamma$  is the specific weight. The axial load applied to the specimen during the test is measured using a 4.54 kg (10 lb) load cell (Model 34, Tension/Compression, Honeywell-Sensotec, OH, USA),

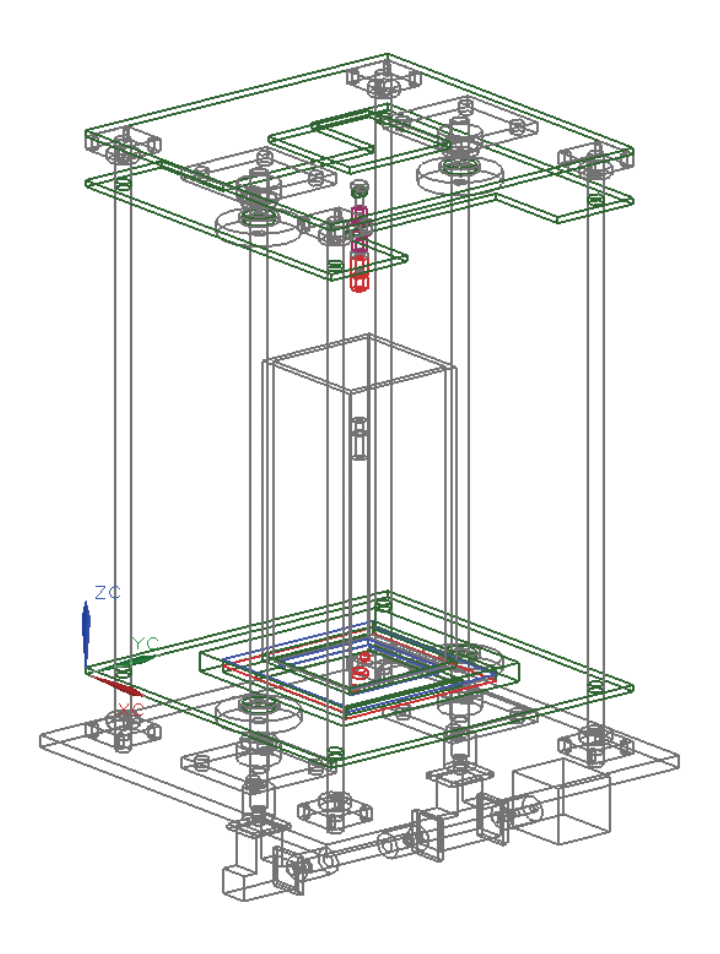


Fig. 2.2: Schematics of the experimental device.

which is attached to the upper cannula of the specimen. The measurements are collected in a computer by a data acquisition board at a 100 Hz sampling rate.

The stereo vision system, consisting of two CCD monochrome cameras (KPM2A, 768H × 494V, Hitachi, Japan) with fixed focal length lenses (HF25HA-1B, Fujinon, Japan), allows the tracking of the 3D position of markers attached to the specimen. Two cameras are placed at different positions but at the same height, focusing on the central region of the test device where the specimen is mounted (Fig. 2.4). The distance of two cameras is approximately 30 cm, and the angle between two cameras and the specimen is approximately 30 degrees. The frame grabber obtains images of markers affixed to the specimen using the two cameras alternately at 5 frames per 2 seconds.

A computer program is designed to control the experimental system using Labview 8.2.

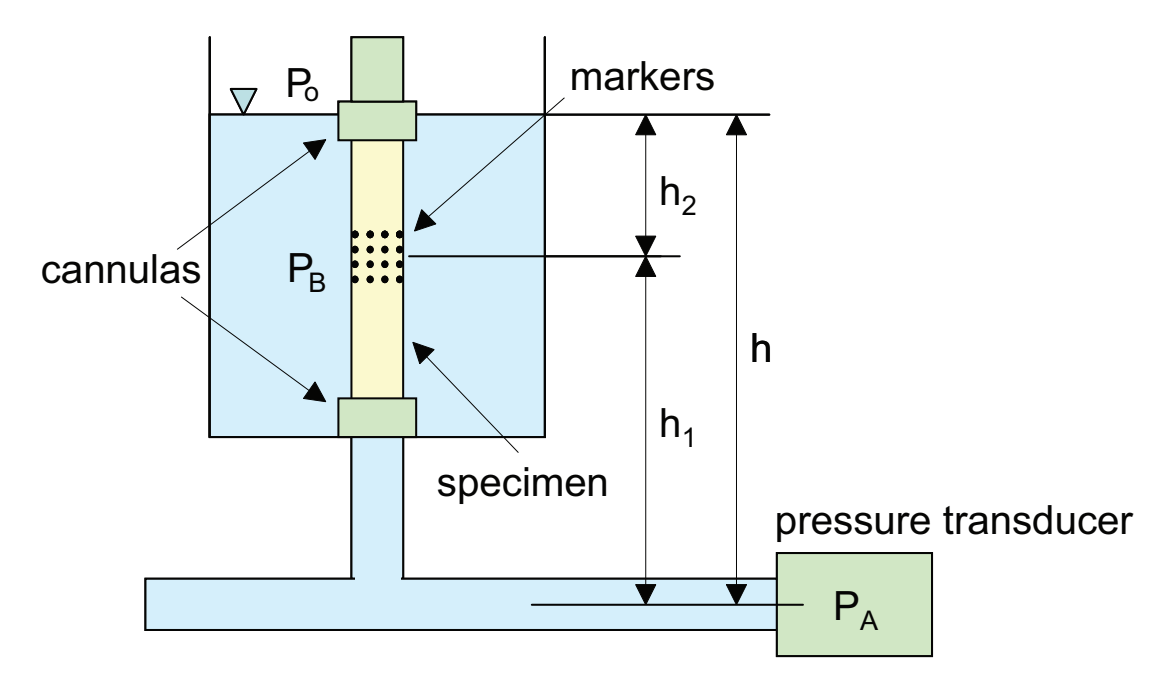
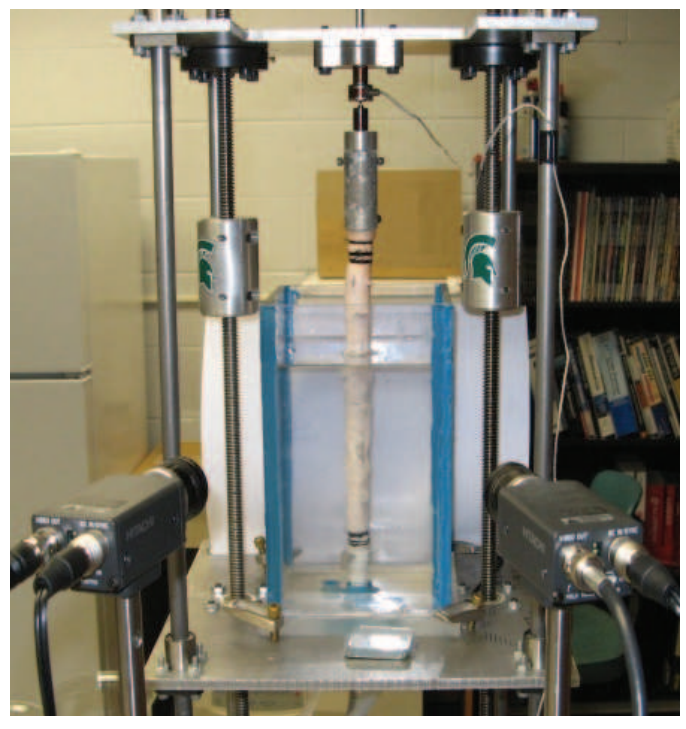


Fig. 2.3: Schematics of the test chamber to show calculation of the transmural pressure

The speed and direction of the syringe pump are controlled by the automated Labview program based on the pressure readings.

A few considerations were made when designing the test device. First, this test device has a multiple-cannula mounting connector for testing several types of blood vessels. This test device is able to test various sizes of specimens, whereas most of existing pressurization testers have been used only for small vessels or short segments of blood vessels. Second, this test device has a vertical mounting system. The vertical set-up is designed to avoid the bending of a blood vessel caused by gravity, since the target length of an aorta sample in this study was about 12 cm. In addition, the vertical mounting system allows us to use multiple cameras around the specimen to record its deformation from multiple directions. Third, its height is adjustable, while the center of the device is fixed. Due to the irregular length of blood vessels and different longitudinal extension for testing, the adjustable height of a test device was needed. Two parallel crossheads maintain the center of the specimen in longitudinal direction, while the crossheads travel in opposite directions along two vertical threads. Lastly, it has less incidence of and is easy to remove air bubbles. At the end of the



(a) Camera set-up with the specimen

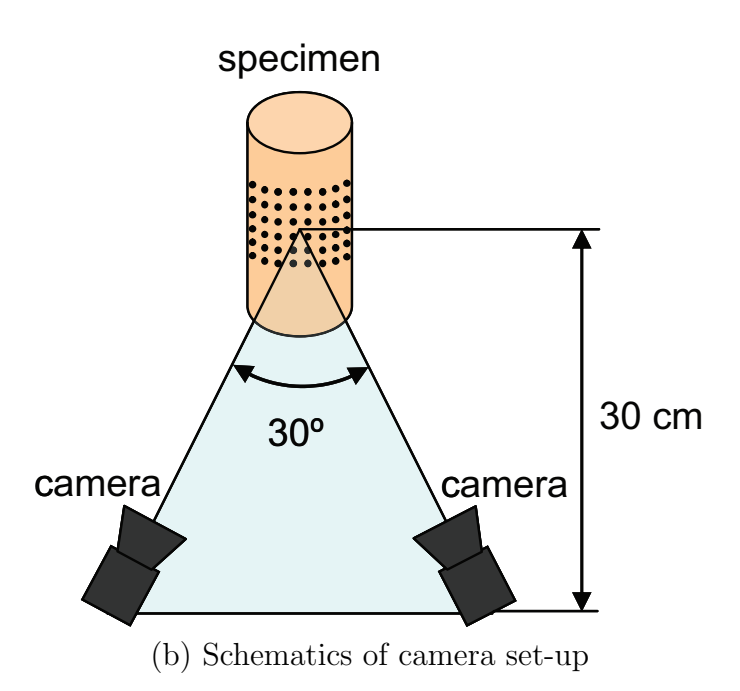


Fig. 2.4: Two camera set-up

tube away from the specimen, saline solution is injected into the tube using a three-way-valve. To remove air bubbles inside the specimen and the tube, upper cannulas (2.6) were

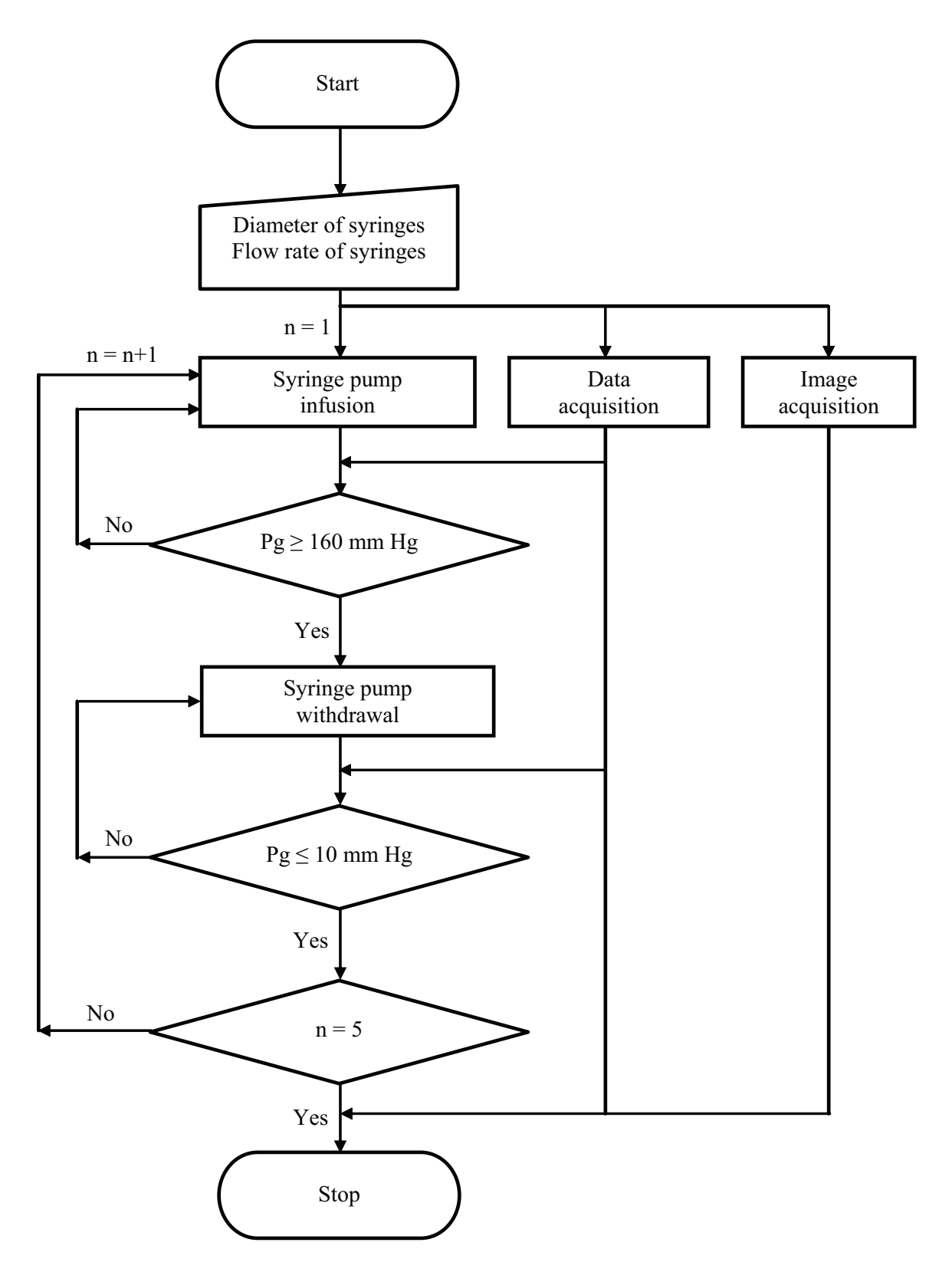


Fig. 2.5: Overview of the experimental process using the extension-inflation test device.

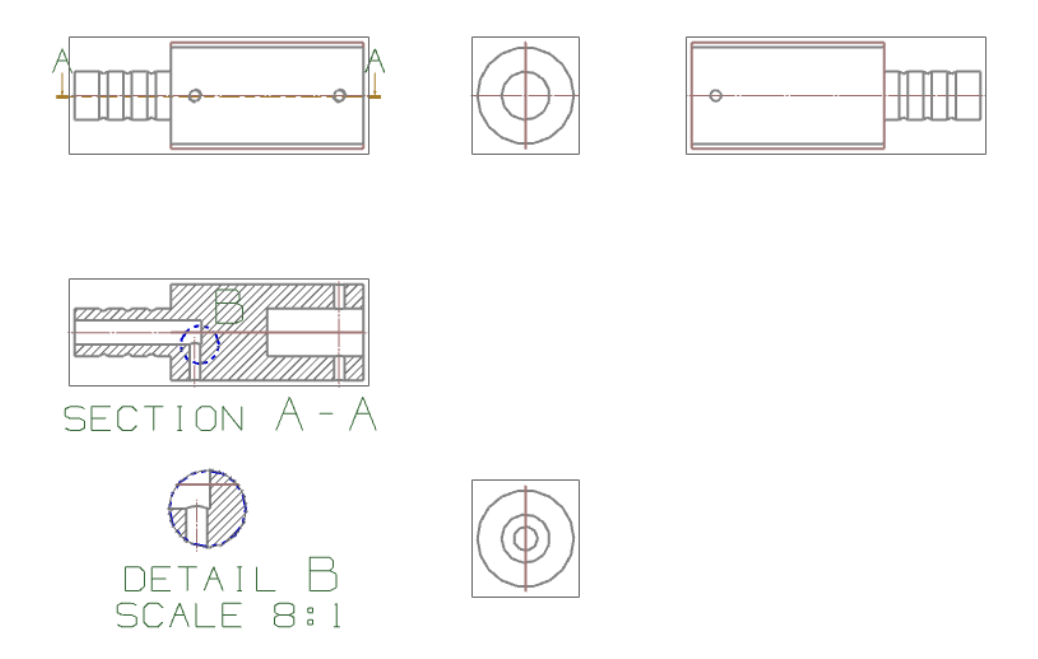


Fig. 2.6: Schematic drawing of an upper cannula connector.

specially designed. They have a tiny hole, which can be opened while the saline solution is filling the specimen and can be closed after the removal of air for the test.

#### 2.1.1 Calibration of sensors

The load cell has been calibrated by using weights with a string. Five different weights in turn are hung, and each voltage output from the data acquisition board is recorded, respectively. A linear least squares regression is used to determine an equation of best-fit line for the test data, that is, the known weights and the voltage outputs of load cell corresponding to the weights. The slope and y-intercept of the fitting equation are used to convert voltage outputs into axial loads applied to the specimen during the test. Fig. 2.7 (a) shows an example of the least squares regression for calibrating the load cell.

Likewise, the pressure transducer has been calibrated by using a single-limb manometer connected to the pressure transducer with a vinyl tube. Five different column heights of water in the manometer and their corresponding voltage outputs of the pressure transducer are recorded. The room temperature is accounted for calculating the hydrostatic pressure for

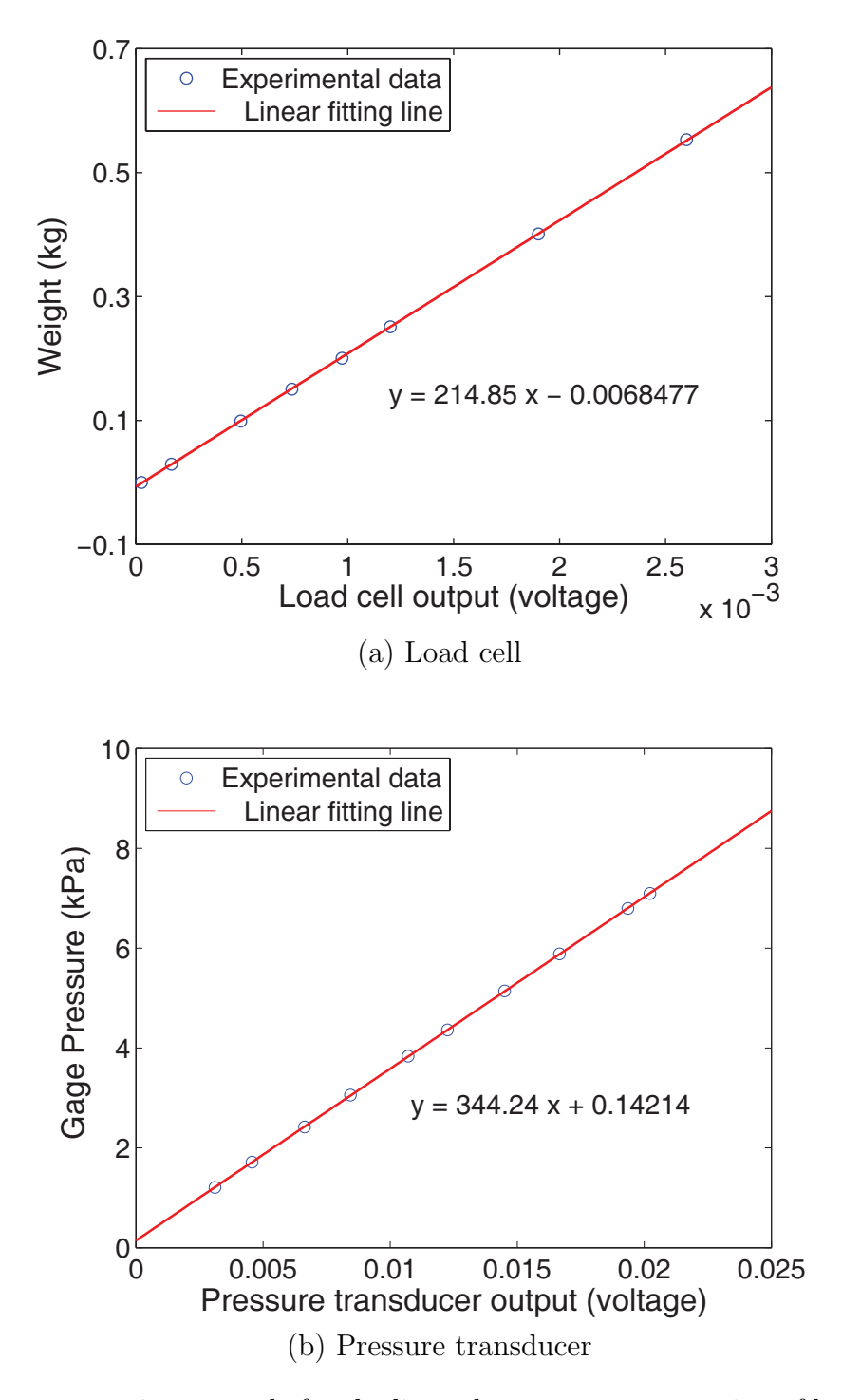


Fig. 2.7: A representative example for the linear least squares regression of load cell data (a) and pressure transducer data (b).

the case of each water column. A linear least squares regression is used again to determine a relationship between the pressure and voltage output of the pressure transducer. The slope and y-intercept of the fitting equation are used to calculate the internal gauge pressure of the specimen. Fig. 2.7 (b) shows an example of the least squares regression for calibrating the pressure transducer.

# 2.2 Specimen preparation

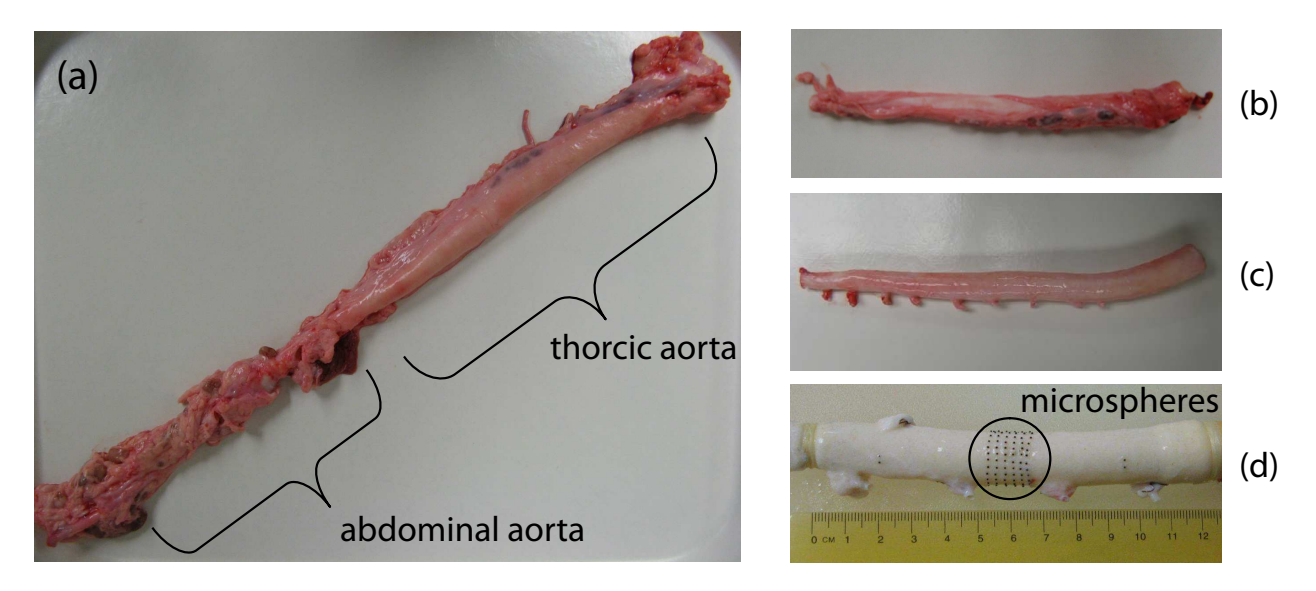


Fig. 2.8: (a) The porcine aorta sample from the thoracic to the abdominal, (b) the thoracic aorta with surrounding tissues, (c) the thoracic aorta after removing surrounding tissues, and (d) a cannulated aorta specimen with micro spheres attached on the wall.

Aortas from approximately six-month-old pigs (Fig. 2.8 (a)) were obtained from a local slaughterhouse. They were stored at 5°C until testing within 24 hours after death. For the inflation test, the peripheral, loose connective tissues are carefully removed from the adventitia of the aorta, while aortic branches are kept intact (Fig. 2.8 (b) and (c)). The proximal or distal portion of straight descending thoracic aorta, approximately 15 cm long, is isolated. All aortic branches are ligated with nylon thread, and both ends of the isolated aorta are connected to cannulas with care to ensure the aorta is not bent or twisted. Approximately 140 black spheres with a diameter of 550  $\mu$ m, as markers, are attached to the aorta along its circumference. They are attached to the aortic wall near either the first to third intercostal arteries for the proximal portion of the thoracic aorta or the fifth to seventh

intercostal arteries for the distal portion, avoiding the regions of aortic branches (Fig. 2.8 (d)). Additional microspheres are attached to the proximal and distal regions of the specimen with 7 cm distance to obtain the reference measurements of longitudinal stretches. In order to reduce the amount of glue, a pulled-glass micropipette is used. Then the specimen is mounted vertically in the test chamber and the inside of the specimen and test chamber are filled with 0.9% NaCl solution. The osmolarity is kept for all tests to limit the effect of osmolarity on the mechanical behavior of a vessel (Guo et al., 2007).

## 2.3 Test protocol

The unloaded reference length wherein the blood vessel is at zero longitudinal force and at zero transmural pressure is recorded, ignoring the effect of the weight of specimens. The specimen is preconditioned longitudinally and circumferentially to obtain repeatable mechanical response of the blood vessel and to reduce possible stress concentration induced during the preparation. The specimen is then elongated at stretch ratios of 1.35, 1.40, or 1.45 with respect to the reference length. The aorta has a pre-stretch in the longitudinal direction at the *in vivo* state, and its *in situ* stretch ratio was estimated between 1.2 and 1.45 (Han and Fung, 1995). For each fixed longitudinal stretch ratio, the inflation test is performed by pressurizing and depressurizing the specimen five times at approximately 1/110 Hz frequency over a transmural pressure range from 1.33 kPa to 21.33 kPa (10 - 160 mm Hg) at room temperature. Digital images of markers affixed to the specimen are collected simultaneously with pressure and axial load measurements.

In this study, the aortic wall is classified into four regions in the circumferential direction. The wall between two consecutive intercostal arteries is defined as the posterior region, its opposite across the lumen is defined as the anterior region, and the two side regions between the anterior and posterior regions are determined as the left and right lateral regions. For the proximal thoracic aorta, the inflation test is repeated at the four circumferential regions

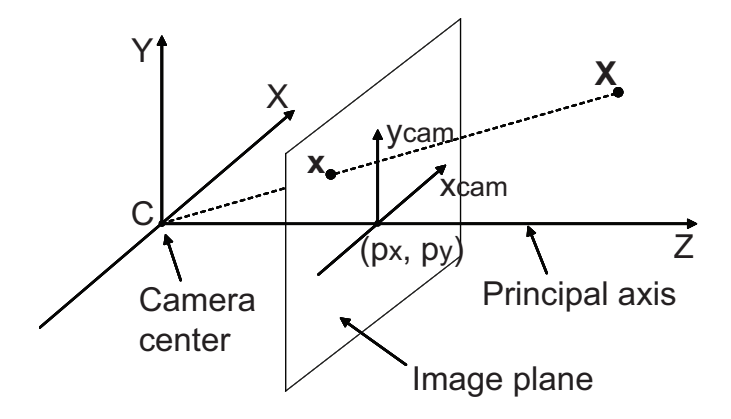


Fig. 2.9: Schematics of a world point and its corresponding image point

(A, L, P, and R) after a 90-degree rotation of the specimen between one region and another. For the distal thoracic aorta, the test is repeated at two circumferential regions (A, P) after 180-degree rotation. Great care is taken in ensuring no twisting of the specimen after the rotation.

After the inflation test, two cross-sectional cuts of the specimen to obtain an aortic ring are made at the test region where the markers are affixed. Three repeated wall thickness measurements per specimen are taken at every 45 degrees along the circumference using a digital vernier caliper. Then, the aortic ring segments are fixed in 10 % formal saline for histology examination.

For this study, seven samples of the proximal thoracic aorta and four samples of the distal thoracic aorta were used, and their experimental information is tabulated in Table C.1 in Appendix C.

# 2.4 Marker tracking and 3D position reconstruction

#### 2.4.1 Calibration of cameras

A 3D calibration jig, which displays array of dots with known spacing, was used. A finite projective camera model have been employed to determine a camera matrix. Projection

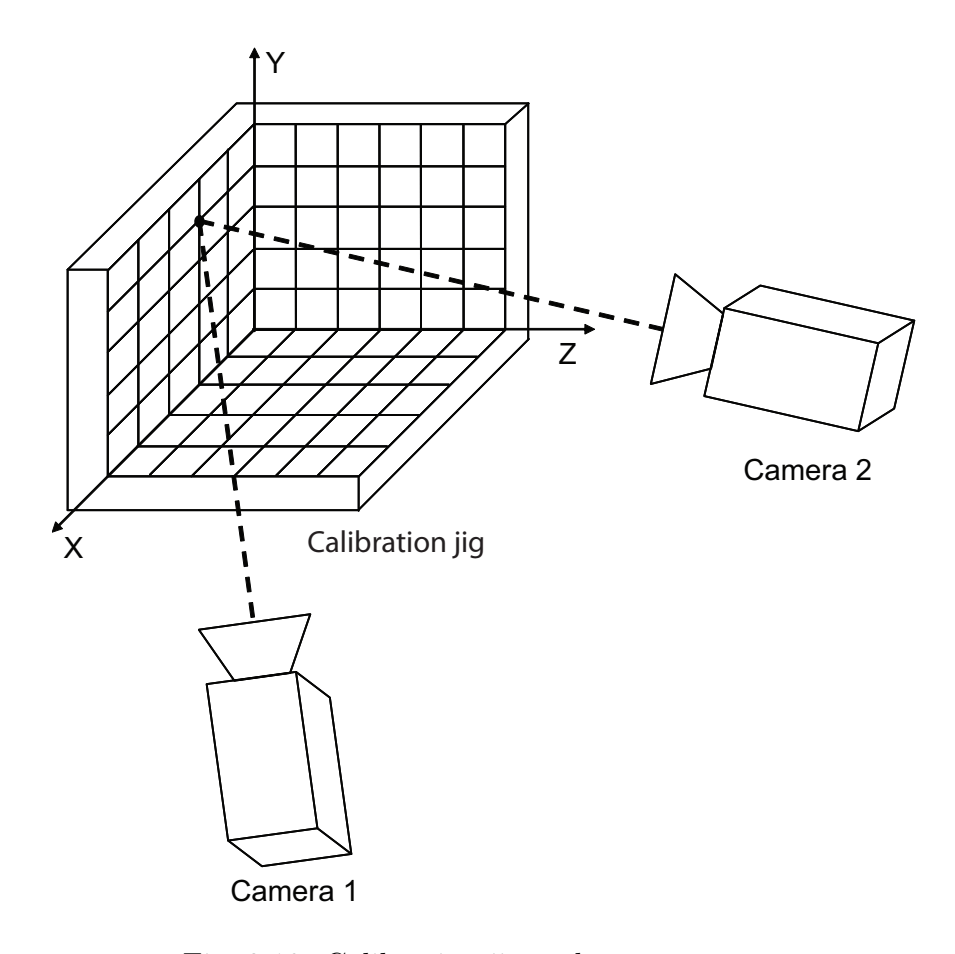


Fig. 2.10: Calibration jig and camera set-up

under this model is a linear mapping in the form of  $\mathbf{x} = \mathbf{M}\mathbf{X}$  using homogeneous coordinates, where a camera matrix  $\mathbf{M}$  describes how a 3D world point  $\mathbf{X} = (X, Y, Z)^T$  projects to a 2D pixel point  $\mathbf{x} = (x, y)^T$  in the image coordinate. In brief, the camera matrix is determined via three steps. First, a 3D world point (X, Y, Z) is transformed to a point in the camera reference frame by rotation and translation. Next, the point is projected onto the image plane at  $(x_{cam}, y_{cam})$ . Lastly, the point  $(x_{cam}, y_{cam})$  on the image plane is mapped into the pixel coordinates in an image. (The details are introduced in Appendix A.) Therefore, the

homogeneous linear mapping can be written as

$$\begin{cases}
sy \\
sx \\
s
\end{cases} = \begin{bmatrix}
M_{11} & M_{12} & M_{13} & M_{14} \\
M_{21} & M_{22} & M_{23} & M_{24} \\
M_{31} & M_{32} & M_{33} & 1
\end{bmatrix} \begin{cases}
X \\
Y \\
Z \\
1
\end{cases}$$
(2.5)

where s is a scaling factor and  $\mathbf{M}_{ij}$  is an element of the calibration matrix.

In equation (2.5), there are 11 unknowns, and more than 6 pairs of 3D world points and their corresponding pixel points in the image are needed. World points are obtained from the calibration jig (Fig. 2.10) and the centers of their pixels in images are extracted through image processing of the images. Using n-number of pixel points corresponding to the world points of the calibration jig, equation (2.5) can be rewritten in the form of  $\mathbf{u} = \mathbf{A}\mathbf{b}$ . Here, u represents a vector of an image pixel point of x-axis and y-axis alternately,  $\mathbf{A}$  represents  $n \times 11$  matrix, and  $\mathbf{b}$  represents all elements of the calibration matrix in a vector. In order to determine the optimized parameter  $\mathbf{b}$  of the calibration matrix, the pseudo inverse (least squares) calculation has been applied. The parameters  $\mathbf{b}$  is obtained by  $\mathbf{b} = (\mathbf{A}^T \mathbf{A})^{-1} \mathbf{A}^T \mathbf{u}$  via minimizing  $\parallel \mathbf{A}\mathbf{b} - \mathbf{u} \parallel^2$ .

## 2.4.2 Image processing

Two CCD cameras obtain serial digital images of the specimen during the inflation test. The center of each marker is extracted via the following steps. Firstly, the image mask from the entire image, that is a small region of markers on the specimen, is defined and the masked region is extracted. Next, the manual threshold type is selected and its range for the masked image is set up, when thresholded markers are displayed clearly from the background. If dark objects are being looked for, markers are shown as dark objects and the aortic wall is shown relatively brighter. After that, border objects of the masked image are removed. Then, the center of mass for markers in x and y directions are obtained from each images

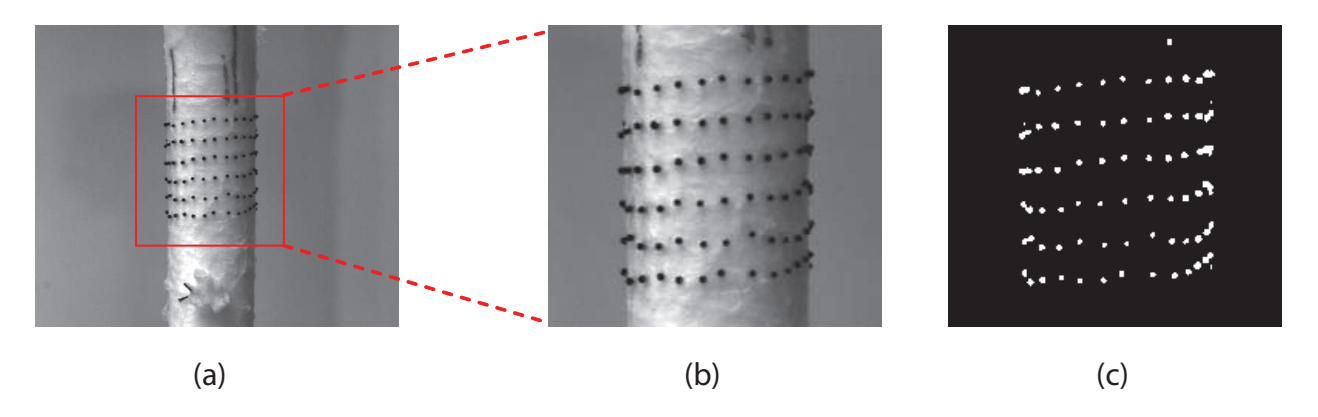


Fig. 2.11: An example of the processing to extract the position of markers in pixel. (a) the entire image, (b) the masked image, and (c) thresholded image

via the particle analysis, which is a built-in function of NI Vision Assistant.

#### 2.4.3 Marker tracking

Using the 2D position data of markers in pixels, the motion of markers is traced over the inflation test. However, the total number of particles in images is not the same as the number of markers. Thus, Matlab programming, so-called the marker tracking algorithm, has been developed to track markers in which we are interested. The algorithm consists of the followings steps. First, some markers of interest are selected from the first image and saved with labels. The positions of markers  $((x_i, y_i))$  in the first image, where i denotes the label of a marker) are compared with the new positions of markers in next image  $((x_j, y_j))$ , where j denotes the label of a marker). Second, the distance between markers from two images  $(|(x_i, y_i) - (x_j, y_j)|)$  are calculated. If a marker of i from the first image had a minimum distance with a marker of j from the next image, we assume that those two markers are the same ones and their distance and labels are recorded. If more than two markers of j in the new image have a same marker of i as a distance between two markers from two consecutive images is minimum, the label of i is repeated. Then a marker of j with a smaller distance from a marker of j which has the same marker of i as the minimum distance is discarded.

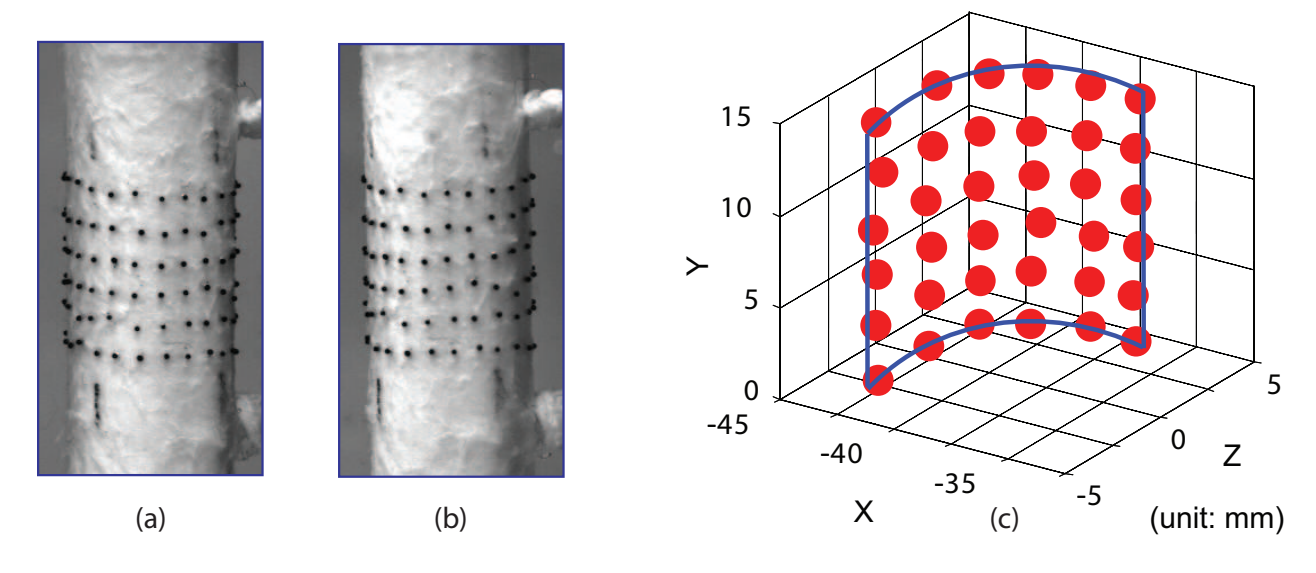


Fig. 2.12: Stereo images from left side camera (a) and right side camera (b), and the reconstructed marker positions in 3D (c)

Therefore, the number of new markers remains as the same number of markers from the first image. However, some of markers from the first image may not be shown later. In this case, the minimum distance of the markers may be bigger than the averaged minimum distance between two consecutive images for all markers. If some markers had a much bigger distance than the averaged minimum distance, they are discarded and the same steps are repeated to find the minimum distance between an image and the next image for the markers. Finally, the new positions of markers are determined. The same process is repeated for the next image with the updated positions of markers until the positions of markers in the last image are determined.

# 2.4.4 3D position reconstruction

Once camera matrices are determined, 3D positions of markers can be obtained using pairs of 2D stereo images taken from both cameras. Linear mapping derived from equation (2.5) for each camera yields four equations with three unknowns (X, Y, Z), which represents a 3D world point corresponding to a pair of image points  $(x^1, y^1)$  and  $(x^2, y^2)$  for both cameras,

as

$$\begin{cases}
y^{1} - M_{14}^{1} \\
x^{1} - M_{24}^{1} \\
y^{2} - M_{14}^{2} \\
x^{2} - M_{24}^{2}
\end{cases} = \begin{bmatrix}
M_{11}^{1} - M_{31}^{1}y_{1} & M_{12}^{1} - M_{32}^{1}y_{1} & M_{13}^{1} - M_{33}^{1}y_{1} \\
M_{21}^{1} - M_{31}^{1}x_{1} & M_{22}^{1} - M_{32}^{1}x_{1} & M_{23}^{1} - M_{33}^{1}x_{1} \\
M_{11}^{2} - M_{31}^{2}y_{2} & M_{12}^{2} - M_{32}^{2}y_{2} & M_{13}^{2} - M_{33}^{2}y_{2} \\
M_{21}^{2} - M_{31}^{2}x_{2} & M_{22}^{2} - M_{32}^{2}x_{2} & M_{23}^{2} - M_{33}^{2}x_{2}
\end{cases} \begin{cases}
X \\ Y \\ Z
\end{cases}$$
(2.6)

where superscript 1 and 2 denote two different cameras. Likewise the process of determining a camera matrix, the pseudo inverse (least squares) calculation is employed to determine the unknown world point (X, Y, Z). Fig. 2.12 shows the stereo images and the reconstructed 3D positions of markers.

# 2.5 Histology sample preparation

At the mid-section of the sample where markers are attached, two transverse cuts of the aorta are made. The aortic ring is fixed in a 10 % formalin solution at room temperature for 3 days and is embedded in paraffin for approximately 24 hours. Then it is sectioned at 5  $\mu$ m thickness and stained with hematoxylin and eosin (H&E), Verhoeff-Van Gieson (VVG), and picrosirius red.

# Chapter 3

# BIOMECHANICAL ANALYSIS

## 3.1 Kinematics in curvilinear coordinate systems

In cardiovascular mechanics, curvilinear coordinates, such as cylindrical polar coordinate and spherical polar coordinate, are often used to describe the geometrical shape of a blood vessel better. For a curvilinear coordinate system, an orthogonal natural basis, called covariant base vectors, are defined as  $\mathbf{G}_i$  in the reference configuration and  $\mathbf{g}_i$  in the deformed configuration.  $\mathbf{G}_i$  and  $\mathbf{g}_i$  need not to be of unit magnitude, and in general they depend on position.

Let us consider  $d\mathbf{b}$  as a differential vector in space. It can be written as

$$d\mathbf{b} = dz^{i}\mathbf{g}_{i} = dz^{1}\mathbf{g}_{1} + dz^{2}\mathbf{g}_{2} + dz^{3}\mathbf{g}_{3}$$

$$(3.1)$$

with respect to the deformed curvilinear coordinates  $z^i$ .

A reciprocal (contravariant) basis vectors  $\mathbf{G}^i$  in the reference configuration and  $\mathbf{g}^i$  in the deformed configuration are determined to satisfy the orthogonality condition via

$$\mathbf{G}_i \cdot \mathbf{G}^j = \delta_i^j, \qquad \mathbf{G}^i \cdot \mathbf{G}_j = \delta_i^i, \tag{3.2}$$

$$\mathbf{g}_i \cdot \mathbf{g}^j = \delta_i^j, \qquad \mathbf{g}^i \cdot \mathbf{g}_j = \delta_j^i \tag{3.3}$$

where  $\delta_i^j = 1$  if i = j and  $\delta_i^j = 0$  if  $i \neq j$ .

A differential vector  $d\mathbf{b}$  in equation (3.1) can be written using contravariant basis vector  $g^i$  as

$$d\mathbf{b} = dz_1 \mathbf{g}^i = dz_1 \mathbf{g}^1 + dz_2 \mathbf{g}^2 + dz_3 \mathbf{g}^3$$
(3.4)

with respect to the deformed curvilinear coordinate  $z_i$ .

In the Cartesian coordinate system,  $d\mathbf{b} = dx^i \mathbf{e}_i$ , where the normal basis  $\mathbf{e}_i$  is written as

$$\mathbf{e}_{i} = \frac{\partial \mathbf{b}}{\partial x^{i}} \tag{3.5}$$

Likewise, in curvilinear coordinate system, the vector  $d\mathbf{b}$  is expressed as  $d\mathbf{b} = dz^i \mathbf{g}_i$ , and orthogonal basis vector  $\mathbf{g}_i$  is

$$\mathbf{g}_i = \frac{\partial \mathbf{b}}{\partial z^i}.\tag{3.6}$$

Using a chain rule,  $\mathbf{g}_i$  can be rewritten as

$$\mathbf{g}_{i} = \frac{\partial \mathbf{b}}{\partial z^{i}} = \frac{\partial \mathbf{b}}{\partial x^{k}} \frac{\partial x^{k}}{\partial z^{i}} = \frac{\partial x^{k}}{\partial z^{i}} \mathbf{e}_{k}$$
(3.7)

$$\mathbf{g}_{i} = \frac{\partial \mathbf{b}}{\partial z^{i}} = \frac{\partial \mathbf{b}}{\partial z^{\alpha}} \frac{\partial z^{\alpha}}{\partial z^{i}} = \frac{\partial z^{\alpha}}{\partial z^{i}} \mathbf{g}_{\alpha}. \tag{3.8}$$

When the covariant basis vector  $\mathbf{g}_i$  are orthogonal at each point, the orthonormal vector  $\hat{\mathbf{e}}$  is determined by the division of the covariant basis vector by its magnitude, such that

$$\hat{\mathbf{e}}_i = \frac{\mathbf{g}_i}{|\mathbf{g}_i|} \text{ (no summation on i)} \tag{3.9}$$

where  $\hat{\mathbf{e}}_i$  does not change with position, and

$$\mid \mathbf{g}_i \mid = \sqrt{\mathbf{g}_i \cdot \mathbf{g}_i} = \sqrt{g_{ii}} \text{ (no summation)}.$$
 (3.10)

Basic manipulations of components for the curvilinear coordinate system are analogous

to those for the Cartesian coordinate system. However, the differentiation of a position vector with respect to the curvilinear coordinate system yields two terms. For example, a differential vector  $d\mathbf{v}$  can be rewritten as

$$\frac{\partial \mathbf{v}}{\partial z^m} = \frac{\partial}{\partial z^m} \left( v^i \mathbf{g}_i \right) = \frac{\partial v^i}{\partial z^m} \mathbf{g}_i + v^i \frac{\partial \mathbf{g}_i}{\partial z^m},\tag{3.11}$$

here the second term can be

$$\frac{\partial \mathbf{g}_i}{\partial z^m} = \frac{\partial}{\partial z^m} \left( \frac{\partial x^k}{\partial z^i} \mathbf{e}_k \right) = \frac{\partial^2 x^k}{\partial z^m \partial z^i} \mathbf{e}_k. \tag{3.12}$$

After substituting equation (3.8) into the second term in equation (3.11)

$$\frac{\partial \mathbf{g}_i}{\partial z^m} = \frac{\partial^2 x^k}{\partial z^m \partial z^i} \frac{\partial z^j}{\partial x^k} \mathbf{g}_j. \tag{3.13}$$

The equation of the balance of linear momentum is  $\operatorname{div}(\mathbf{t}) + \rho \mathbf{b} = \rho \mathbf{a}$ , where  $\mathbf{t}$  is the Cauchy stress tensor,  $\mathbf{b}$  is the body force vector, and  $\mathbf{a}$  is the acceleration vector. The divergence of a tensor  $\mathbf{t}$  in curvilinear coordinate system is given by

$$\operatorname{div}(\mathbf{t}) = \mathbf{g}^m \cdot \left( \frac{\partial t^{ij}}{\partial z^m} \mathbf{g}_i \otimes \mathbf{g}_j + t_{ij} \frac{\partial \mathbf{g}_i}{\partial z^m} \otimes \mathbf{g}_j + t^{ij} \mathbf{g}_i \otimes \frac{\partial \mathbf{g}_j}{\partial z^m} \right). \tag{3.14}$$

The deformation gradient tensor  $\mathbf{F}$  is the gradient of mapping function to describe the motion of a continuum. When a position vector for a material point in the undeformed configuration  $\mathbf{X}$  has displacement, the material point has new position  $\mathbf{x}$  in the deformed configuration. For an infinitesimal change of the position vector in the curvilinear coordinate system, the deformation gradient  $\mathbf{F}$  is the fundamental measure of the deformation as

$$\mathbf{F} = \frac{\partial \mathbf{x}}{\partial \mathbf{X}} = \frac{\partial x^i}{\partial X^J} \mathbf{g}_i \otimes \mathbf{G}^J = F_J^i \mathbf{g}_i \otimes \mathbf{G}^J. \tag{3.15}$$

where  $F_J^i = \frac{\partial x^i}{\partial X^J}$ . Then the determinant of the deformation gradient J is given by

$$J = \det \mathbf{F} = \frac{\mathbf{g}_1 \cdot (\mathbf{g}_2 \times \mathbf{g}_3)}{\mathbf{G}_1 \cdot (\mathbf{G}_2 \times \mathbf{G}_3)}.$$
 (3.16)

The covariant component of C is

$$\mathbf{C} = \left( F_A^i \mathbf{g}_i \otimes \mathbf{G}^A \right)^T \cdot \left( F_B^j \mathbf{g}_j \otimes \mathbf{G}^B \right)$$

$$= \left( F_A^i F_B^j g_{ij} \mathbf{G}^A \otimes \mathbf{G}^B \right)$$

$$= C_{AB} \mathbf{G}^A \otimes \mathbf{G}^B$$
(3.17)

# 3.2 Numerical analysis and approximation

The cylindrical coordinate is often used in vascular mechanics to describe the positions of material particles. It is appropriate to solve blood vessel problems since the base vectors of the curvilinear coordinate need not be independent of position. In this study, the positions of markers are determined in the Cartesian coordinate from the image processing, and then they are converted to the cylindrical polar coordinate.

#### 3.2.1 Coordinate transformation

The 3D positions of markers affixed to the specimen are obtained before and during the inflation test. The load-free state is regarded as the reference configuration, and the deformed state during the test is regarded as the deformed configuration. Because of the cylindrical shape of the vessel wall, the position of a marker (X, Y, Z) in the Cartesian coordinate system is converted to variables  $(\Theta, S, R)$  in the cylindrical polar coordinate system via

$$X - X_o = R\cos\Theta, \qquad Y - Y_o = R\sin\Theta, \qquad Z = S$$
 (3.18)

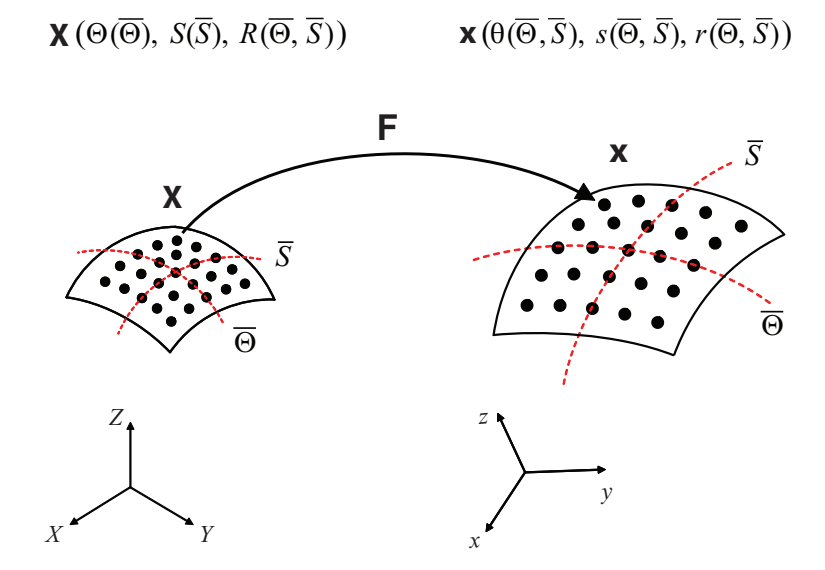


Fig. 3.1: The surfaces in the reference configuration and the deformed configuration are approximated by continuous functions of two variables,  $\overline{\Theta}$  and  $\overline{S}$ , convected to the surface. The deformation gradient of the surface corresponding to the mapping is denoted by  $\mathbf{F}$ .

where  $\{X_o, Y_o\}$  is the center-line approximated by the marker positions. Likewise, the position (x, y, z) in the deformed configuration is converted to variables  $(\theta, s, r)$  via

$$x - x_o = r\cos\theta, \qquad y - y_o = r\sin\theta, \qquad z = s$$
 (3.19)

The outer surfaces of the vessel wall are parameterized using two variables  $\overline{\Theta}$  and  $\overline{S}$ , which provide a convected curvilinear coordinate system for the surface during the deformation. The normalized variables  $\overline{S}$  and  $\overline{\Theta}$  can be obtained via

$$\overline{S} = \frac{2(S - S_{min})}{S_{max} - S_{min}} - 1 \tag{3.20}$$

$$\overline{\Theta} = \frac{2(\Theta - \Theta_{min})}{\Theta_{max} - \Theta_{min}} - 1, \tag{3.21}$$

and then  $-1 \leq \overline{S} \leq 1$  and  $-1 \leq \overline{\Theta} \leq 1$ .

All variables in the reference and deformed configurations are expressed as functions of

 $\overline{\Theta}$  and  $\overline{S}$ , as

$$\Theta = \Theta(\overline{\Theta}), \qquad S = S(\overline{S}), \qquad R = \hat{R}(\overline{\Theta}, \overline{S}),$$
 (3.22)

$$\theta = \hat{\theta}(\overline{\Theta}, \overline{S}), \qquad s = \hat{s}(\overline{\Theta}, \overline{S}), \qquad r = \hat{r}(\overline{\Theta}, \overline{S}).$$
 (3.23)

#### 3.2.2 Deformation gradient

The covariant base vectors of the surface,  $\mathbf{G}_i$  in the reference configuration and  $\mathbf{g}_i$  in the deformed configuration, are defined as

$$\mathbf{G}_i = \frac{\partial \mathbf{X}}{\partial \Sigma_i}, \qquad \mathbf{g}_i = \frac{\partial \mathbf{x}}{\partial \Sigma_i}$$
 (3.24)

where  $\Sigma_i$  are two variables convected to the surface  $\overline{\Theta}$  and  $\overline{S}$ .

In a convected curvilinear coordinate system, the 2D deformation gradient  $\mathbf{F}^*$  of the surface is given by

$$\mathbf{F}^* = \mathbf{g}_i \otimes \mathbf{G}^i \tag{3.25}$$

where  $\otimes$  denotes the tensor product. Since the covariant and contravariant base vectors are generally not orthonormal, local orthonormal base vectors  $\hat{\mathbf{E}}_i$  in the reference configuration and  $\hat{\mathbf{e}}_i$  in the current configuration are determined at each point as

$$\hat{\mathbf{E}}_1 = \frac{\mathbf{G}_1}{|\mathbf{G}_1|}, \qquad \hat{\mathbf{E}}_2 = \frac{\mathbf{G}_2 - (\mathbf{G}_2 \cdot \hat{\mathbf{E}}_1)\hat{\mathbf{E}}_1}{|\mathbf{G}_2 - (\mathbf{G}_2 \cdot \hat{\mathbf{E}}_1)\hat{\mathbf{E}}_1|}$$
 (3.26)

$$\hat{\mathbf{e}}_1 = \frac{\mathbf{g}_1}{|\mathbf{g}_1|}, \qquad \hat{\mathbf{e}}_2 = \frac{\mathbf{g}_2 - (\mathbf{g}_2 \cdot \hat{\mathbf{e}}_1)\hat{\mathbf{e}}_1}{|\mathbf{g}_2 - (\mathbf{g}_2 \cdot \hat{\mathbf{e}}_1)\hat{\mathbf{e}}_1|}$$
 (3.27)

where the subscripts 1 and 2 represent the circumferential and longitudinal directions, respectively.

The covariant and contravariant base vectors thus can be expressed in terms of the local orthonormal base vectors  $\hat{\mathbf{E}}_i$  or  $\hat{\mathbf{e}}_i$ . Finally, the 2D deformation gradient  $\mathbf{F}$  with respect to the local orthonormal base vector can be written as  $F_{pq} = \hat{\mathbf{e}}_p \cdot \mathbf{F}\hat{\mathbf{E}}_q$ .

#### 3.2.3 Approximation of the surface

The surfaces of the vessel wall are globally parameterized using two variables  $\overline{S}$  and  $\overline{\Theta}$ , which are convected to the two-dimensional curvilinear coordinate system. The surfaces of vessel wall in both configurations are approximated using Legendre polynomial functions, which make two variables orthogonal to each other.

The four functions  $(\hat{R}, \hat{\theta}, \hat{s}, \text{ and } \hat{r})$  in equation (3.22) and (3.23) are approximated by the finite series of continuous base functions of  $\overline{\Theta}$  and  $\overline{S}$ 

$$\left(\hat{R}, \hat{\theta}, \hat{s}, \hat{r}\right) = \sum_{j=1}^{nU} \alpha_j \phi_j(\overline{\Theta}, \overline{S})$$
(3.28)

where  $n^U$  is the number of degrees of the base function and  $\alpha_j$  is a parameter. The base function  $\phi_j$  is defined as a combination of Legendre polynomials of  $\overline{\Theta}$  and that of  $\overline{S}$ , that is,  $\phi_j(\overline{\Theta}, \overline{S}) = \psi_k(\overline{\Theta})\psi_l(\overline{S})$  where  $\psi_k$  and  $\psi_l$  represent  $k^{th}$  and  $l^{th}$  degrees of Legendre polynomials, respectively, for each variable. For example,  $\psi_0 = 1$  and  $n^{th}$  degree (n=1, 2, 3, ...) of Legendre polynomials of a variable x are given by

$$\psi_n(x) = \frac{1}{2^n n!} \frac{d^n}{dx^n} \left(x^2 - 1\right)^n. \tag{3.29}$$

In this study,  $3^{rd}$  and  $4^{th}$  degrees of Legendre polynomials are used in the longitudinal and circumferential directions, respectively.

In our pilot study, the edge of the surface domain has a large variation in stretch distribution, and so the accuracy of the Legendre polynomial approximation decreased near the edge of the domain. Once the coordinate was transformed to the cylindrical coordinate and the positions of markers were approximated, different areas of the central region of the domain were tested for determining the optimal area of the central region, which had a high accuracy of the approximation. The stretch distributions of a silicon tube, which has relatively uniform stretch distribution, with different areas of central region were compared to

each other. The central region of domain with  $-0.7 < \overline{\Theta} < 0.7$  and  $-0.7 < \overline{S} < 0.7$  showed nearly uniform stretch distribution, so that the reduced domain were used for stress-strain analysis.

#### 3.2.4 Least squares estimation

Let  $\Phi^{exp}(\overline{\Theta}_n, \overline{S}_n)$  be the experimental data of marker positions at a point  $(\overline{\Theta}_n, \overline{S}_n)$  for  $n = 1, 2, ..., n^D$ , where  $n^D$  is the number of markers. We used  $36 \pm 6$  markers in this study. Parameters  $\alpha_i$  for each approximation function can be estimated by the least squares method with an optimization function E

$$E = \sum_{n=1}^{nD} \left\{ \sum_{j=1}^{nU} \alpha_j \phi_j \left( \overline{\Theta}_n, \overline{S}_n \right) - \Phi_n^{exp} (\overline{\Theta}_n, \overline{S}_n) \right\}^2.$$
 (3.30)

Taking partial derivatives of E in equation (3.30) with respect to  $\alpha_i$ 

$$\frac{\partial E}{\partial \alpha_i} = 2 \sum_{n=1}^{nD} \left\{ \sum_{j=1}^{nU} \alpha_j \phi_j \left( \overline{\Theta}_n, \overline{S}_n \right) - \Phi_n^{exp} \left( \overline{\Theta}_n, \overline{S}_n \right) \right\} \phi_i \left( \overline{\Theta}_n, \overline{S}_n \right). \tag{3.31}$$

At the minimum,  $\partial E/\partial \alpha_i=0$ , which leads to the linear equation  $\mathbf{K}\boldsymbol{\alpha}=\mathbf{f}$ , where  $\boldsymbol{\alpha}=\{\alpha_1,...,\alpha_{nU}\}^T$  and

$$K_{ij} = \sum_{n=1}^{n} \phi_i(\overline{\Theta}_n, \overline{S}_n) \phi_j(\overline{\Theta}_n, \overline{S}_n)$$
(3.32)

$$f_{i} = \sum_{n=1}^{nD} \Phi_{n}^{exp}(\overline{\Theta}_{n}, \overline{S}_{n}) \phi_{i}(\overline{\Theta}_{n}, \overline{S}_{n}). \tag{3.33}$$

The fitting parameters  $\alpha$  for the Legendre polynomials can be obtained by solving the above linear equations using the experimental data.

$$\alpha = \left(\mathbf{L}^{\mathbf{T}}\mathbf{L}\right)^{-1}\mathbf{L}^{\mathbf{T}}\mathbf{\Phi}^{\mathbf{exp}} \tag{3.34}$$

where 
$$\mathbf{L} = \left\{\phi_1, \phi_2, ..., \phi_{NU}\right\}^T$$
.

#### 3.3 Thickness of the aortic wall

In the load-free state, the aortic wall thickness  $H_0$  at a certain position along the circumference is approximated by a curve fit to the measurements of aortic wall thickness at every 45 degrees, using the Fourier series

$$H_0(\theta) = a_0 + a_1 \cos(\theta) + a_2 \sin(\theta) + a_3 \cos(2\theta) + a_4 \sin(2\theta). \tag{3.35}$$

The aortic wall thickness during the inflation test in the deformed configuration can be calculated by the incompressibility condition (Carew et al., 1968), which means that the determinant of the deformation gradient is unity (det **F**=1). In 3D, the deformation gradient can be written as

$$\mathbf{F} = \begin{bmatrix} F_{11} & F_{12} & 0 \\ F_{21} & F_{22} & 0 \\ 0 & 0 & \lambda_3 \end{bmatrix}$$
 (3.36)

where  $\lambda_3 = h/H_0$ , h being the deformed wall thickness. The 1 and 2 directions are in-plane (i.e., circumferential and longitudinal directions) and the 3 direction out-of-plane (radial direction). From the incompressibility condition, the wall thickness during the deformation is given by

$$h = \frac{H_0}{F_{11}F_{22} - F_{12}F_{21}}. (3.37)$$

# 3.4 Curvature of the aortic wall

The principal curvature of the aortic wall is obtained by the first and second fundamental forms of a surface in differential geometry. We use the same parameters in the fundamental forms of a surface as parameters in our approximation, that is,  $\overline{S}$  and  $\overline{\Theta}$ .

The first fundamental form of a surface is

$$I = Ed\overline{S}^2 + 2Fd\overline{S}d\overline{\Theta} + Gd\overline{\Theta}^2 = d\mathbf{x} \cdot d\mathbf{x}$$
(3.38)

where

$$E = \left(\frac{\partial x}{\partial \overline{S}}\right)^2 + \left(\frac{\partial y}{\partial \overline{S}}\right)^2 + \left(\frac{\partial z}{\partial \overline{S}}\right)^2 \tag{3.39}$$

$$F = \frac{\partial x}{\partial \overline{S}} \frac{\partial x}{\partial \overline{\Theta}} + \frac{\partial y}{\partial \overline{S}} \frac{\partial y}{\partial \overline{\Theta}} + \frac{\partial z}{\partial \overline{S}} \frac{\partial z}{\partial \overline{\Theta}}$$
(3.40)

$$G = \left(\frac{\partial x}{\partial \overline{\Theta}}\right)^2 + \left(\frac{\partial y}{\partial \overline{\Theta}}\right)^2 + \left(\frac{\partial z}{\partial \overline{\Theta}}\right)^2. \tag{3.41}$$

The second fundamental forms of a surface are

$$II = Ld\overline{S}^2 + 2Md\overline{S}d\overline{\Theta} + Nd\overline{\Theta}^2 = -d\mathbf{x} \cdot d\hat{\mathbf{N}}$$
(3.42)

where

$$L = \frac{1}{\sqrt{EG - F^2}} \begin{vmatrix} \frac{\partial^2 x}{\partial \overline{S}^2} & \frac{\partial^2 y}{\partial \overline{S}^2} & \frac{\partial^2 z}{\partial \overline{S}^2} \\ \frac{\partial x}{\partial \overline{S}} & \frac{\partial y}{\partial \overline{S}} & \frac{\partial z}{\partial \overline{S}} \\ \frac{\partial x}{\partial \overline{\Theta}} & \frac{\partial y}{\partial \overline{\Theta}} & \frac{\partial z}{\partial \overline{\Theta}} \end{vmatrix}$$
(3.43)

$$M = \frac{1}{\sqrt{EG - F^2}} \begin{vmatrix} \frac{\partial^2 x}{\partial \overline{S} \partial \overline{\Theta}} & \frac{\partial^2 y}{\partial \overline{S} \partial \overline{\Theta}} & \frac{\partial^2 z}{\partial \overline{S} \partial \overline{\Theta}} \\ \frac{\partial x}{\partial \overline{S}} & \frac{\partial y}{\partial \overline{S}} & \frac{\partial z}{\partial \overline{S}} \\ \frac{\partial x}{\partial \overline{\Theta}} & \frac{\partial y}{\partial \overline{\Theta}} & \frac{\partial z}{\partial \overline{\Theta}} \end{vmatrix}$$
(3.44)

$$N = \frac{1}{\sqrt{EG - F^2}} \begin{vmatrix} \frac{\partial^2 x}{\partial \overline{\Theta}^2} & \frac{\partial^2 y}{\partial \overline{\Theta}^2} & \frac{\partial^2 z}{\partial \overline{\Theta}^2} \\ \frac{\partial x}{\partial \overline{S}} & \frac{\partial y}{\partial \overline{S}} & \frac{\partial z}{\partial \overline{S}} \\ \frac{\partial x}{\partial \overline{\Theta}} & \frac{\partial y}{\partial \overline{\Theta}} & \frac{\partial z}{\partial \overline{\Theta}} \end{vmatrix}$$
(3.45)

and the unit surface normal vector  $\hat{\mathbf{N}}$  is given by

$$\hat{\mathbf{N}} = \frac{\mathbf{g}_1 \times \mathbf{g}_2}{|\mathbf{g}_1 \times \mathbf{g}_2|}.\tag{3.46}$$

The detail derivatives of differentiations are introduced in Appendix B.

Let  $\kappa$  be a normal curvature and it has two extremal values, which are the principal curvature,  $\kappa_n$  (Struik, 1988),

$$\kappa = \frac{II}{I} = \frac{Ld\overline{\Theta}^2 + 2Md\overline{\Theta}d\overline{S} + Nd\overline{S}^2}{Ed\overline{\Theta}^2 + 2Fd\overline{\Theta}d\overline{S} + Gd\overline{S}^2}.$$
 (3.47)

Therefore, we have

$$(EG - F^2)\kappa^2 - (EN + GL - 2MF)\kappa + LN - M^2 = 0.$$
 (3.48)

The two extreme values of  $\kappa_n$  in equation (3.47) are two principal curvatures  $\kappa_1$  and  $\kappa_2$ . We assumed that the outer radii of curvatures of the aortic wall are

$$r_1 = \frac{1}{\kappa_1}, \qquad r_2 = \frac{1}{\kappa_2}.$$
 (3.49)

Here the sign convention is that the radius of curvature is positive if the center of curvature is on the r-negative side of the surface. The detail derivatives of the parameters are included in Appendix B.

# 3.5 Stress and strain analysis

The stretch  $\lambda_i$  is calculated at each point by

$$\lambda_i = \sqrt{\hat{\mathbf{E}}_i \cdot (\mathbf{F}^{*T} \mathbf{F}^*) \hat{\mathbf{E}}_i} (i=1, 2)$$
(3.50)

where subscript 1 and 2 denote the circumferential and the longitudinal directions, respectively. In the classical method, the relationship between the transmural pressure and the tension is referred to as Laplace's law, that is  $T = \frac{Pr}{h}$ , where T is the tension in the walls, P is the transmural pressure across the vessel wall, r is the radius of the vessel, and h is the

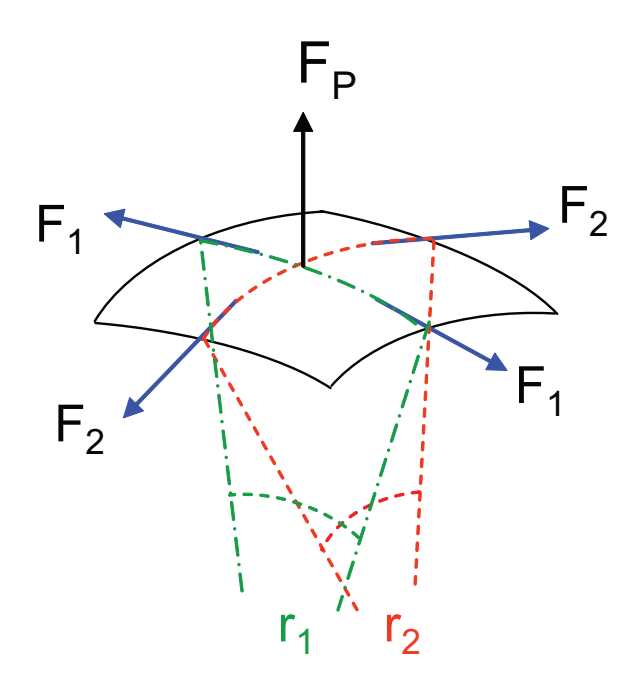


Fig. 3.2: Free body diagram of membrane tissue.

thickness of the wall. The higher pressure difference the more tension, the thicker wall the less tension, and the bigger radius the more tension there is. However, previous studies using this equation do not take into account changes in radius or tension along the circumference. In this study, the radius of the aorta depends on the circumferential position. Thus, the membrane hypothesis was applied to the aortic tissue to determine stress. The effect of bending throughout the vascular wall was so small that it was ignored when the aorta was loaded.

For a small section of the aortic segment, depicted in Fig. 3.2, the relationship of the transmural pressure and the tension was derived in the similar way with the Laplace law. Three forces are acting upon the wall: one due to pressure  $(F_P)$  acting radially and the others due to tensions  $(F_1$  and  $F_2)$  acting tangentially in two principal directions (S1 and S2). From the equilibrium of forces,

$$F_P = F_1 + F_2. (3.51)$$

From the shell membrane equilibrium equation,

$$\frac{T_1}{r_1} + \frac{T_2}{r_2} = P (3.52)$$

where  $T_1$  and  $T_2$  are membrane principal stress resultants per unit length in circumferential and longitudinal direction, respectively. Here, the local radius of curvature of the membrane  $r_1$  and  $r_2$  in circumferential and longitudinal direction, respectively, are calculated by the classical differential geometry of the surface as explained in the previous section.

For a cylindrical polar model, the mean radius of the curvature in the longitudinal direction is much larger than that in the circumferential direction  $(r_2 \gg r_1)$ . Therefore, equation (3.52) can be rewritten in terms of the mean circumferential Cauchy stress  $\sigma_1$ , that is  $T_1 = \sigma_1/h$ . The mean circumferential stress  $\sigma_1$  for each circumferential region can be estimated by

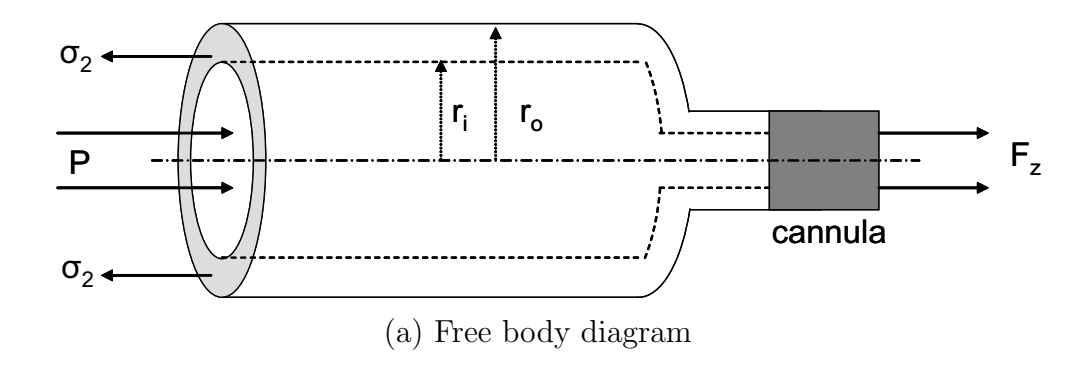
$$\sigma_1 = \frac{P(r_1 - h)}{h}.\tag{3.53}$$

Here, we assume that stress  $\sigma_1$  is the circumferential stress of the midwall.

Let us consider stress in the longitudinal direction. Bending of the aorta in vivo during the cardiac cycle is negligible (Choi et al., 2009) and we assume that the blood vessel has no bending moment applied at the end during the inflation test. During the inflation test, the blood vessel wall thickness (h) depends on its circumferential location ( $\theta$ ). The estimation of the aortic wall thickness was addressed in previous section (equation (3.37)). The bending moment M on the vessel wall

$$M = \int_0^{2\pi} (\sigma_2 x') r_m h d\theta = 0 \tag{3.54}$$

where  $\sigma_2$  is the longitudinal stress on the vessel wall, and  $r_m$  is the mean radius of curvature at the midwall. The distance  $x' = x - \bar{x}$  as shown in Fig. 3.3 (b), where  $\bar{x}$  is the centroid. Because of the asymmetry, the centroid of area is not same of middle of a ring. The



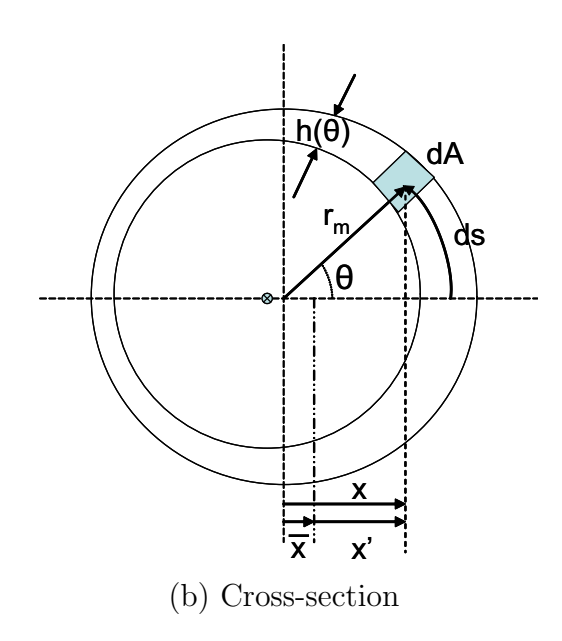


Fig. 3.3: (a) Free body diagram of a blood vessel sample during the inflation test and (b) the cross-section of the aortic wall.

centroid,  $\bar{x}$ , is calculated by

$$\bar{x} = \frac{1}{A} \int_0^{2\pi} x dA = \frac{1}{A} \int_0^{2\pi} \cos \theta r_m^2 h d\theta$$
 (3.55)

where  $x = r \cos \theta$ .

Because of the asymmetry of the aortic wall thickness, the cross-sectional area of the wall (A) and the centroid of area  $(\bar{x})$  can be calculated as functions of  $\theta$ . The piecewise area of the aortic wall is dA = hds, where s is the arc of circular shape of the aortic ring. If  $\theta$  is

very small,  $ds = r_m d\theta$ . The total cross-sectional area of the aortic ring, A, is given by

$$A = \int_0^{2\pi} \mathrm{d}A = \int_0^{2\pi} r_m h \mathrm{d}\theta \tag{3.56}$$

. Let the longitudinal stress assume  $\sigma_2 = ax' + b$ , where a and b are constants. The forces in longitudinal direction during the inflation test reach the equilibrium and thus

$$\int_0^{2\pi} \sigma_2 h r_m d\theta = P\pi (r_1 - h)^2 + F_z.$$
 (3.57)

where  $F_z$  is axial force to be applied the specimen during the inflation test. In equation (3.54) and equation (3.57),  $\sigma_2$  is substituted in terms of a and b by the assumption  $\sigma_2 = ax' + b$ . Then these two equations are arranged in matrix form as

$$\begin{bmatrix}
\int_0^{2\pi} x'^2 h r_m d\theta & \int_0^{2\pi} x' h r_m d\theta \\
\int_0^{2\pi} x' h r_m d\theta & \int_0^{2\pi} h r_m d\theta
\end{bmatrix}
\begin{cases} a \\ b \end{cases} = 
\begin{cases} 0 \\ P\pi r_i^2 + F_z \end{cases}.$$
(3.58)

Two constants a and b can be estimated using Gaussian quadrature (see Appendix B.2), and the longitudinal stress  $\sigma_2$  is determined.

In order to estimate material stiffness, the circumferential stiffness  $k_1(P_i)$  is calculated by fitting a  $6^{th}$  order of polynomial function to the stress-stretch curve. That is, the circumferential stiffness in this study is defined as a tangent of the mean stress-stretch curve at the transmural pressure  $P_i$  such that

$$k_1(P_i) = \frac{\partial \sigma_1}{\partial \lambda_1} |_{\lambda_1(P_i)} = \frac{\sigma_1 (\lambda_1 + \Delta \lambda_1) - \sigma_1 (\lambda_1 - \Delta \lambda_1)}{2\Delta \lambda_1}.$$
 (3.59)

To estimate the structural stiffness during the cardiac cycle, the pressure-strain elastic modulus  $E_p$  can also be calculated.  $E_p$  was introduced by Peterson et al. (1960) and after that many others adopted this pressure-diameter relation. The pressure-strain elastic modulus represents distensibility of a blood vessel by  $\Delta P/\Delta \epsilon$ , where  $\Delta P$  is the maximum pulse

pressure between the diastolic state and the systolic state and  $\Delta \epsilon$  is the change in strain during the same period. The pressure-strain elastic modulus resulted from both wall stiffness and the geometry of the blood vessel. Originally it is expressed as

$$E_p = \frac{P_{sys} - P_{dia}}{\left(D_{sys} - D_{dia}\right)/D_{dia}} \tag{3.60}$$

where subscripts sys and dia denote the systolic and diastolic conditions, respectively, and D is the diameter of lumen (Feigl et al., 1963). In this study, the denominator of the equation (3.60) was divided by  $D_o$ , which is the diameter of the lumen at the load-free state. Thus, equation (3.60) can be rewritten as

$$E_p = \frac{P_{sys} - P_{dia}}{\left(\lambda_{sys} - \lambda_{dia}\right) / \lambda_{dia}} \tag{3.61}$$

The systolic pressure and diastolic pressure have been assumed  $P_{sys}$ =15.20 kPa (114 mm Hg) and  $P_{dia}$ =10.13 kPa (76 mm Hg), respectively. These pressures were determined when the external pressure by the surrounding organ and tissue was considered as 5% of the transmural pressure (Zhang et al., 2005).

## 3.6 Statistical analysis

The mean of the computed values, such as stretch, stress, and stiffness, for the four circumferential regions of the aorta are compared statistically. The mean of a data set  $x_i$  ( $i = 1, 2, \dots, N$ ) is defined as

$$\bar{x} = \frac{1}{N} \sum_{i=1}^{N} x_i \tag{3.62}$$

and the standard deviation (SD) is computed via

$$SD = \sqrt{\frac{\sum_{i=1}^{N} (x_i - \bar{x})^2}{N - 1}}$$
 (3.63)

All aorta specimens are assumed to be independent statistical samples. Due to an increased chance of an error in doing multiple two-sample t-tests, ANOVA is suitable in comparing more than two. Hence, the significant difference among the four regions and each pairs of regions are evaluated by using one-way repeated measures ANOVA, which generalizes t-test to more than two groups, with Sidak adjustment. Also, the significant difference between two longitudinal portions for each region is evaluated by two-sample t-test. The difference is considered significant when p < 0.05.

# Chapter 4

# CONSTITUTIVE RELATIONS AND PARAMETERS

#### 4.1 Constitutive relations

The energy equation is

$$\rho_o \frac{d\epsilon}{dt} = \mathbf{P}^T : \frac{d\mathbf{F}}{dt} - \nabla_0 \cdot \mathbf{q}_0 + \rho_o g \tag{4.1}$$

where  $\rho_0$  is mass density,  $\epsilon$  the internal energy density defined per unit mass,  $\mathbf{P}$  the first Piola-Kirchhoff stress tensor,  $\nabla_0$  the del operator  $(\nabla_0 = \frac{\partial()}{\partial \mathbf{X}})$ ,  $\mathbf{q}_0$  the heat flux vector, and g a heat addition defined per unit mass. The internal energy is related to the Helmholtz potential  $\psi$  and entropy  $\eta$ , that is,  $\epsilon = \psi + \eta T$ , where T is the temperature.

For an isothermal process with no heat transfer (i.e. T=costant,  $\mathbf{q}_0 = 0$ ), the equation (4.1) yields

$$\left(-\rho_0 \frac{d\psi}{d\mathbf{F}} + \mathbf{P}^T\right) : \frac{d\mathbf{F}}{dt} = 0 \tag{4.2}$$

and the first Piola-Kirchhoff stress tensor  $\mathbf{P}$  can be

$$\mathbf{P}^T = \rho_o \frac{\partial \psi}{\partial \mathbf{F}} \longleftrightarrow \mathbf{P} = \rho_o \frac{\partial \psi}{\partial \mathbf{F}^T}.$$
 (4.3)

The Helmholtz potential  $\psi$  and the strain-energy W are related in an isothermal process, that is,  $\rho_o \psi(\mathbf{F}) = W(\mathbf{F})$ . From the material frame indifference

$$\frac{\partial \psi}{\partial \mathbf{F}^T} = 2 \frac{\partial \psi}{\partial \mathbf{C}} \cdot \mathbf{F}^T \tag{4.4}$$

where  $\mathbf{C} = \mathbf{C}^T$  and  $\mathbf{C} = \mathbf{F}^T \cdot \mathbf{F}$ . From equation (4.3) and (4.4), the first Piola-Kirchhoff stress tensor

$$\mathbf{P} = 2\frac{\partial W}{\partial \mathbf{C}} \cdot \mathbf{F}^T. \tag{4.5}$$

The alternate constitutive relations for the Cauchy stress can be written as (using  $\hat{\mathbf{t}} = \frac{1}{J}\mathbf{F}\cdot\mathbf{P}$ )

$$\hat{\mathbf{t}} = \frac{2}{J} \mathbf{F} \cdot \frac{\partial W}{\partial \mathbf{C}} \cdot \mathbf{F}^T \tag{4.6}$$

which is defined as the actual acting force on a body over the current area. However, equation (4.6) does not take into account the incompressibility constraint ( $J = \rho_0/\rho = 1$ ). After applying the constraint, equation (4.6) is rewritten as

$$\mathbf{t} = -p\mathbf{I} + 2\mathbf{F} \cdot \frac{\partial W}{\partial \mathbf{C}} \cdot \mathbf{F}^{T}$$
(4.7)

where p is a Lagrangian multiplier, which depends on position and time. Each component of equation (4.7) is

$$t_{11} = -p + \hat{t}_{11}$$

$$t_{22} = -p + \hat{t}_{22}$$

$$t_{33} = -p + \hat{t}_{33}.$$

$$(4.8)$$

The strain energy function W of vascular tissue is a function of the right Cauchy-Green deformation tensor as

$$W = W(C_{ij}), \quad \text{where } i, j = 1, 2, 3.$$
 (4.9)

Here 1, 2, and 3 denote the circumferential, axial, and radial directions, respectively.

For a general hyperelastic behavior, equation (4.6) can be written with an index notation as

$$\hat{t}_{ij} = \frac{2}{J} F_{iA} \frac{\partial W}{\partial C_{AB}} F_{jB}, \quad \text{where } i, j, A, B = 1, 2, 3.$$
(4.10)

During the inflation test, the deformation gradient is assumed to be

$$\mathbf{F} = \begin{bmatrix} F_{11} & F_{12} & 0 \\ F_{21} & F_{22} & 0 \\ 0 & 0 & \lambda_3 \end{bmatrix} = \begin{bmatrix} \lambda_1 & 0 & 0 \\ 0 & \lambda_2 & 0 \\ 0 & 0 & \lambda_3 \end{bmatrix}$$
(4.11)

where  $\lambda_3 = h/H_0$  based on the incompressibility assumption. The right Cauchy green tensor  ${\bf C}$  becomes

$$\mathbf{C} = \begin{bmatrix} \lambda_1^2 & 0 & 0 \\ 0 & \lambda_2^2 & 0 \\ 0 & 0 & \lambda_3^2 \end{bmatrix}. \tag{4.12}$$

Based on the thin-wall analysis (Holzapfel et al., 2000), let the stress in the radial direction  $t_{33}$  be zero. Then the Lagrangian multiplier  $p = \hat{t}_{33}$ . Consequently, equation (4.8) is rewritten as

$$t_{11} = \hat{t}_{11} - \hat{t}_{33} = \frac{2}{J} F_{1A} \frac{\partial W}{\partial C_{AB}} F_{1B} - \frac{2}{J} F_{3A} \frac{\partial W}{\partial C_{AB}} F_{3B}$$

$$t_{22} = \hat{t}_{22} - \hat{t}_{33} = \frac{2}{J} F_{2A} \frac{\partial W}{\partial C_{AB}} F_{2B} - \frac{2}{J} F_{3A} \frac{\partial W}{\partial C_{AB}} F_{3B}$$

$$t_{33} = 0$$

$$(4.13)$$

#### 4.1.1 Constitutive models

#### Mixture model

In this study, the constitutive model based on a constrained mixture approach (Baek et al., 2006; Humphrey and Rajagopal, 2002) has been adopted to describe the mechanical properties of the aorta. Let the natural configuration represent the stress-free state of a constituent of aortic wall. Deformation is considered in two steps: first, mapping from the natural configuration (stress-free state) of each constituent to the reference configuration (in vivo state), second mapping from the reference configuration to the deformed configuration.

The arterial wall is assumed to be a mixture of the constituent of i, such as elastin (e), multiple collagen families  $(1, \dots, k, \dots, 4)$ , and smooth muscle (m). The strain energy W of the mixture per unit volume is

$$W = \Sigma_i \nu^i W^i = \nu^e W^e + \Sigma_k \nu^k W^k + \nu^m W^m \tag{4.14}$$

where  $\nu^i$  are the unit reference volume for each constituent of i. It has been assumed that there is no active tone presented during the inflation test in this study.

For the elastin, a mapping from the natural configuration to the reference configuration (in vivo state)  $\hat{\mathbf{G}}^e$  is defined as

$$\hat{\mathbf{G}}^e = \operatorname{diag}\left\{\hat{G}_1^e, \hat{G}_2^e, \hat{G}_3^e\right\} \tag{4.15}$$

such that the mapping of the elastin from the natural configuration to the deformed configuration

$$\mathbf{F}_n^e = \mathbf{F} \cdot \hat{\mathbf{G}}^e \tag{4.16}$$

and therefore

$$\mathbf{C}_{n}^{e} = (\mathbf{F}_{n}^{e})^{T} \cdot \mathbf{F}_{n}^{e} = (\hat{\mathbf{G}}^{e})^{T} \cdot \mathbf{C} \cdot \hat{\mathbf{G}}^{e}. \tag{4.17}$$

The Cauchy stress  $\hat{\mathbf{t}}$  of elastin can be rewritten in terms of  $\mathbf{F}_n^e$  and  $\mathbf{C}_n^e$  as

$$2\mathbf{F} \frac{\partial W^{e}}{\partial \mathbf{C}^{e}} \mathbf{F}^{T} = 2F_{iA} \frac{\partial W^{e}}{\partial C_{AB}^{e}} F_{Bj}^{T}$$

$$= 2F_{iA} \left( \hat{G}_{Ak}^{e} \frac{\partial W^{e}}{\partial C_{n[kl]}^{e}} \hat{G}_{lB}^{eT} \right) F_{Bj}^{T}$$

$$= 2F_{n[ik]}^{e} \frac{\partial W^{e}}{\partial C_{n[kl]}^{e}} F_{n[lj]}^{eT}$$

$$= 2\mathbf{F}_{n}^{e} \frac{\partial W^{e}}{\partial \mathbf{C}_{n}^{e}} \mathbf{F}_{n}^{eT}$$

$$= 2\mathbf{F}_{n}^{e} \frac{\partial W^{e}}{\partial \mathbf{C}_{n}^{e}} \mathbf{F}_{n}^{eT}$$

$$(4.18)$$

Strain energy of elastin  $W^e$  per unit reference volume are given by

$$W^{e}\left(\mathbf{C}_{n}^{e}\right) = \frac{c_{1}}{2} \left\{ C_{n[11]}^{e} + C_{n[22]}^{e} + C_{n[33]}^{e} - 3 \right\}$$

$$(4.19)$$

where  $C_{n[11]}^e, C_{n[22]}^e$ , and  $C_{n[33]}^e$  are components of  $C_n^e$ ,

and

$$2F_{n[ik]}^e F_{n[jl]}^e \frac{\partial W^e}{\partial C_{n[kl]}^e} = c_1 \left( \hat{G}_i^e \lambda_i \right) \left( \hat{G}_j^e \lambda_j \right) \frac{\partial W^e}{\partial C_{n[kl]}^e}. \tag{4.20}$$

Each component of equation (4.20) is

$$2F_{n[i1]}^{e} \frac{\partial W^{e}}{\partial C_{n[11]}^{e}} F_{n[1j]}^{eT} = 2F_{n[11]}^{e} \frac{\partial W^{e}}{\partial C_{n[11]}^{e}} F_{n[11]}^{eT} = c_{1} \left( \hat{G}_{1}^{e} \lambda_{1} \right)^{2}$$

$$2F_{n[i2]}^{e} \frac{\partial W^{e}}{\partial C_{n[22]}^{e}} F_{n[2j]}^{eT} = 2F_{n[22]}^{e} \frac{\partial W^{e}}{\partial C_{n[22]}^{e}} F_{n[22]}^{eT} = c_{1} \left( \hat{G}_{2}^{e} \lambda_{2} \right)^{2}$$

$$2F_{n[i3]}^{e} \frac{\partial W^{e}}{\partial C_{n[33]}^{e}} F_{n[3j]}^{eT} = 2F_{n[33]}^{e} \frac{\partial W^{e}}{\partial C_{n[33]}^{e}} F_{n[33]}^{eT} = c_{1} \left( \hat{G}_{3}^{e} \lambda_{3} \right)^{2}.$$

$$(4.21)$$

In the radial direction, the homeostatic tensor  $\hat{G}_3^e$  and stretch of elastin  $\lambda_3$  can be substituted by the circumferential and axial components from the incompressibility constraint, such that

$$\hat{G}_{3}^{e}\lambda_{3} = \frac{1}{\hat{G}_{1}^{e}\hat{G}_{2}^{e}\lambda_{1}\lambda_{2}}.$$
(4.22)

For the collagen fiber, the stretch of  $k^{th}$  collagen fiber family in the natural configuration (stress-free state) from the deformed configuration is defined as

$$\lambda_n^k = G_h^c \lambda^k \tag{4.23}$$

where  $G_h^c$  is homeostatic stretch. The stretch of the  $k^{th}$  collagen fiber is

$$\lambda^{k} = \sqrt{\left(\lambda_{1} \sin \alpha^{k}\right)^{2} + \left(\lambda_{2} \cos \alpha^{k}\right)^{2}},\tag{4.24}$$

where  $\alpha^k$  is the orientation of the  $k^{th}$  collagen fiber family. The Cauchy stress of the collagen fiber family

$$F_{iA}F_{jB}\frac{\partial W^k}{\partial C_{AB}^k} = \lambda_i^{k^2}\frac{\partial W^k}{\partial \lambda_i^{k^2}} = \lambda_i^{k^2}\frac{\partial W^k}{\partial \lambda_n^{k^2}}\frac{\partial \lambda_n^{k^2}}{\partial \lambda_i^{k^2}},$$
(4.25)

where the strain energy of collagen  $W^k$  per unit reference volume is given by

$$W^{k}\left(\lambda_{n}^{k}\right) = \frac{c_{2}}{4c_{3}}\left[\exp\left\{c_{3}\left(\lambda_{n}^{k^{2}} - 1\right)^{2}\right\} - 1\right]$$

$$(4.26)$$

and therefore

$$\frac{\partial W^k}{\partial \lambda_n^{k^2}} = \frac{c_2}{2} \left[ \exp\left\{ c_3 \left( \lambda_n^{k^2} - 1 \right)^2 \right\} \right] \left( \lambda_n^{k^2} - 1 \right) \tag{4.27}$$

$$\frac{\partial \lambda_n^{k^2}}{\partial \lambda_1^{k^2}} = G_h^{c^2} \left( \sin \alpha^k \right)^2$$

$$\frac{\partial \lambda_n^{k^2}}{\partial \lambda_2^{k^2}} = G_h^{c^2} \left(\cos \alpha^k\right)^2. \tag{4.28}$$

For the smooth muscle, the stretch in the natural configuration from the deformed configuration is defined as

$$\lambda_n^m = G_h^m \lambda_1 \tag{4.29}$$

where  $G_h^m$  is homeostatic stretch. The Cauchy stress of the smooth muscle

$$F_{iA}F_{jB}\frac{\partial W^m}{\partial C_{AB}^m} = \lambda_i^{m2}\frac{\partial W^m}{\partial \lambda_i^{m2}} = \frac{\partial W^m}{\partial \lambda_n^{m2}}\frac{\partial \lambda_n^{m2}}{\partial \lambda_i^{m2}},\tag{4.30}$$

where the strain energy of smooth muscle  $W^m$  per unit reference volume is given by

$$W^{m}(\lambda_{n}^{m}) = \frac{c_{4}}{4c_{5}} \left[ \exp \left\{ c_{5} \left( (\lambda_{n}^{m})^{2} - 1 \right)^{2} \right\} - 1 \right]$$
(4.31)

and therefore

$$\frac{\partial W^m}{\partial \lambda_n^{m2}} = \frac{c_4}{2} \left[ \exp\left\{ c_5 \left( \lambda_n^{m2} - 1 \right)^2 \right\} \right] \left( \lambda_n^{m2} - 1 \right) \tag{4.32}$$

$$\frac{\partial \lambda_n^{m2}}{\partial \lambda_1^{m2}} = G_h^{m2}$$

$$\frac{\partial \lambda_n^{m2}}{\partial \lambda_2^{m2}} = 0. {(4.33)}$$

The volume fraction of the constituent of i is prescribed as following (He and Roach, 1994; Holzapfel et al., 2002; Menashi et al., 1987):

$$\nu^e = 0.2, \qquad \nu^m = 0.2, \qquad \nu^k = [0.1, 0.1, 0.4, 0.4] (1 - \nu^e - \nu^m).$$
 (4.34)

In this study, a four-fiber family has been considered. It is assumed that a one-fiber family is aligned to the circumferential direction, another the longitudinal direction. The other a two-fiber family is disposed helically with respect to the longitudinal direction.

$$\alpha^{k} = [0^{\circ}, 90^{\circ}, \alpha^{\circ}, (180 - \alpha)^{\circ}]$$

Parameters  $[c_1, c_2, c_3, c_4, c_5, G_1^e, G_2^e, G_h^c, G_h^m, \alpha]$  to describe the mechanical behavior of the aorta in this study are assumed to be unknown and determined by the parameter estimation.

#### 4.1.2 Parameter estimation

The constitutive parameters are estimated by fitting the inflation test data of a healthy porcine thoracic aorta at three different longitudinal stretches of 1.35, 1.40. and 1.45. The stretch and stress are normalized with homeostatic stress and stretch, which are obtained at 95 mm Hg at the longitudinal stretch of 1.35. The magnitude of normalized stretch and stress depend on the homeostatic ones, but it does not effect the shape of curve in the stress-stretch plot. Parameters are determined by minimizing the objective function  $\tilde{e}$  which represents differences between the theoretically predicted results and experimentally calculated results based on measurements in the two stretching directions

$$\tilde{e} = \sum_{k=1}^{m} \left[ \frac{(t_{11}|_t - t_{11}|_e)_k^2 + (t_{22}|_t - t_{22}|_e)_k^2}{\sigma_h^2} \right]$$
(4.35)

where the subscripts t and e denote theoretical and experimental values, respectively, and  $\sigma_h$  is the homeostatic stress of the artery.

# Chapter 5

# RESULTS AND DISCUSSION

# 5.1 Validation of the experimental measurements

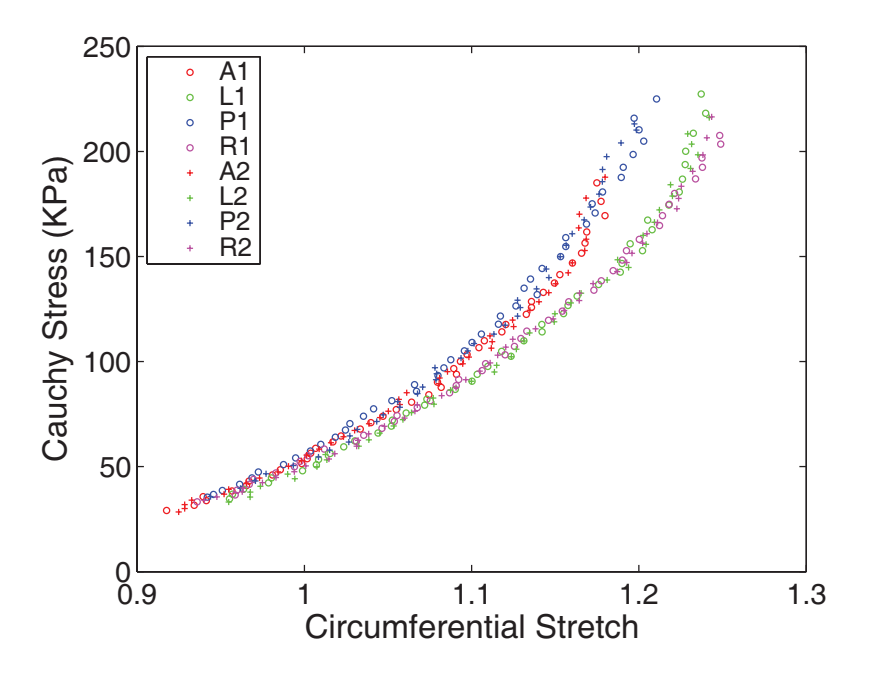


Fig. 5.1: Comparison of stretch-stress plots before and after the rotation of a specimen. A: anterior region, L: left lateral region, P: posterior region, and R: right lateral region.

In our pilot study, the inflation test for the same region of an aorta was repeated after rotating the specimen under the same experimental conditions in order to ensure the reproducibility of our experimental results. Fig. 5.1 shows an example of stress-stretch response of

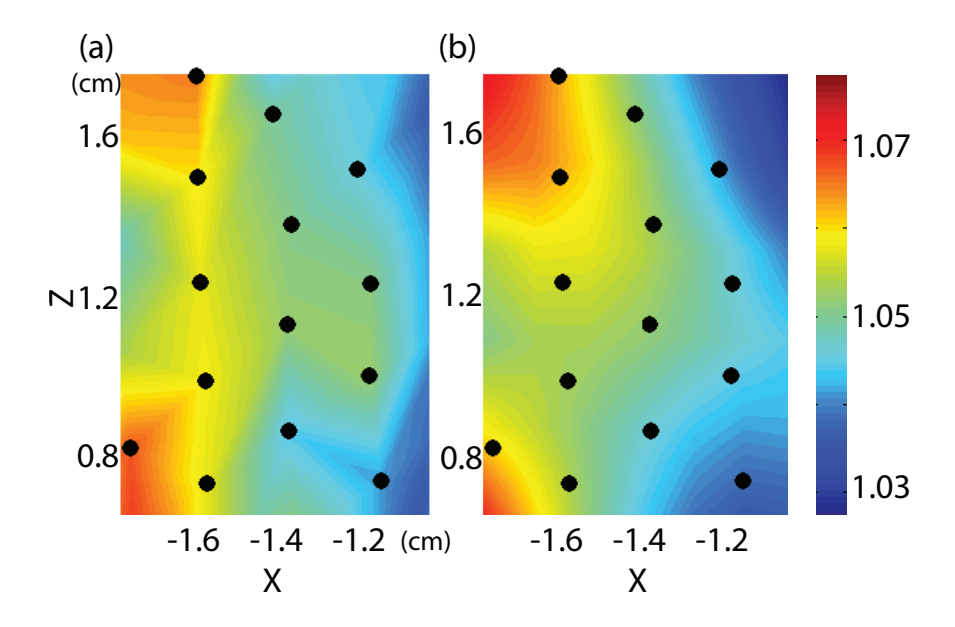


Fig. 5.2: Comparison of the distribution of circumferential stretch between two methods: (a) stretch distribution by linear approximation with triangular elements and (b) stretch distribution by the approximation in the present study. Black dots represent markers in the deformed configuration.

an aorta before and after rotating. There was little difference in the stress-stretch responses after the rotation.

# 5.2 Validation of the approximation using continuous functions

A flexible silicone tube, which has nearly uniform radius and stretch distributions, was used to compare the circumferential stretch distributions obtained by two approximations: one was derived from the continuous functions explained in the previous chapter; and the other was based on linear polynomial approximation with triangular elements, which is a typical method used in finite element analysis and previous experimental studies (Hu et al., 2007; Saravanan et al., 2006). Although both stretch distributions looked similar, the stretch distribution obtained by the approximation using continuous functions showed smoother and slightly higher variation than that obtained by linear approximation (Fig 5.2).

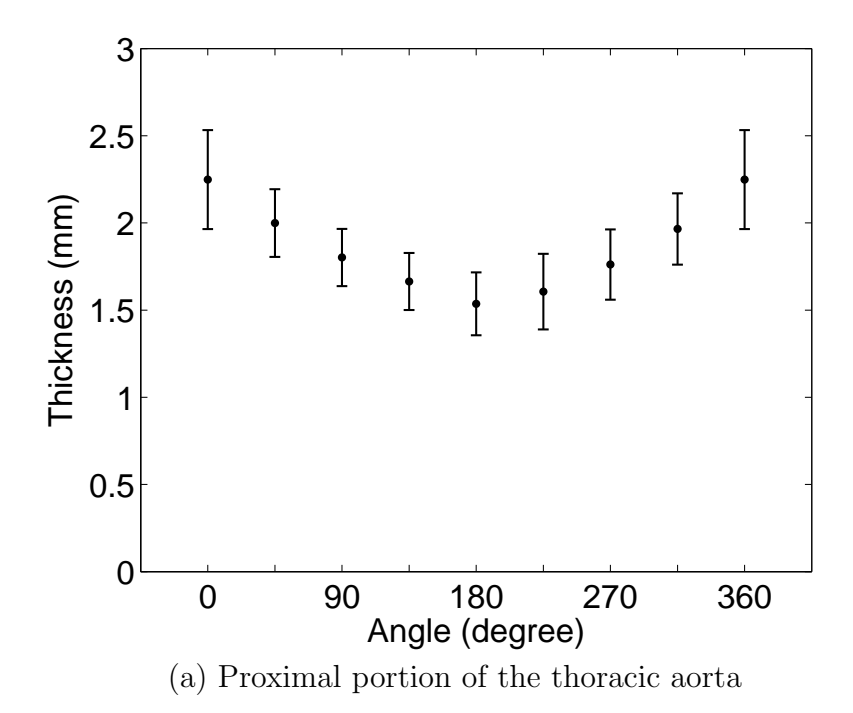
In addition to the circumferential stretch, the outer radii of small cylindrical rods were investigated, assuming each rod had a constant radius. Microspheres (i.e. markers) with a mean diameter of 196, 390, and 550  $\mu$ m were attached onto the surfaces of two rods with different diameters of 1.27 and 1.91 cm using adhesive and a pulled glass micropipette. Pairs of digital images of markers on the specimen were obtained and processed to extract the positions of markers. The radii of the specimens with different sizes of markers were estimated by the method described in the previous chapter. The radii of the specimens were also estimated by fitting the equation of a perfect cylinder with the marker positions using the least squares method. The entire procedure was repeated three times for each specimen and the average values of the radii were obtained. Overall, the radius difference between the two methods was less than 2%.

#### 5.3 Variation of the aortic wall thickness

Aortic wall thickness varied gradually along the circumference (Fig. 5.3). The anterior region was thickest ( $2.2 \pm 0.3$  mm for the proximal thoracic aorta and  $1.8 \pm 0.3$  mm for the distal thoracic aorta) and the posterior region was thinnest ( $1.5 \pm 0.2$  mm for the proximal and  $1.2 \pm 0.1$  mm for the distal). The ratio of the mean wall thickness of the anterior region to the posterior was  $1.5 \pm 0.1$  for the proximal and  $1.6 \pm 0.2$  for the distal. Although the wall thickness decreased as the distance from the heart further, the ratio remained similar.

# 5.4 Radius of curvature of the aortic wall

The outer radius of the aorta responded to the change of pressure as shown in Fig. 5.4. At the load-free state, the mean and standard deviation of the radius of the proximal aorta for each region were  $8.5 \pm 0.8$  (A),  $8.8 \pm 1.0$  (L),  $8.1 \pm 1.0$  (P), and  $8.7 \pm 0.9$  mm (R). It showed that the mean radius of the posterior region was slightly smaller than other circumferential regions. On the other hand, the radii of the four regions became nearly uniform as the



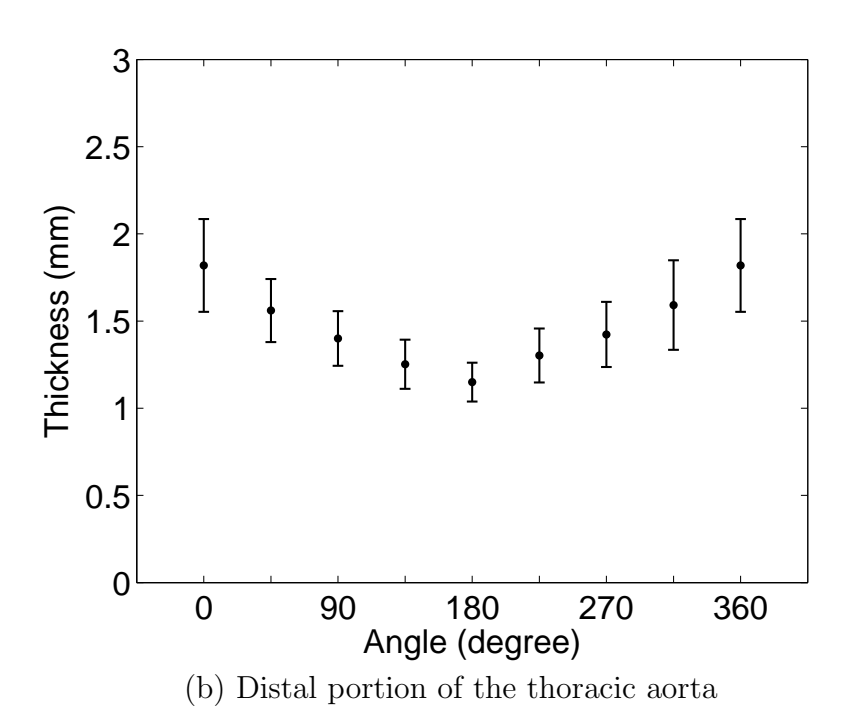


Fig. 5.3: Mean and standard deviation of the aortic wall thickness along the circumference: (a) the proximal thoracic aorta, (b) the distal thoracic aorta. 0°: the anterior region, 90°: left lateral region, 180°: posterior region, and 270°: right lateral region

pressure was applied during the inflation test. At the transmural pressure of 12.00 kPa, the mean and standard deviation of the radius for each region were  $10.0 \pm 0.7$  mm (A),  $10.1 \pm$ 

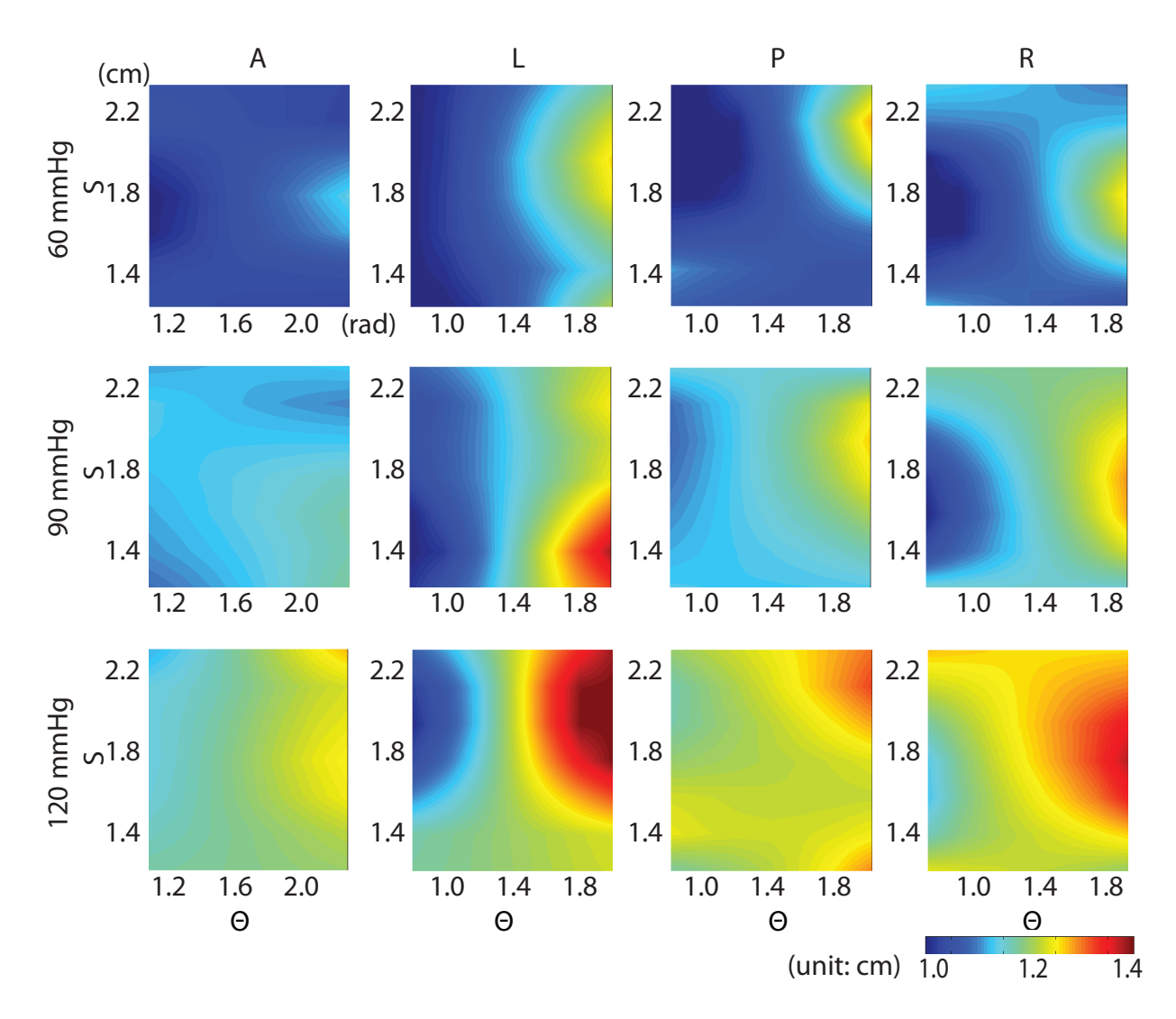


Fig. 5.4: A representative example of the distributions of the radius of curvature for the four circumferential regions of one thoracic aorta sample at transmural pressures of 8.00 kPa (60 mm Hg), 12.00 kPa (90 mm Hg), and 16.00 kPa (120 mm Hg), respectively, and a longitudinal stretch ratio ( $\Lambda_Z$ ) of 1.35.

0.7 mm (L),  $10.2 \pm 0.7 \text{ mm (P)}$ , and  $10.1 \pm 0.8 \text{ mm (R)}$ .

### 5.5 Stress and strain relationship of the aorta

The circumferential stretch and the circumferential Cauchy stress during the inflation test at three fixed longitudinal stretch ratios of 1.35, 1.40, and 1.45 were computed for each circumferential region of each specimen. In a repeated cyclic loading condition, loading and

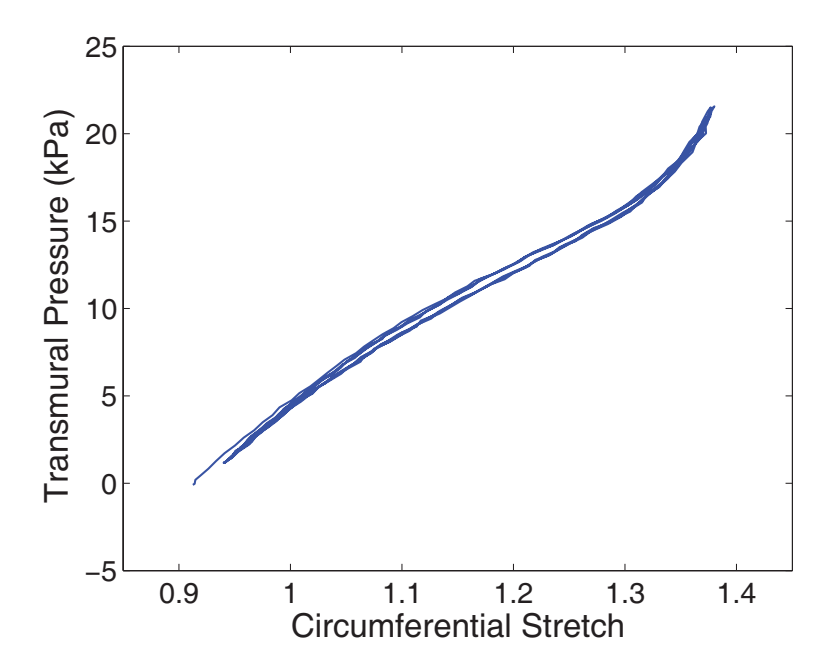


Fig. 5.5: A representative example of the five repeated loading and unloading curves of the anterior region of the thoracic aorta.

unloading curves exhibited a small hysteresis (i.e., pseudo-elastic behavior) like other vascular tissues (Fig. 5.5). Therefore, the last loading curve was used for stress-strain analysis in this study.

The circumferential stretch (Fig. 5.6) and the longitudinal stretch (Fig. 5.7) were distributed nonuniformly within the domain and they varied according to the circumferential region. As the pressure increased, the circumferential stretch was increased gradually, but the longitudinal stretch was relatively uniform compared to the circumferential stretch.

Likewise, the stress also changed with respect to the change of pressure and varied with the circumferential region. The averaged stretch and stress within the domain for each region were calculated for comparison among the four circumferential regions of the aorta. Fig. 5.8 displays the circumferential and longitudinal stress-stretch curves for the four regions. All aorta samples exhibited similar nonlinear stress-stretch behavior. The stress-stretch curves deviated from each other progressively as the pressure increased. The extent of deviation for the circumferential stress-stretch curve was more than that of the longitudinal one, and

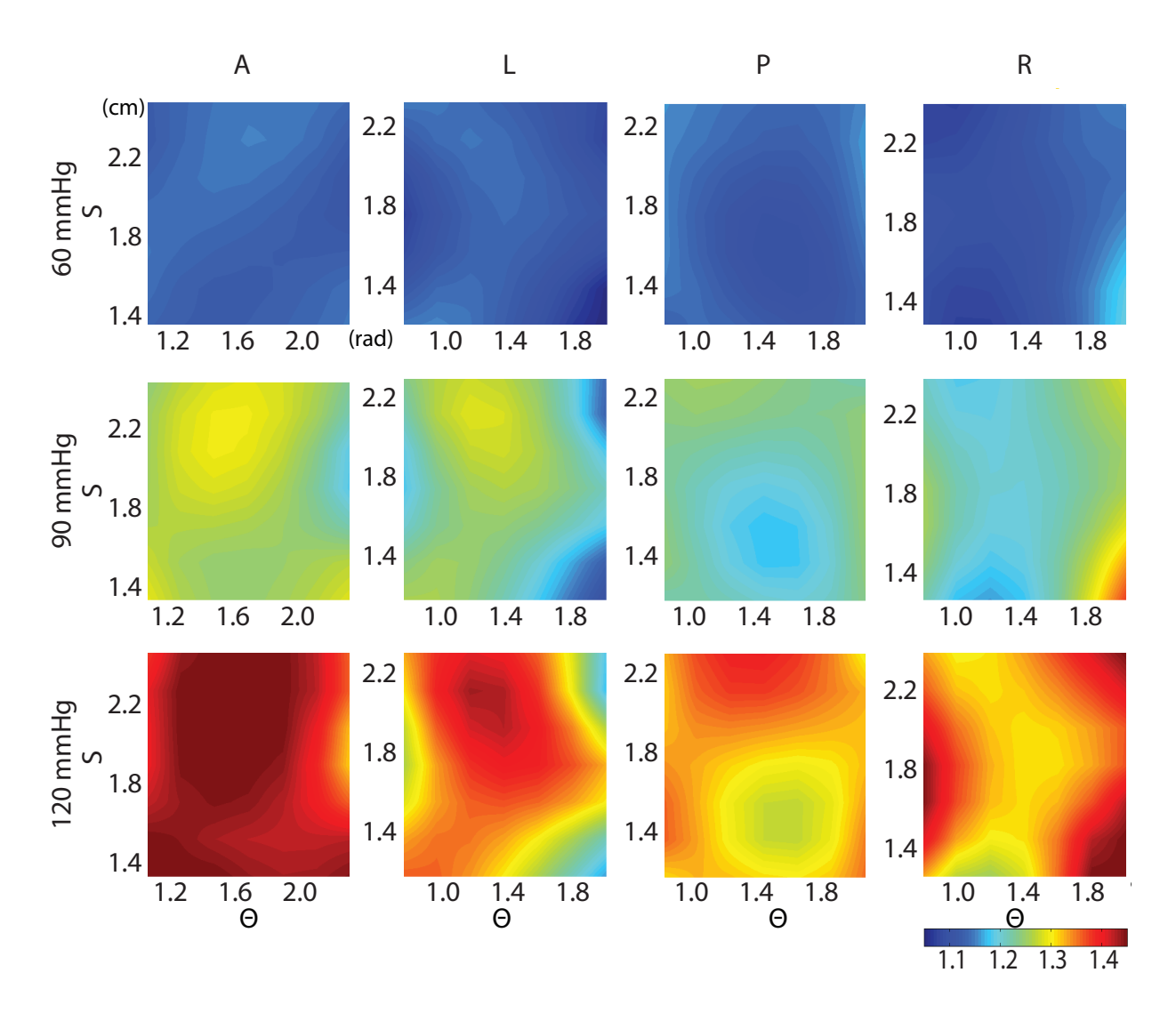


Fig. 5.6: A representative example of the distributions of circumferential stretch for the four circumferential regions of one thoracic aorta sample at transmural pressures of 8.00 kPa, 12.00 kPa, and 16.00 kPa, respectively, and a longitudinal stretch ratio ( $\Lambda_Z$ ) of 1.35.

the overall change of the circumferential stress was larger than the longitudinal stress. In the low pressure range, the stress-stretch response for each region was nearly linear, but it became nonlinear after the transmural pressure exceeded a transition point, which ranged from 10.93 to 14.53 kPa (82 - 109 mm Hg).

The circumferential stiffness of the four circumferential regions is plotted with respect to the increase of pressure in Fig. 5.9. In the low pressure range, the stiffness was nearly constant, which corresponded to the linear stress-stretch response, but increased markedly after the transition point.

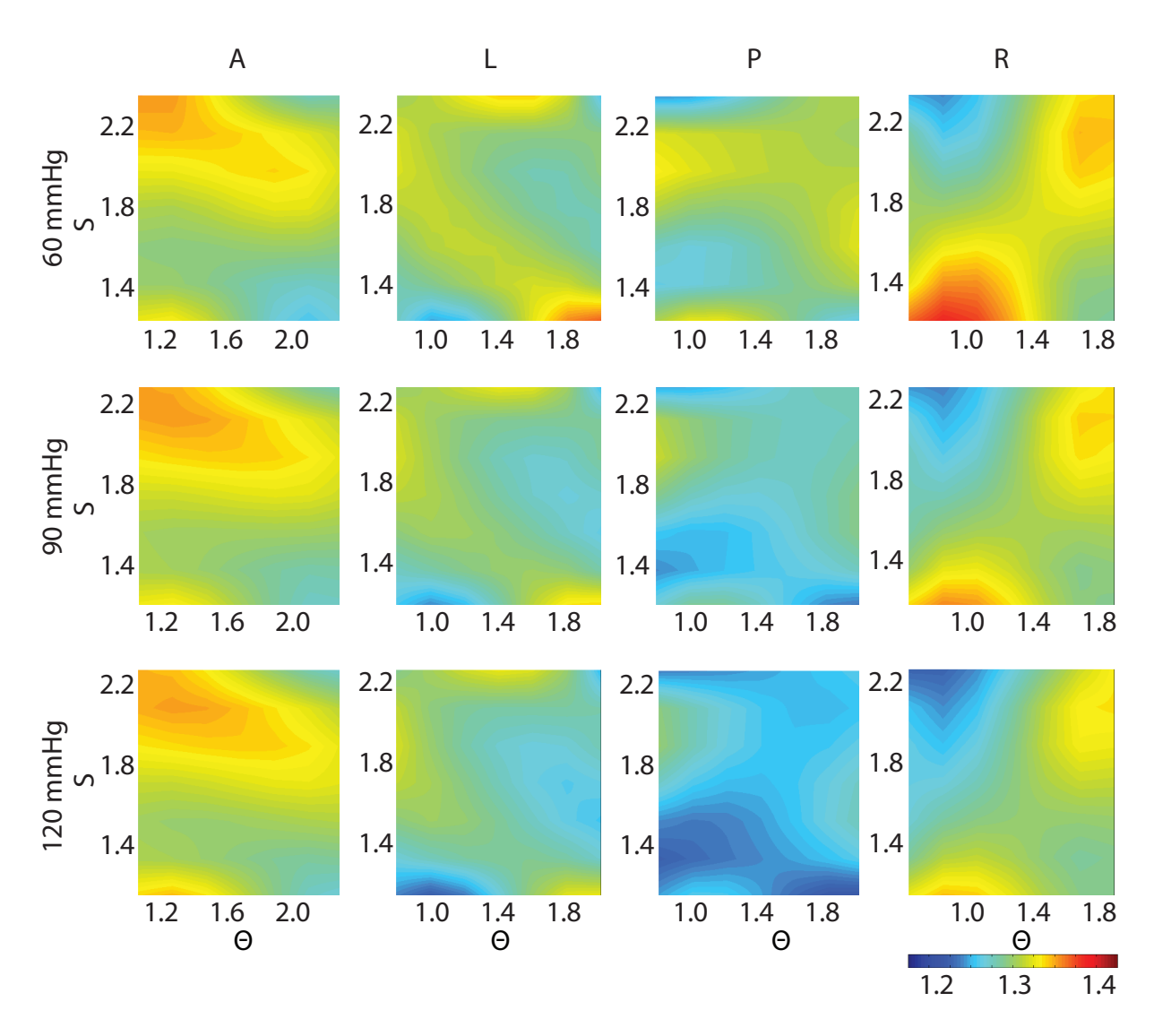


Fig. 5.7: A representative example of the distributions of longitudinal stretch for the four circumferential regions of one thoracic aorta sample at transmural pressures of 8.00 kPa, 12.00 kPa, and 16.00 kPa, respectively, and a longitudinal stretch ratio ( $\Lambda_Z$ ) of 1.35.

The mean of the circumferential stretch, which was averaged within the domain, was computed for each region of all aorta samples. There was no significant difference in the mean stretch among the four circumferential regions at the transmural pressure of 12.00 kPa (90 mm Hg) (Fig. 5.10). The mean and standard deviation of the stretch at the transmural pressure of 12.00 kPa and at longitudinal stretch of 1.35 were  $1.20 \pm 0.06$  (A),  $1.22 \pm 0.03$  (L),  $1.22 \pm 0.05$  (P), and  $1.21 \pm 0.04$  (R). The mean and standard deviations of the stretch at different pressure and different longitudinal stretch are tabulated in Appendix C.

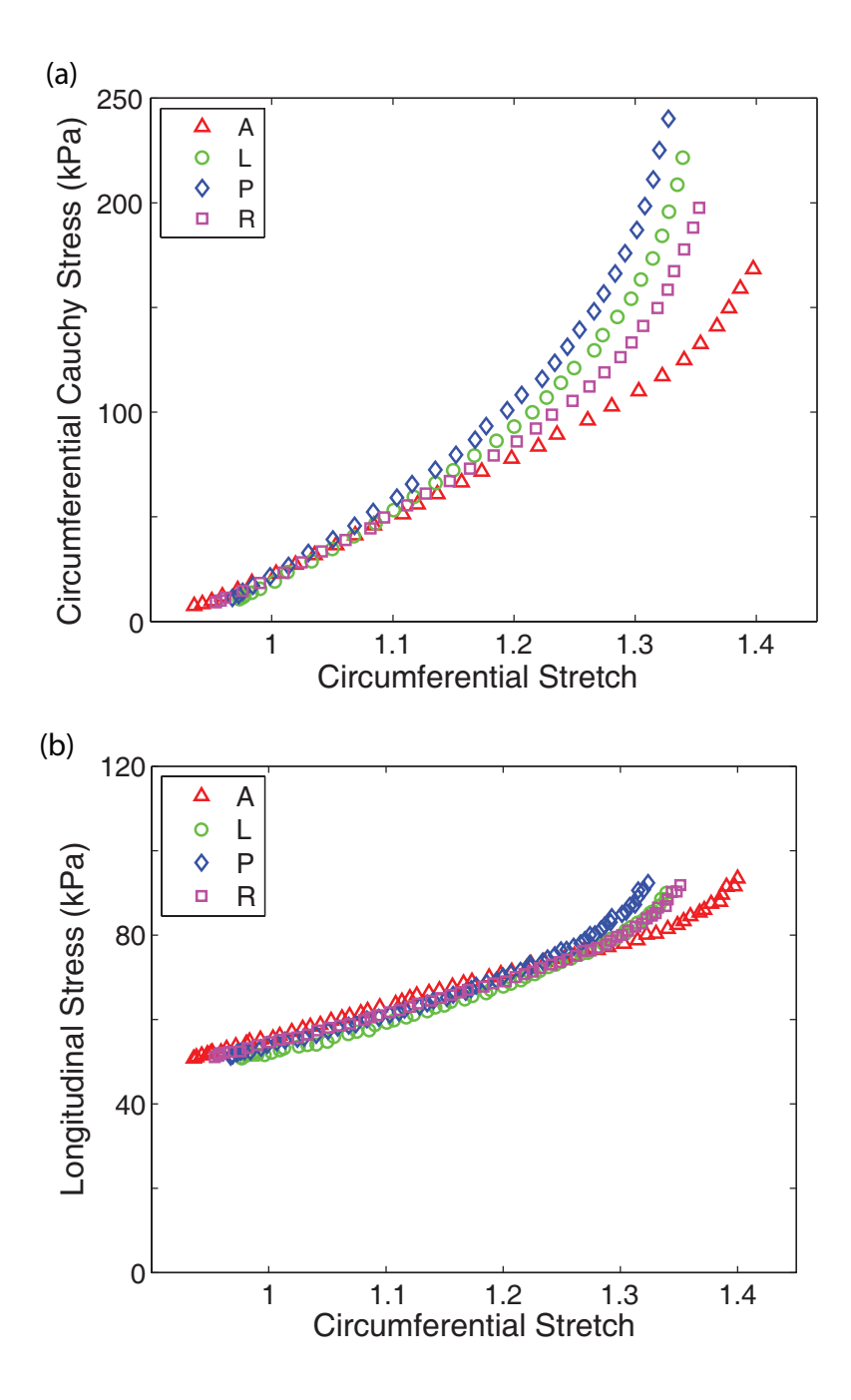


Fig. 5.8: A representative example of the circumferential Cauchy stress and circumferential stretch curve (a) and the longitudinal stress and circumferential stretch curve (b) at a longitudinal stretch ratio ( $\Lambda_Z$ ) of 1.35.

In the same manner, the mean of circumferential stress averaged within the domain was computed for each region, and a significant difference was found among the four circumferential region. For the proximal portion of the thoracic aorta, in the post-hoc analysis, there

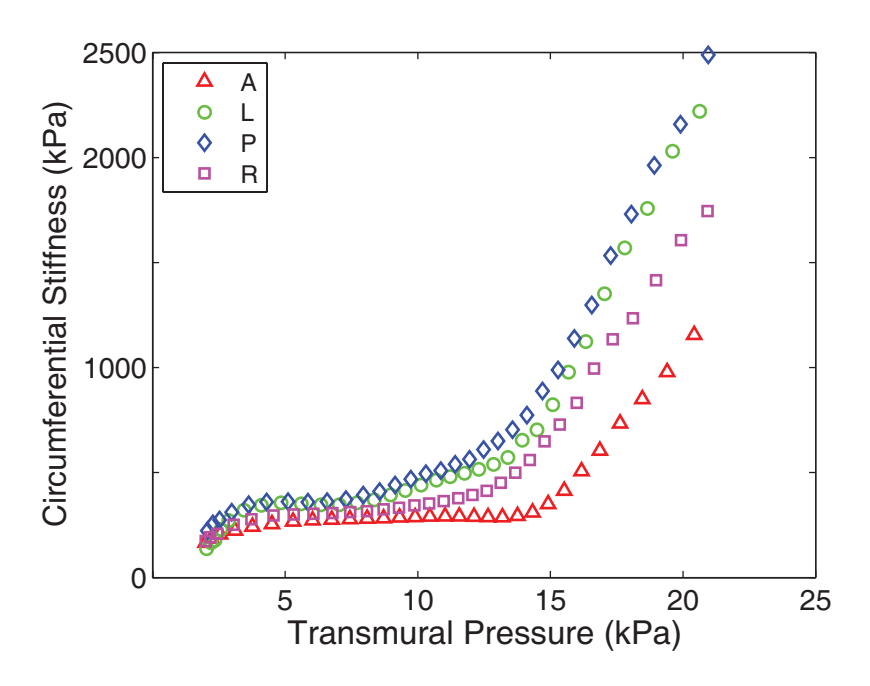


Fig. 5.9: A representative example of the circumferential stiffness and transmural pressure curve at a longitudinal stretch ratio ( $\Lambda_Z$ ) of 1.35.

was a significant difference between the anterior and posterior regions, the anterior and left lateral regions, the anterior and right lateral regions, the left lateral and posterior regions, and the posterior and right lateral regions at the transmural pressures above 8.00 kPa (60 mm Hg). For the distal portion of the thoracic aorta, a significant difference was also found between the anterior and posterior regions. The mean and standard deviations of the stress at different pressure and different longitudinal stretch are tabulated in Appendix C.

## 5.6 Circumferential variation in the stiffness

The circumferential stiffness in this study is defined as a change in stress with respect to a change in stretch in the circumferential direction. Hence, it presents the intrinsic stiffness of the vascular tissue. There was a significant difference in the stiffness among the four circumferential regions. The mean stiffness of the posterior region had the highest value, and the anterior region had the lowest. The difference in the stiffness among the four regions became more prominent as pressure increased. Fig. 5.12 shows the mean stiffness

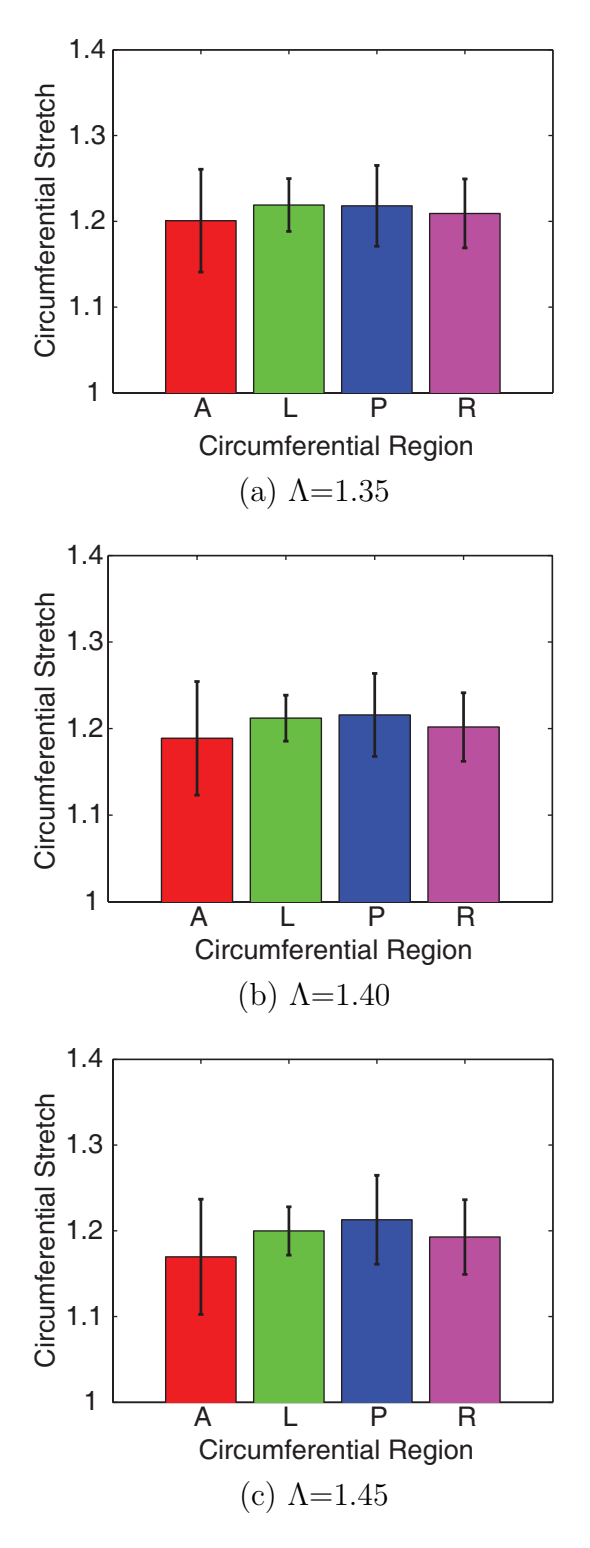


Fig. 5.10: Comparison of the mean circumferential stretch of the proximal thoracic aorta at the transmural pressure of 12.00 kPa for each longitudinal stretch ratio  $(\Lambda_Z)$ .

and the statistical evaluation of their significance at the transmural pressure of 12.00 kPa, which is within the transition region for the thoracic aorta at each fixed longitudinal stretch ratio. The stiffness at the anterior region differed significantly from the posterior. However, the mean pressure-strain elastic modulus, which represents the structural stiffness, had no significant difference among the four regions (Fig. 5.13). The mean and standard deviation of the circumferential stiffness for each region at the investigated transmural pressure of 8.00, 12.00, and 16.00 kPa are listed in Table C.5 in Appendix C.

# 5.7 Longitudinal variation in the mechanical behavior of the aorta

The aorta at all tested regions exhibited typical nonlinear pseudoelastic behavior. For the mean circumferential stretch of the distal thoracic aorta, there was no significant difference between the anterior and posterior regions, which is the same trend as the proximal thoracic aorta (Fig. 5.14). The values of mean stretch of the anterior and posterior regions of the distal thoracic aorta had a higher standard deviation than that of the proximal. The stretch of the anterior region in the distal portion was slightly higher than the proximal, although the difference was not statistically significant. The stretch of the posterior region had almost the same amount of the stretch in both proximal and distal portions.

The mean stress of the distal thoracic aorta was higher in the both anterior and posterior regions compared to that of the proximal portion at the same transmural pressure 12.00 kPa (Fig. 5.15). Similar to the proximal portion, the mean stress of the posterior region at the distal portion was significantly higher than that of the anterior region. The specific values of the stretch and stress are included in Appendix C.

The mean circumferential stiffness was also changed with the change in pressure (Fig. 5.16). The difference in the mean stiffness of the posterior region from the proximal to the distal portions of the thoracic agree was significantly higher than that of the anterior

region, and their difference became larger as pressure increased. The posterior region remains significantly stiffer than the anterior regions for both longitudinal portions. However, the pressure-strain elastic modulus did not show the significant difference between the proximal and distal portions for both anterior and posterior regions, although the mean pressure-strain elastic modulus was higher at the distal portion (Fig. 5.17). It may be due to the large standard deviation. The specific values of the circumferential stiffness and pressure-strain elastic modulus are included in Appendix C.

## 5.8 Material parameters

Material parameters are one of common indicators to describe the mechanical response of the vascular tissue using a constitutive model. Parameter estimation was performed to determine the material parameters of the aorta for each region. A representative best-fit curve of the theoretical prediction to the experimentally measured data is shown in Fig. 5.18. For most of the test samples, the regression curves fit better to the circumferential stress-stretch curve than the longitudinal curve.

The mean and standard deviation of all parameters are shown in Table 5.1. Parameter  $c_1$  presents the isotropic behavior of the elastin of the aorta. The  $c_2$  is a parameter of the exponential part of the constraint mixture model, which represents the mechanical behavior of the four collagen fiber families (See Chapter 4.4.1). The anterior region of the thoracic aorta has the biggest mean value of  $c_1$  in the proximal portion, but there was no significant difference among the four circumferential regions (Fig. 5.19). On the other hand, the parameter  $c_2$  in the anterior region has the smallest mean value among the four circumferential regions (Fig. 5.19), and a significant difference was found between the anterior and right lateral regions. For the statistical analysis of  $c_1$  and  $c_2$ , data from all 11 aortic sample were used regardless of the longitudinal portion. In a statistical analysis, there were significant differences of  $c_1$  and  $c_2$  between the anterior and posterior regions (Fig. 5.19 and 5.20).

Table 5.1: The mean and standard deviation of material parameters for all aorta samples

Parameter \ Region	Anterior	Posterior
$c_1 \text{ (kPa)}$	$406 \pm 96$	$318 \pm 93$
$c_2 \text{ (kPa)}$	$155 \pm 63$	$318 \pm 209$
$c_3$	$2.73 \pm 2.87$	$6.33 \pm 7.91$
$c_4$ (Pa)	$(31.2 \pm 83.7) \times 10^{-9}$	$(1.48 \pm 4.54) \times 10^{-6}$
$c_5$	$(1.93 \pm 4.74) \times 10^{-6}$	$(7.7 \pm 17.1) \times 10^{-3}$
$G_1^e$	$1.12 \pm 0.06$	$1.23 \pm 0.07$
$G_2^{ar{e}}$	$1.19 \pm 0.04$	$1.15 \pm 0.06$
$G_h^{\bar{c}}$	$1.09 \pm 0.01$	$1.09 \pm 0.01$
$G_h^m$	$1.10 \pm 0.00$	$1.10 \pm 0.00$
$\alpha(\circ)$	$26.5 \pm 6.4$	$31.9 \pm 12.1$

(a) The anterior and posterior regions

Parameter \ Region	Left lateral	Right lateral
$c_1 \text{ (kPa)}$	$355 \pm 90$	$345 \pm 76$
$c_2 \text{ (kPa)}$	$226 \pm 104$	$197 \pm 76$
$c_3$	$4.10 \pm 3.47$	$5.83 \pm 5.57$
$c_4$ (Pa)	$0.685 \pm 0.108 \times 10^{-9}$	$(23.6 \pm 37.1) \times 10^{-9}$
$c_5$	$0.202 \pm 0.522$	$2.28 \pm 5.36$
$G_1^e$	$1.19 \pm 0.10$	$1.20 \pm 0.07$
$G_2^{ar{e}}$	$1.14 \pm 0.06$	$1.17 \pm 0.04$
$G_h^{ar{c}}$	$1.09 \pm 0.01$	$1.09 \pm 0.01$
$G_h^{ ilde{c}} \ G_h^m$	$1.10 \pm 0.00$	$1.10 \pm 0.00$
$\alpha(\circ)$	$24.5 \pm 11.7$	$30.0 \pm 4.7$

<sup>(</sup>b) The left and right lateral regions

While the material parameters in the unit of stress corresponding to the behavior of the elastin  $(c_1)$  and collagen  $(c_2)$  have large values, the parameters for smooth muscle  $(c_4)$  very small. All homeostatic stretch parameters,  $G_1^e$ ,  $G_2^e$ ,  $G_h^c$ , and  $G_h^m$  are less than 1.2 for each constituent. The averaged angle of collagen fiber family for each region is about 28°.

#### 5.9 DISCUSSION

#### 5.9.1 Nonlinear, anisotropic behavior of the aorta

The stress-stretch curves for all local regions of the thoracic aorta in this study exhibited nonlinear behavior similar to other studies (Groenink et al., 1999; Stergiopulos et al., 2001; Sokolis, 2007). The circumferential stress increased linearly up to a transition point beyond which the stress changed rapidly with the increase of the stretch. This nonlinear trend of the circumferential stress with respect to the stretch (or strain) is consistent with other works for the human thoracic aorta (Spina et al., 1983), the canine thoracic aorta (Zhou and Fung, 1997), and ovine thoracic aorta (Wells et al., 1999). The range of linear circumferential stress-stretch response in this study is at a relatively higher pressure than other porcine arteries such as porcine basilar arteries and coronary arteries (Hu et al., 2007; Pandit et al., 2005; Wang et al., 2006).

The transition from linear to nonlinear behavior of the aorta occurred at 10.93 to 14.53 kPa (82 - 109 mm Hg), which falls within the *in vivo* pressure range from 10.13 to 15.20 kPa (76 - 114 mm Hg) when the radial compression of the aorta by the surrounding tissue is assumed to be around 5% of internal pressure (Zhang et al., 2005). Other studies (Danpinid et al., 2010; Shadwick, 1999) have also suggested that the transition corresponded to normal physiological conditions.

The circumferential stress-strain relationship differs from the longitudinal stress-strain relationship. It infers that the mechanical properties of the aorta is anisotropic, which is a well-known property of the soft tissue reported in many other studies (Fung, 1993; Humphrey,

#### 5.9.2 Variation in stiffness

This study supports that the mechanical properties of the aorta depend on location. One major finding in this study is the circumferential variation in the stiffness of the healthy thoracic aorta. The posterior region of the aorta was significantly stiffer than the anterior. It may be related to the bigger motion of the anterior region than the posterior (Goergen et al., 2007). However, the posterior region was significantly thinner than the anterior, so that the structural stiffness, which is represented by the pressure-strain elastic modulus, remained non-significant. This finding suggests that the circumferential distention of the proximal thoracic aorta may be uniform in vivo even with the significant variations in stiffness of the aortic tissue in the circumferential direction. However, the validation of this suggestion requires a better understanding of the effect of the surrounding tissues and the spine on biomechanics of the aortic wall in vivo.

This study also reveals the longitudinal variation in stiffness of the healthy thoracic aorta. The stiffness in the distal portion is higher than the proximal portion for the both anterior and posterior regions. This trend is consistent with previous studies (Purslow, 1983; Zou and Zhang, 2009).

#### 5.9.3 Heterogeneous composite of the aorta

The arterial wall is a heterogeneous composite consisting mainly of collagen, elastin, and smooth muscle cells. The amount of these contents varies with locations along the arterial tree (Fischer and Llaurado, 1966; Halloran et al., 1995; Purslow, 1983) and are responsible for the mechanical properties of a blood vessel (Lillie and Gosline, 2007; Roach and Song, 1994; Stergiopulos et al., 2001). Many studies have reported that elastin fibers are primarily responsible for the linear behavior of an artery in the low pressure range (Gundiah et al., 2007; Shadwick, 1999; Stergiopulos et al., 2001). The influence of elastin on the mechanical

properties of aortic tissue has been investigated (Gundiah et al., 2007; Lillie and Gosline, 2007; Zou and Zhang, 2009). These previous studies imply that the stiffness of the aortic wall may be affected by the amount of elastin, the orientation of elastin fibers, and the density of cross-linking. On the other hand, collagen is recruited in the higher pressure range and contributes to the nonlinear behavior of arterial tissue (Groenink et al., 1999; Shadwick, 1999). The orientation of collagen fibers and the amount of cross-linking influence the mechanical response of vascular tissue (Haskett et al., 2010; Holzapfel et al., 2002). Many previous studies suggest that the microstructure and relative content of each component may cause the variation in stiffness among the different circumferential regions shown in the this study.

# 5.9.4 Relation of heterogeneous mechanical properties with pathological conditions

The mechanical properties of a diseased aorta vary spatially with its pathological condition. Previous studies (Iliopoulos et al., 2009a; Raghavan et al., 2006; Thubrikar et al., 2001) suggested nonuniform changes of the aortic wall during the development of aortic diseases, such as aortic aneurysms. Iliopoulos et al. (2009b) reported a preferential bulging in the anterior side of the human ascending thoracic aneurysms. Choudhury et al. (2009) showed that the elastic modulus of the ascending thoracic aorta depended on the circumferential region as well as the pathological tissue type.

On the other hand, the variation in mechanical properties of the aorta may have an affection on vascular remodeling and the pathological condition. For example, the progression of abdominal aortic aneurysms is associated with an increase in circumferential stiffness (Vande Geest et al., 2006).

Therefore, the mechanical properties of vascular tissue may affect the pathological condition or vice versus. Previous studies were, however, not enough to make a decisive conclusion about the relations of heterogeneous biomechanical properties with the development of aortic diseases. It promotes further comparative studies of local mechanical properties of aortic walls between healthy and diseased samples.

#### 5.9.5 Material parameters

The mechanical behavior of a blood vessel has been characterized with a constitutive model based on a constrained mixture approach using experimental data. Previous studies have used many different constitutive models and different measures of strain. Recently, many adopted constitutive models motivated from arterial structure (Holzapfel et al., 2000; Zulliger et al., 2004b). One of the structurally motivated models to describe arterial mechanics is the constitutive model based on a constrained mixture theory. This model suggests that the mechanical behavior of a blood vessel can be explained by major constituents, that is, elastin, collagen fibers, and smooth muscles. Parameters for elastin  $(c_1)$  and collagen  $(c_2)$  that we found in this study have larger values compared to those for smooth muscles as shown in Table 5.1. These results suggest that the elastin and collagen fibers are major components contributing to the mechanical response of the aorta.

In our study, the mean values of  $c_1$  and  $c_2$  for the distal thoracic aorta are smaller than the proximal, respectively. It is in a good agreement with the previous study of Halloran et al. (1995), which showed that the content of collagen and elastin, respectively, decreases from proximal to distal portion of the aorta.

For each circumferential region, the mean value of  $c_1$  is higher at the proximal portion than the distal and  $c_2$  is higher in the distal portion than the proximal. It implies that the elastin is more dominant in the proximal portion and the collagen is in the distal. Indeed, the content of elastin is higher in the proximal portion than the distal, and that of collagen is higher in the distal (Davidson et al., 1986).

In the comparison of the material parameters between the anterior and posterior regions,  $c_1$  of the anterior is higher than that of the posterior for both proximal and distal portions of the thoracic aorta, although there was no significant difference in the proximal portion. It

may be because of the different number of elastin lamella between two circumferential regions. O'Connell et al. (2008) examined the number of medial lamellae for the rat abdominal aorta, and a significant difference was found in the anterior and posterior regions.

The smooth muscle contraction affects the stress and strain distribution in arteries (Rachev and Hayashi, 1999; Zulliger et al., 2004a), and the elastin lamina is much stiffer than the smooth muscle layer (Matsumoto et al., 2004). In this study, the active tone was not accounted for and the parameters of smooth muscle,  $c_4$  and  $c_5$ , were found to be very small. Therefore, the role of smooth muscle in the passive mechanical behavior of the thoracic aorta was insignificant.

Most of previous studies have assumed that the elastin has isotropic properties. However, Rezakhaniha et al. (2011) reported recently that the anisotropic properties of elastin provide better curve fit to characterize the mechanical response of a blood vessel. Hence, there is a need to study the mechanical properties and behavior of elastin.

### 5.9.6 Limitation of this study

Although our validation study showed that the errors were negligible, there might be measurement errors caused by the rotation of the specimen when measuring the strain at four local circumferential regions of the thoracic aorta. The accuracy of the strain measurement may be enhanced by using multiple cameras simultaneously around the specimen or using a concave conical mirror (Genovese, 2009).

We found that the values of stress and strain at the distal portion have larger variances compared to those at the proximal portion, which might attribute to the small number of specimen from the distal portion. The number of samples also affect the statistical analysis on significance test. Therefore, we suggest that more experimental test with specimens from the distal portion can strengthen the statistical analysis presented in this study.

Another shortcoming of this study is that the histology of the aortic wall was not fully examined to validate the prediction based on the mixture theory-based constitutive model for the spatial variation in the mechanical properties of the thoracic aorta. The histological and microstructural features, such as the number of elastin lamellae, may correlate to the circumferential variation, and further investigation will be needed to understand the heterogeneity of the thoracic aorta in this study.

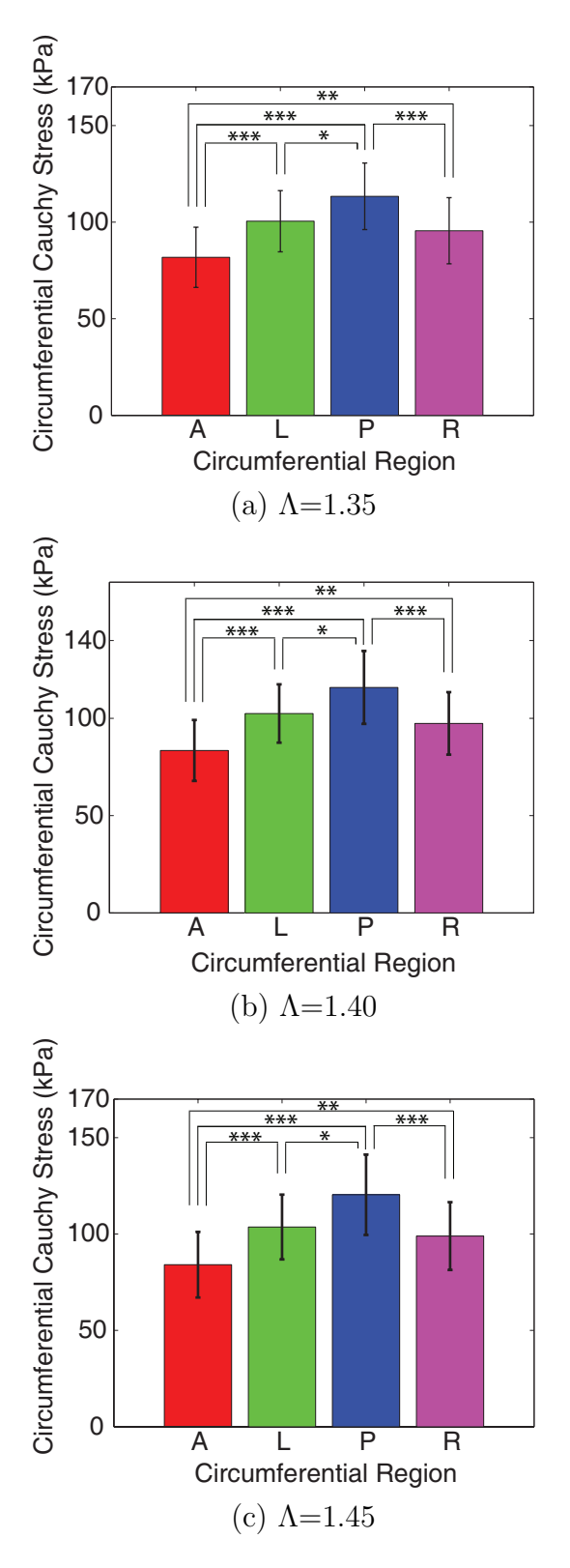


Fig. 5.11: Comparison of the mean circumferential Cauchy stress of the proximal thoracic aorta aat the transmural pressure of 12.00 kPa for each longitudinal stretch ratio ( $\Lambda_Z$ ). Asterisk represents the significant difference (\*: p<0.05, \*\*: p<0.01, \*\*\*: p<0.005)

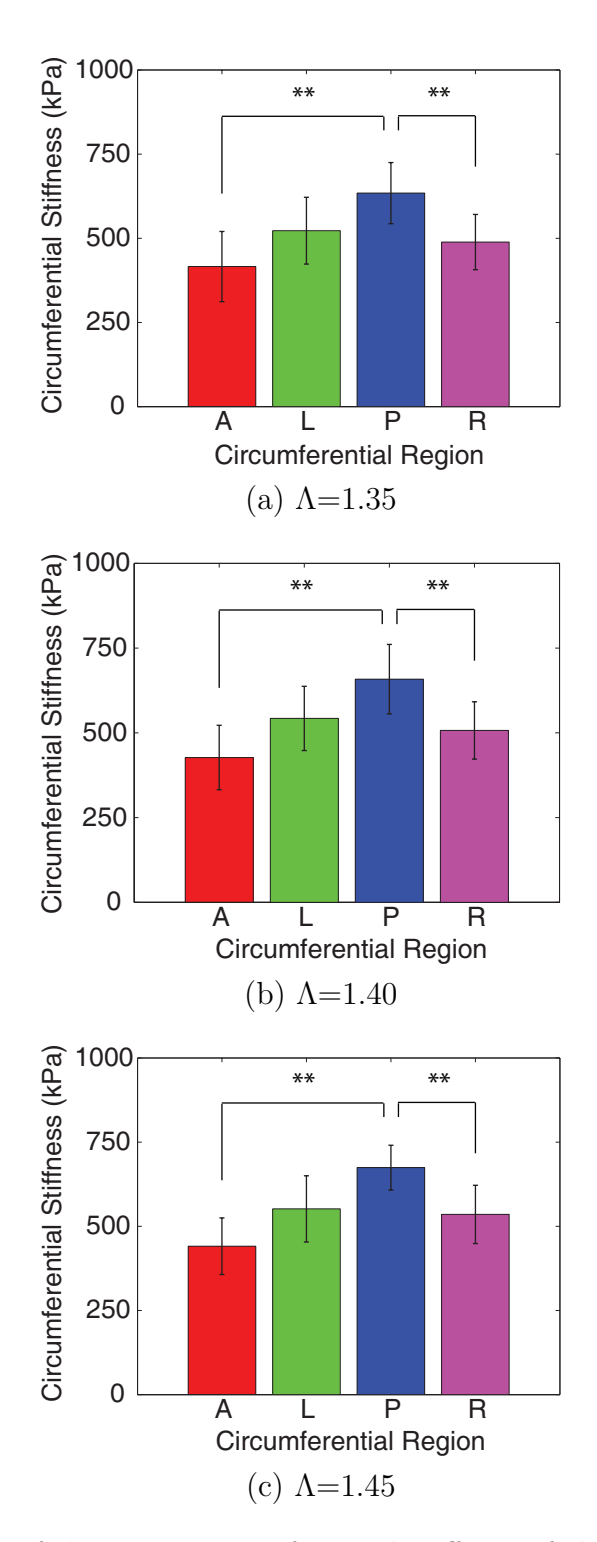


Fig. 5.12: Comparison of the mean circumferential stiffness of the proximal thoracic aorta among the four circumferential regions at the transmural pressure of 12.00 kPa for each longitudinal stretch ratio ( $\Lambda_Z$ ).

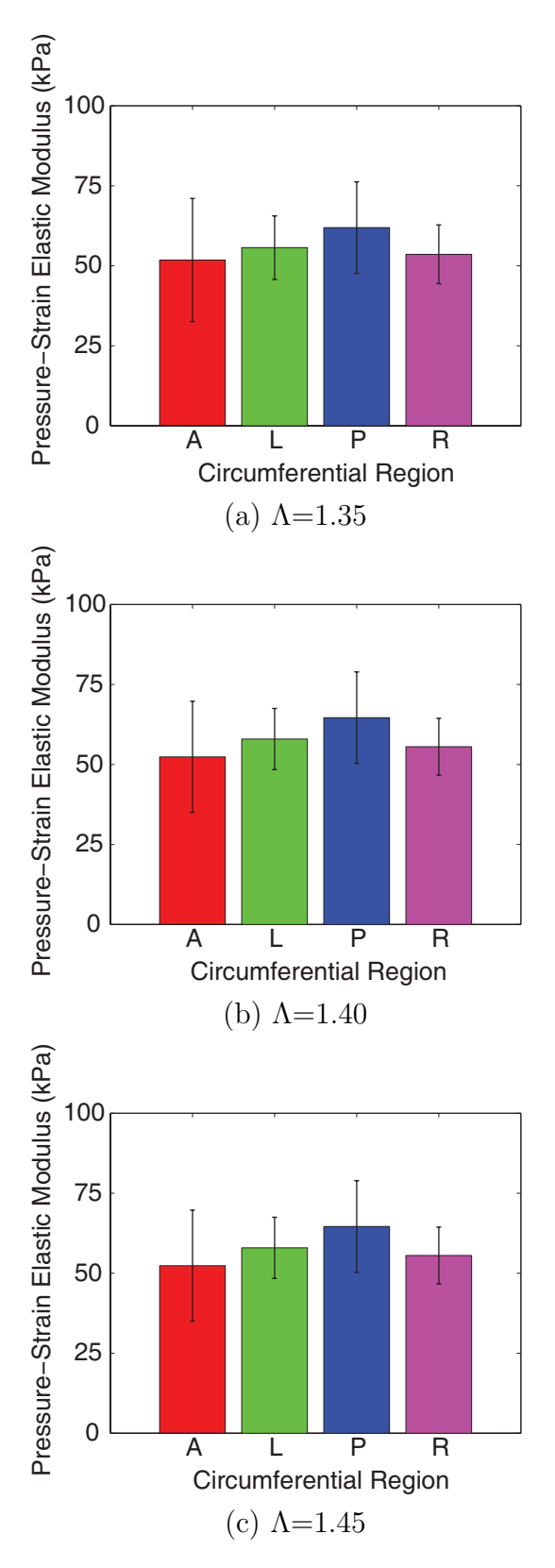


Fig. 5.13: Comparison of the mean pressure-strain elastic modulus of the proximal thoracic aorta at the transmural pressure of 12.00 kPa for each longitudinal stretch ratio  $(\Lambda_Z)$ .

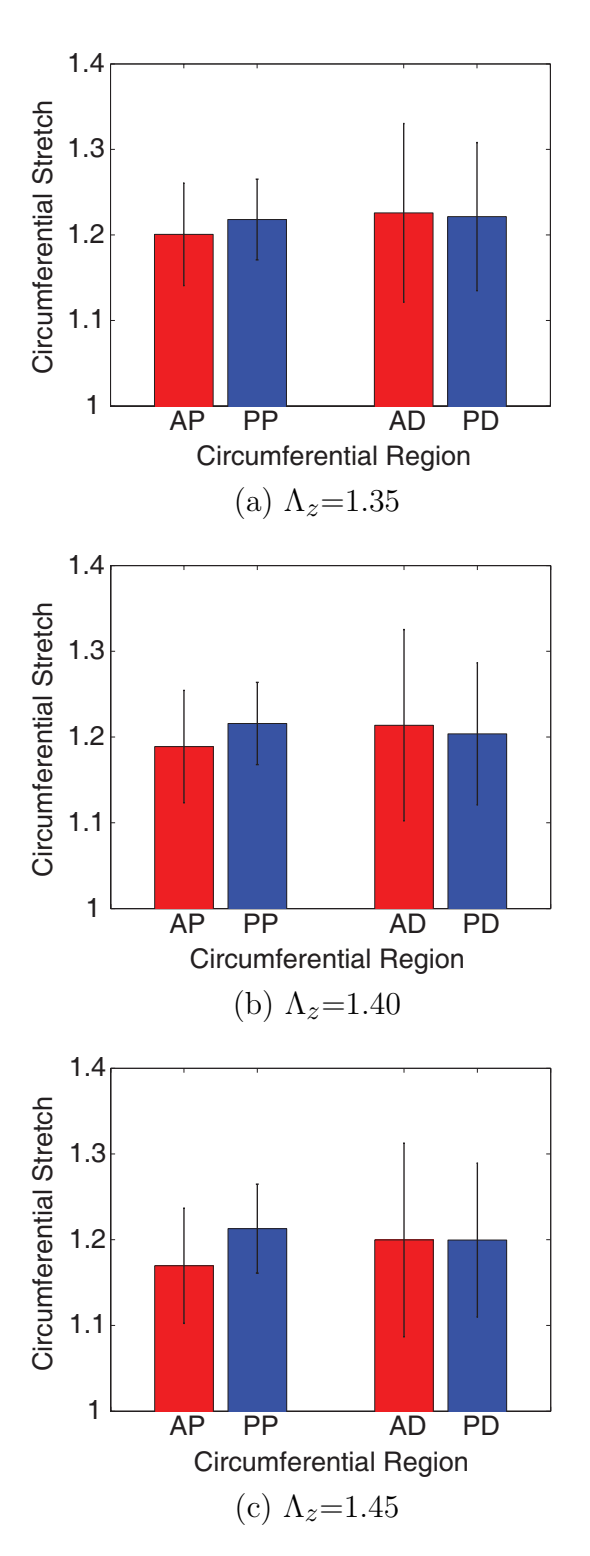


Fig. 5.14: Comparison of the mean stretch at the anterior and posterior regions of the proximal and distal portions of the thoracic aorta at the transmural pressure of 12.00 kPa for each longitudinal stretch ratio ( $\Lambda_Z$ ).

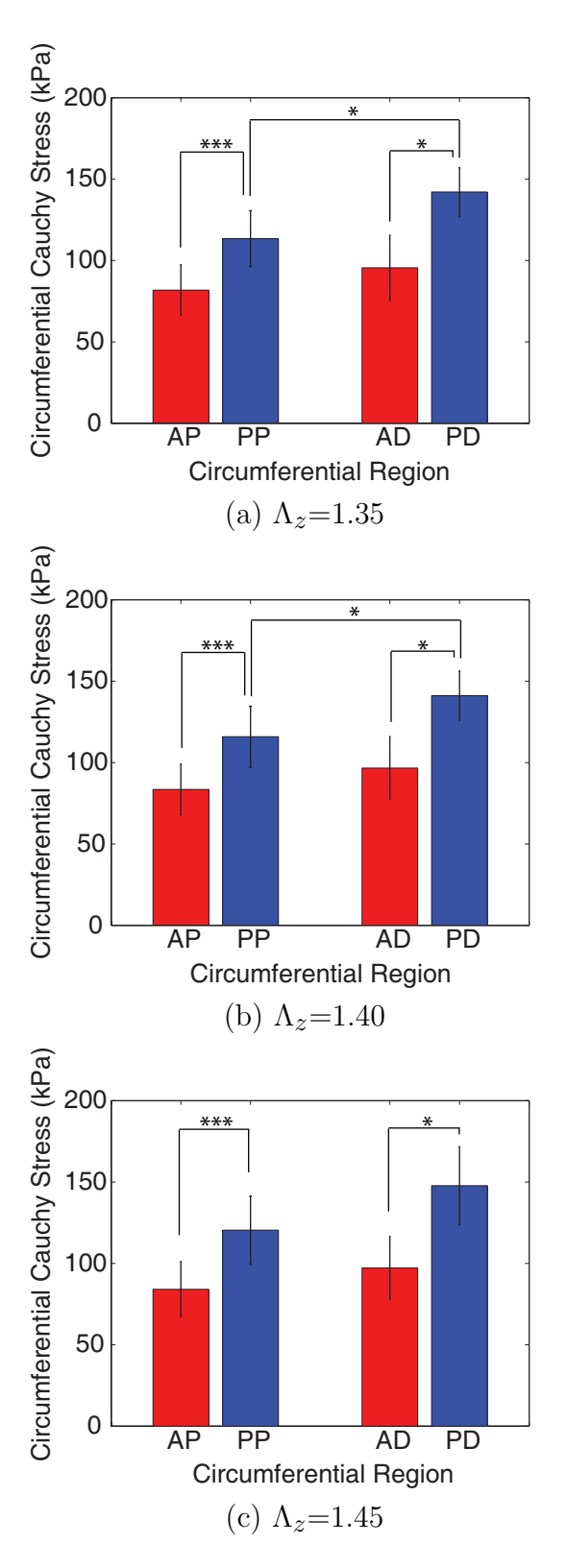


Fig. 5.15: Comparison of the mean circumferential stress at the anterior and posterior regions of the proximal and distal portions of the thoracic aorta at the transmural pressure of 12.00 kPa for each longitudinal stretch ratio  $(\Lambda_Z)$ .

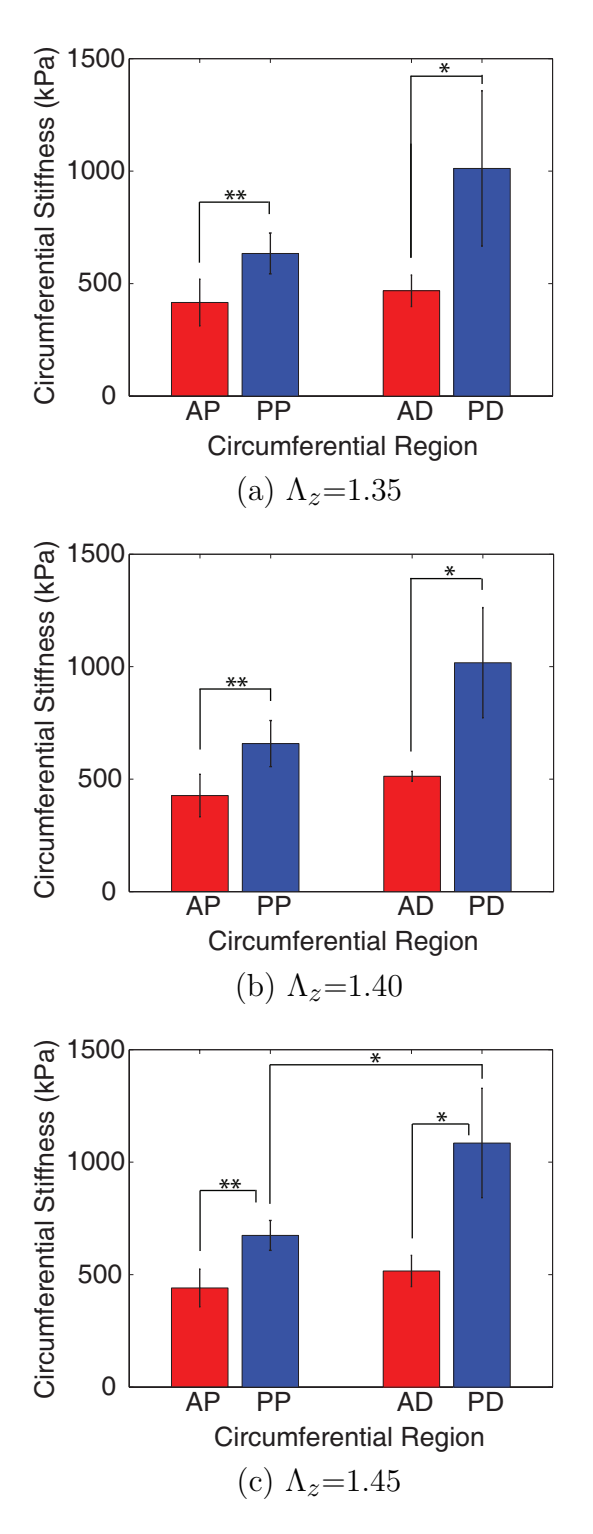


Fig. 5.16: Comparison of the mean circumferential stiffness at the anterior and posterior regions of the proximal and distal portions of the thoracic aorta at the transmural pressure of 12.00 kPa for each longitudinal stretch ratio ( $\Lambda_Z$ ).

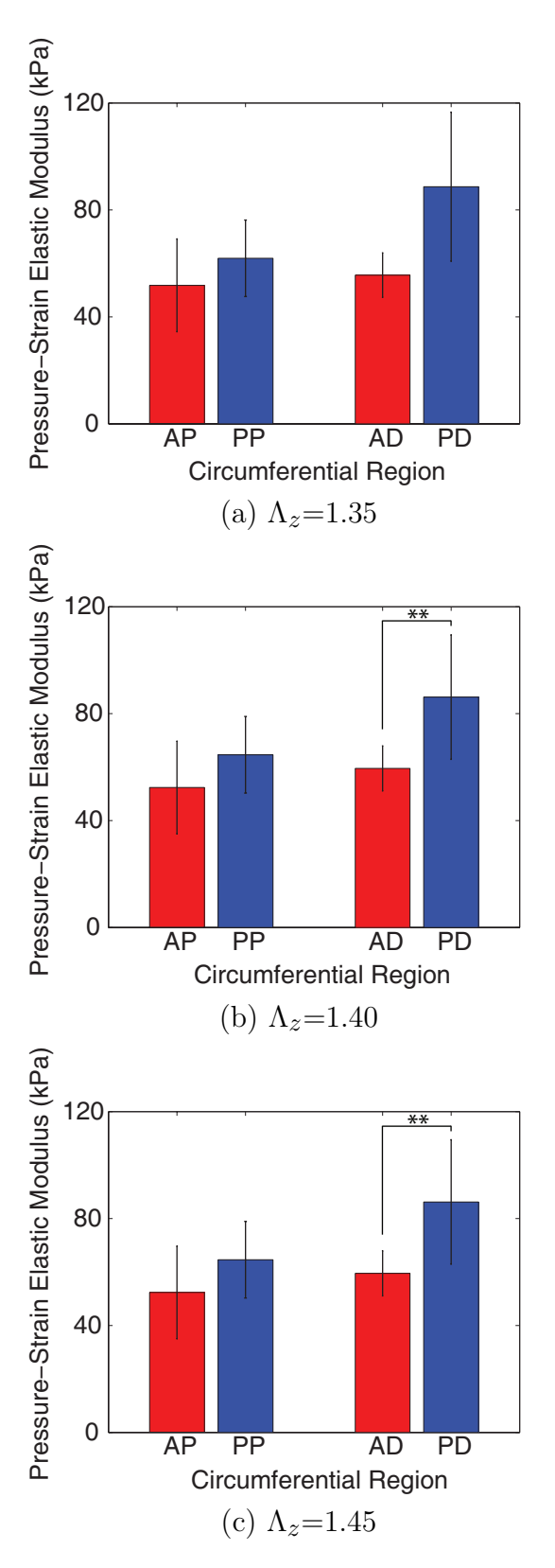
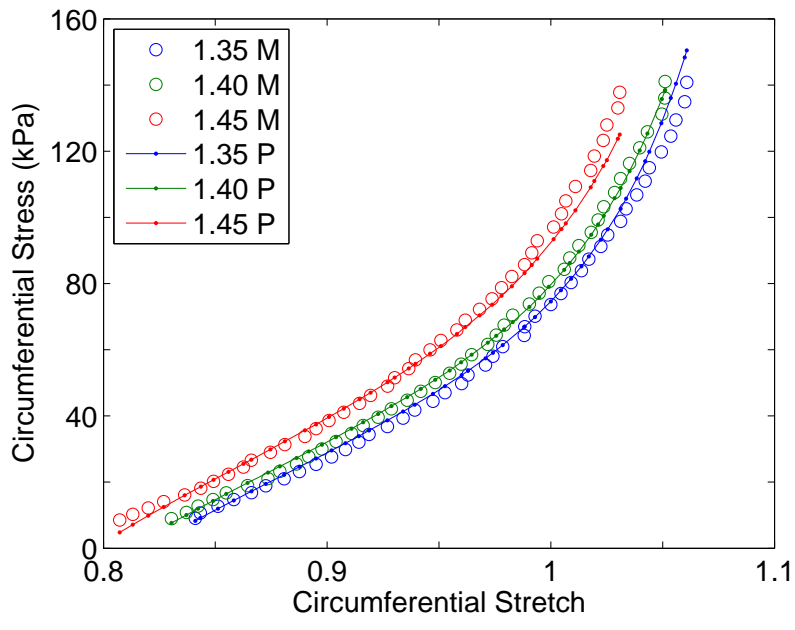
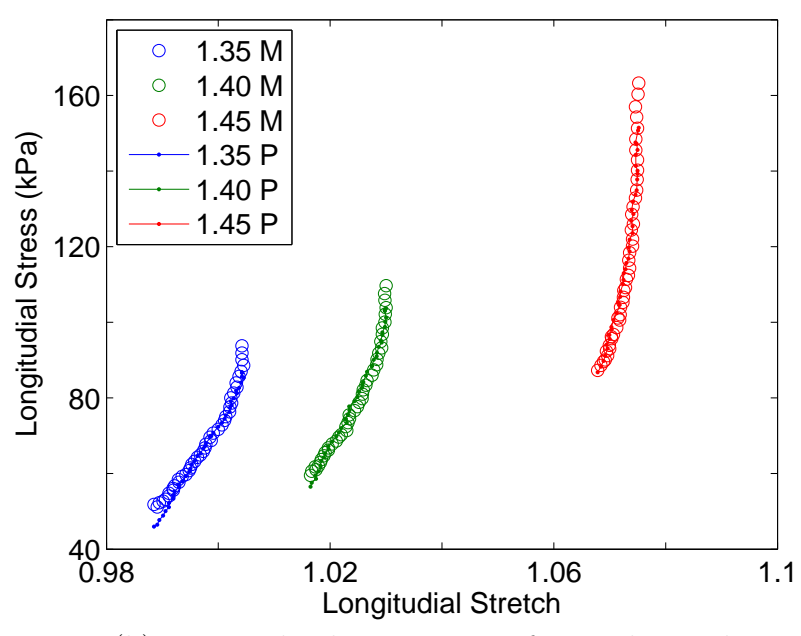


Fig. 5.17: Comparison of the mean pressure-strain elastic modulus at the anterior and posterior regions of the proximal and distal portions of the thoracic aorta at the transmural pressure of 12.00 kPa for each longitudinal stretch ratio ( $\Lambda_Z$ ).



(a) Circumferential stress-circumferential stretch



(b) Longitudinal stress-circumferential stretch

Fig. 5.18: A representative stress-stretch plot. Stress was calculated by using experimentally measured data and theoretically predicted. M: experimentally measured data, P: theoretically predicted data

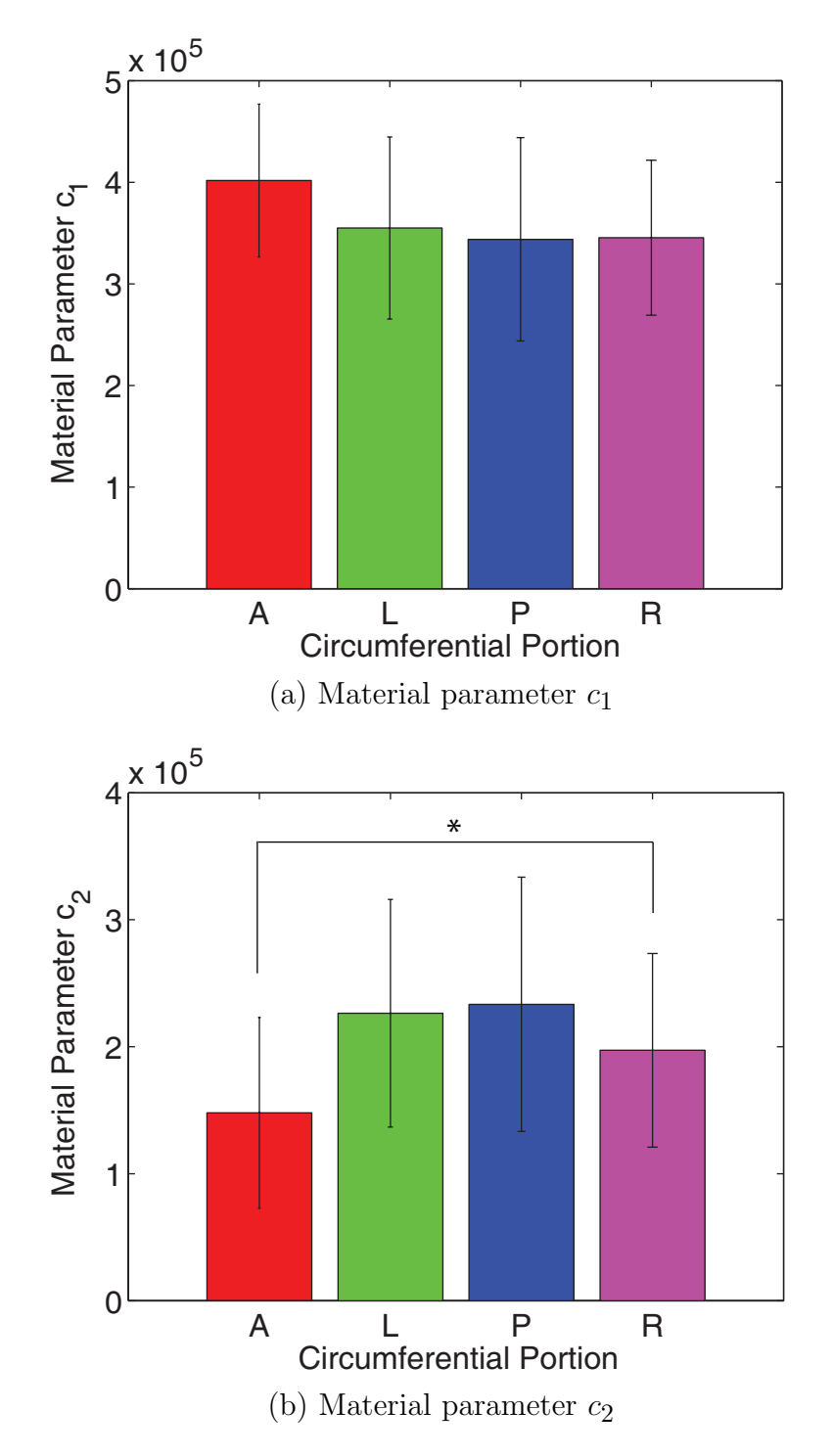


Fig. 5.19: Comparison of the mean and standard deviation of material parameter  $c_1$  (a) and  $c_2$  (b) among the four circumferential regions for the proximal thoracic aorta.

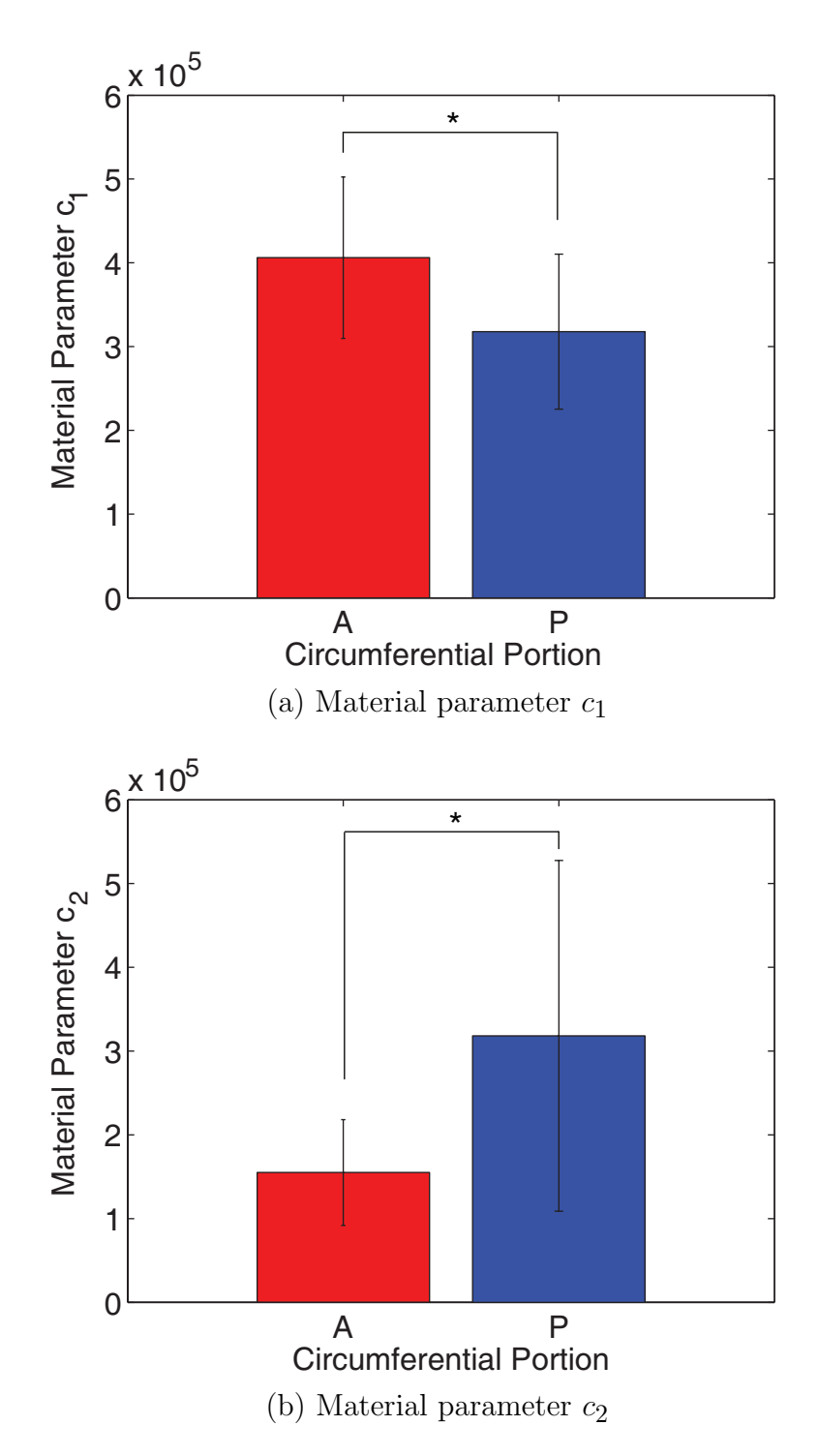


Fig. 5.20: Comparison of the mean and standard deviation of material parameter  $c_1$  (a) and  $c_2$  (b) between the proximal and distal portions of the thoracic aorta.

## Chapter 6

## CONCLUSION

The majority of computational studies of vascular adaptation have been performed based on the assumption of the homogeneous mechanical properties of a blood vessel. Although a few studies reported the regional heterogeneity in the mechanical properties of the aorta along the aortic tree, the circumferential variation has not been taken into account (Guo and Kassab, 2004; Sokolis, 2007). Recently the local mechanical properties of healthy and diseased ascending thoracic aortas were studied using uniaxial or biaxial tests, but there is little experimental data, based on author's knowledge, to quantify the circumferential variation in mechanical properties of a healthy thoracic aorta. Hence, in this study, the circumferential variation in stiffness of the porcine descending thoracic aorta was experimentally investigated. In order to characterize the local mechanical properties of the aorta, an ex vivo extension-inflation apparatus with a stereo vision system was developed, which allowed us to measure the 3D deformation of a blood vessel, and a stress-strain analysis method using 3D experimental data was developed as well. Then, the material parameters were estimated by the parameter estimation method using a constitutive model based on the constraint mixture theory.

The experimental results of this study indicated a nonuniform distribution of stretch and stress in a local region and nonuniform thickness of a rtic wall along the circumference. The stress-stretch response during the inflation test depends on the local region. These results showed that there was the variation in the stiffness, defined as the tangent of stress-stretch response, among the four circumferential regions and two longitudinal portions. In addition, material parameters showed that there was no significant difference between two circumferential regions (the anterior and posterior regions) for the both proximal and distal portions of the aorta, but that there was a significant difference between two longitudinal portions (the proximal and the distal portions) for the anterior and posterior region of the aorta.

One major finding of this study was that the posterior region of the porcine thoracic aorta was significantly stiffer than the anterior, that is, the circumferential variation in the mechanical properties of the aorta. Interestingly, however, there was no significant difference in the pressure-strain elastic modulus for the proximal thoracic aorta. Another finding was that the distal portion of the porcine thoracic aorta was significantly stiffer than the proximal portions. It shows the longitudinal variation in the mechanical behavior of the thoracic aorta. The parameter estimation based on the mixture theory-based constitutive model suggests that the proximal thoracic aorta exhibited elastin-dominant mechanical behavior and the distal thoracic aorta exhibits the collagen-dominant mechanical behavior. It may cause the longitudinal variation in the mechanical behavior.

Finally, it is suggested that the experimental method and analysis presented in this study can be used in the study of vascular biomechanics. The consistent spatial variations in the mechanical properties of the thoracic aorta increase our understanding of vascular remodeling and adaptation during the progression of vascular diseases or vice versa, and will eventually help to improve clinical treatments and interventions of vascular disease.

# **APPENDICES**

# Appendix A

## Methods

#### A.1 Camera matrix

In general, points in world is expressed in terms of the world coordinate frame. Two coordinate frames between world and camera one may be related via rotation and translation.

Under the pinhole camera model (See Fig. 2.4), a point in the world,  $\mathbf{X} = (X, Y, Z)^T$ , is mapped to the point on the image plane,  $\mathbf{x_{cam}} = (x, y)^T$  in terms of the camera coordinate frame. For the central projective camera, it is a linear mapping between homogenous vectors of world and image points. In the image coordinate  $(fX/Z, fY/Z, f)^T$ , where f is the focal length, the last coordinate of the image point can be ignored. Then,

$$\left\{ \begin{array}{c}
fX \\
fY \\
Z
\end{array} \right\} = \begin{bmatrix}
f & 0 & 0 & 0 \\
0 & f & 0 & 0 \\
0 & 0 & 1 & 0
\end{bmatrix} \left\{ \begin{array}{c}
X \\
Y \\
Z \\
1
\end{array} \right\} 
 \tag{A.1}$$

In practical, the origin in image plane is not at the principal point,  $(p_x, p_y)^T$  which is the point where the line from the camera center perpendicular to the image plane meets the image plane. Then a point  $\mathbf{X_{cam}}$  is mapped to the point  $(fX^c/Z^c + p_x, fY^c/Z^c + p_y)^T$  on

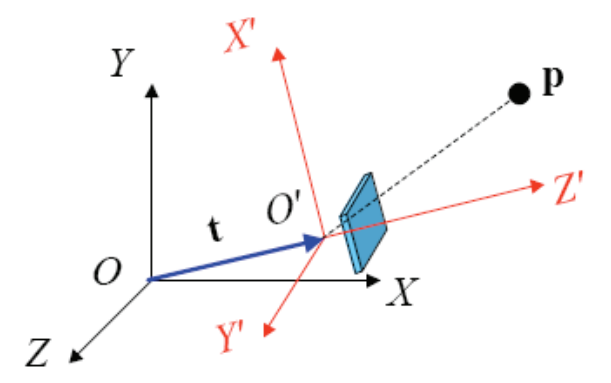


Fig. A.1: Schematics of a world point and its corresponding image point

the image plane.

$$\left\{ \begin{array}{c}
 fX + Zp_x \\
 fY + Zp_y \\
 Z
 \end{array} \right\} = \begin{bmatrix}
 f & 0 & p_x & 0 \\
 0 & f & p_y & 0 \\
 0 & 0 & 1 & 0
\end{bmatrix} \left\{ \begin{array}{c}
 X \\
 Y \\
 Z \\
 1
 \end{array} \right\} \tag{A.2}$$

In general, the camera matrix is determined via three steps. In first step, points (x, y, z) in the camera reference can be obtained the rotation and translation of 3D world points (X, Y, Z) via

$$\begin{cases}
X' \\
Y' \\
Z' \\
1
\end{cases} = \begin{bmatrix}
\mathbf{R}^T & \mathbf{t} \\
\mathbf{0}^T & 1
\end{bmatrix} \begin{cases}
X \\
Y \\
Z \\
1
\end{cases} \tag{A.3}$$

where,  $\mathbf{R}^T$  and  $\mathbf{t}$  represent the rotation matrix and the translation vector, respectively, from the world reference coordinate to the camera reference coordinate.

Next, projection of the points onto the image plane at  $(x_{cam}, y_{cam})$  is written as

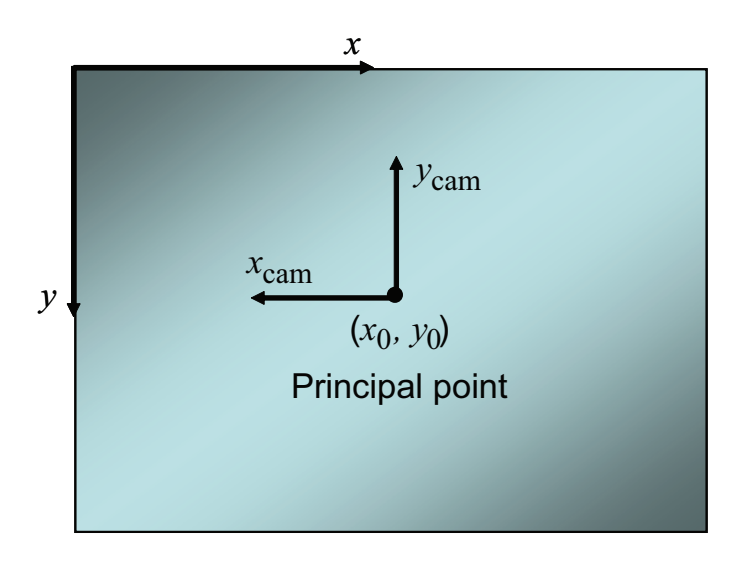


Fig. A.2: Image plane and pixel coordinate

$$\left\{
\begin{array}{c}
x_{cam} \\
y_{cam} \\
f
\end{array}
\right\}
\left[
\begin{array}{cccc}
1 & 0 & 0 & 0 \\
0 & 1 & 0 & 0 \\
0 & 0 & 1 & 0
\end{array}
\right]
\left\{
\begin{array}{c}
X' \\
Y' \\
Z' \\
1
\end{array}
\right\}$$
(A.4)

where, f is the focal length.

Lastly, the mapping from points  $(x_{cam}, y_{cam})$  on the image plane to the pixel coordinates in an image is

$$\left\{ \begin{array}{c} x \\ y \\ 1 \end{array} \right\} = \frac{1}{f} \left[ \begin{array}{ccc} \alpha_x & 0 & x_0 \\ 0 & \alpha_y & y_0 \\ 0 & 0 & 1 \end{array} \right] \left\{ \begin{array}{c} x_{cam} \\ y_{cam} \\ f \end{array} \right\}$$
(A.5)

where,  $\alpha_x$  and  $\alpha_y$  are scaling in x and y directions, respectively,  $(x_0, y_0)$  is the principal point

in the image plane (Fig. A.2). This  $3 \times 3$  matrix is called as camera calibration matrix,

$$\left\{ \begin{array}{c} x \\ y \\ 1 \end{array} \right\} = \frac{1}{f} \left[ \begin{array}{cccc} \alpha_x & 0 & x_0 \\ 0 & \alpha_y & y_0 \\ 0 & 0 & 1 \end{array} \right] \left[ \begin{array}{cccc} 1 & 0 & 0 & 0 \\ 0 & 1 & 0 & 0 \\ 0 & 0 & 1 & 0 \end{array} \right] \left[ \begin{array}{c} \mathbf{R}^T & \mathbf{t} \\ \mathbf{0}^T & 1 \end{array} \right] \left\{ \begin{array}{c} X \\ Y \\ Z \\ 1 \end{array} \right\} \tag{A.6}$$

In homogeneous coordinates, scaling factors  $\frac{1}{f}$  are irrelevant so that it can be discard. A single camera is characterized by 4 internal camera parameters and 6 external camera parameters (3 translations and 3 rotations).

Therefore a finite projective pinhole camera is expressed in terms of a linear mapping of homogeneous coordinates as  $\mathbf{x_{cam}} = P\mathbf{X}$ , where  $P = \mathbf{KR}[\mathbf{I}| \mathbf{t}]$  is the camera matrix with 11 degrees of freedom. That is, P can be as

$$\left\{ \begin{array}{c} sx \\ sy \\ s \end{array} \right\} = \begin{bmatrix} P_{11} & P_{12} & P_{13} & P_{14} \\ P_{21} & P_{22} & P_{23} & P_{24} \\ P_{31} & P_{32} & P_{33} & 1 \end{bmatrix} \left\{ \begin{array}{c} X \\ Y \\ Z \\ 1 \end{array} \right\} \tag{A.7}$$

where a scaling factor  $s = P_{31}X + P_{32}Y + P_{33}Z$ . Then, all image points yield  $2n \times 11$  matrix in the form of  $\mathbf{u} = \mathbf{Ab}$  and pseudo-inverse method can be applied to find a vector  $\mathbf{b}$ . The camera matrix is determined by the known measurement of calibration jig. At least 6 pairs of image points and world points of the jig are required. Then equation (5) can be rewritten as

where n is the number of points. Pseudo Inverse Method (Least Squares Estimation) is employed to find the optimized unknown affine camera matrix parameters  $P_{ij}$ .

# Appendix B

# Analysis

## B.1 Derivatives of the parameters for the curvature

#### **B.1.1** Reference Configuration

In the reference configuration,  $S = S(\overline{S})$ ,  $\Theta = \Theta(\overline{\Theta})$  and  $R \approx \hat{R}(S, \Theta) = \hat{R}(S(\overline{S}), \Theta(\overline{\Theta})) = \hat{R}(\overline{S}, \overline{\Theta})$ , where

$$\hat{R} = \sum_{k=1}^{n} \delta_k P_k(\overline{S}, \overline{\Theta})$$
 (B.1)

The first derivatives of X and Y with respect to  $\overline{S}$  and  $\overline{\Theta}$  are

$$\frac{\partial X}{\partial \overline{S}} \approx \frac{\partial \hat{R}}{\partial \overline{S}} \cos \Theta \tag{B.2}$$

$$\frac{\partial X}{\partial \overline{\Theta}} \approx \frac{\partial \hat{R}}{\partial \overline{\Theta}} \cos \Theta + \hat{R} \frac{\partial \cos \Theta}{\partial \overline{\Theta}}$$
 (B.3)

$$\frac{\partial Y}{\partial \overline{S}} \approx \frac{\partial \hat{R}}{\partial \overline{S}} \sin \Theta \tag{B.4}$$

$$\frac{\partial Y}{\partial \overline{\Theta}} \approx \frac{\partial \hat{R}}{\partial \overline{\Theta}} \sin \Theta + \hat{R} \frac{\partial \sin \Theta}{\partial \overline{\Theta}}$$
 (B.5)

$$\frac{\partial Z}{\partial \overline{S}} = \frac{\partial S}{\partial \overline{S}} \tag{B.6}$$

$$\frac{\partial Z}{\partial \overline{\Theta}} = \frac{\partial S}{\partial \overline{\Theta}} \tag{B.7}$$

$$\frac{\partial \hat{R}}{\partial \overline{S}} = \sum_{k=1}^{n} \delta_k \frac{\partial P_k(\overline{S}, \overline{\Theta})}{\partial \overline{S}}$$
 (B.8)

$$\frac{\partial \hat{R}}{\partial \overline{\Theta}} = \sum_{k=1}^{n} \delta_k \frac{\partial P_k(\overline{S}, \overline{\Theta})}{\partial \overline{\Theta}}$$
 (B.9)

$$\frac{\partial \cos \Theta}{\partial \overline{\Theta}} = \frac{\partial \cos \Theta}{\partial \Theta} \frac{\partial \Theta}{\partial \overline{\Theta}}$$
 (B.10)

$$\frac{\partial \sin \Theta}{\partial \overline{\Theta}} = \frac{\partial \sin \Theta}{\partial \Theta} \frac{\partial \Theta}{\partial \overline{\Theta}}$$
 (B.11)

$$\frac{\partial \cos \Theta}{\partial \Theta} = -\sin \Theta \tag{B.12}$$

$$\frac{\partial \sin \Theta}{\partial \Theta} = \cos \Theta \tag{B.13}$$

$$\frac{\partial \Theta}{\partial \overline{\Theta}} = \frac{\Theta_{max} - \Theta_{min}}{2} \tag{B.14}$$

$$\frac{\partial S}{\partial \overline{S}} = \frac{S_{max} - S_{min}}{2} \tag{B.15}$$

$$\frac{\partial S}{\partial \overline{\Theta}} = 0 \tag{B.16}$$

The second derivatives of X and Y with respect to  $\overline{S}$  and  $\overline{\Theta}$  are

$$\frac{\partial^2 X}{\partial \overline{S}^2} = \frac{\partial^2 \hat{R}}{\partial \overline{S}^2} \cos \Theta \tag{B.17}$$

$$\frac{\partial^2 X}{\partial \overline{\Theta}^2} = \frac{\partial^2 \hat{R}}{\partial \overline{\Theta}^2} \cos \Theta + 2 \left( \frac{\partial \hat{R}}{\partial \overline{\Theta}} \frac{\partial \cos \Theta}{\partial \overline{\Theta}} \right) + \hat{R} \frac{\partial^2 \cos \Theta}{\partial \overline{\Theta}^2}$$
 (B.18)

$$\frac{\partial^2 X}{\partial \overline{S} \partial \overline{\Theta}} = \frac{\partial^2 R}{\partial \overline{S} \partial \overline{\Theta}} \cos \Theta + \frac{\partial R}{\partial \overline{S}} \frac{\partial \cos \Theta}{\partial \overline{\Theta}}$$
(B.19)

$$\frac{\partial^2 Y}{\partial \overline{S}^2} = \frac{\partial^2 \hat{R}}{\partial \overline{S}^2} \sin \Theta \tag{B.20}$$

$$\frac{\partial^2 Y}{\partial \overline{\Theta}^2} = \frac{\partial^2 \hat{R}}{\partial \overline{\Theta}^2} \sin \Theta + 2 \left( \frac{\partial \hat{R}}{\partial \overline{\Theta}} \frac{\partial \sin \Theta}{\partial \overline{\Theta}} \right) + \hat{R} \frac{\partial^2 \sin \Theta}{\partial \overline{\Theta}^2}$$
 (B.21)

$$\frac{\partial^2 Y}{\partial \overline{S} \partial \overline{\Theta}} = \frac{\partial^2 R}{\partial \overline{S} \partial \overline{\Theta}} \sin \Theta + \frac{\partial R}{\partial \overline{S}} \frac{\partial \sin \Theta}{\partial \overline{\Theta}}$$
(B.22)

$$\frac{\partial^2 Z}{\partial \overline{S}^2} = \frac{\partial^2 S}{\partial \overline{S}^2} \tag{B.23}$$

$$\frac{\partial^2 Z}{\partial \overline{\Theta}^2} = \frac{\partial^2 S}{\partial \overline{\Theta}^2} \tag{B.24}$$

$$\frac{\partial^2 Z}{\partial \overline{S} \partial \overline{\Theta}} = \frac{\partial^2 S}{\partial \overline{S} \partial \overline{\Theta}} \tag{B.25}$$

$$\frac{\partial^2 R}{\partial \overline{S}^2} = \sum_{k=1}^n \delta_k \frac{\partial^2 P_k(\overline{S}, \overline{\Theta})}{\partial \overline{S}^2}$$
 (B.26)

$$\frac{\partial^2 R}{\partial \overline{\Theta}^2} = \sum_{k=1}^n \delta_k \frac{\partial^2 P_k(\overline{S}, \overline{\Theta})}{\partial \overline{\Theta}^2}$$
 (B.27)

$$\frac{\partial^{2} R}{\partial \overline{S} \partial \overline{\Theta}} = \sum_{k=1}^{n} \delta_{k} \frac{\partial^{2} P_{k}(\overline{S}, \overline{\Theta})}{\partial \overline{S} \partial \overline{\Theta}}$$
(B.28)

$$\frac{\partial^2 \cos \Theta}{\partial \overline{\Theta}^2} = \frac{\partial \cos \Theta}{\partial \Theta} \left( \frac{\partial \Theta}{\partial \overline{\Theta}} \right)^2 + \frac{\partial \cos \Theta}{\partial \Theta} \left( \frac{\partial^2 \Theta}{\partial \overline{\Theta}^2} \right) \tag{B.29}$$

$$\frac{\partial^2 \sin \Theta}{\partial \overline{\Theta}^2} = \frac{\partial \sin \Theta}{\partial \Theta} \left( \frac{\partial \Theta}{\partial \overline{\Theta}} \right)^2 + \frac{\partial \sin \Theta}{\partial \Theta} \left( \frac{\partial^2 \Theta}{\partial \overline{\Theta}^2} \right) \tag{B.30}$$

$$\frac{\partial \Theta}{\partial \overline{\Theta}} = 0 \tag{B.31}$$

$$\frac{\partial^2 S}{\partial \overline{S}^2} = 0 \tag{B.32}$$

$$\frac{\partial^2 S}{\partial \overline{\Theta}^2} = 0 \tag{B.33}$$

$$\frac{\partial^2 S}{\partial \overline{S} \partial \Theta} = 0 \tag{B.34}$$

#### **B.1.2** Current Configuration

The polar coordinate  $(r, \theta, s)$  will be converted to the cartesian coordinate (x, y, z)

$$x = r\cos\theta \approx \hat{r}\left(\overline{s}, \overline{\theta}\right)\cos\hat{\theta}\left(\overline{S}, \overline{\Theta}\right) \tag{B.35}$$

$$y = r \sin \theta \approx \hat{r} \left( \overline{s}, \overline{\theta} \right) \sin \hat{\theta} \left( \overline{S}, \overline{\Theta} \right)$$
 (B.36)

$$z = s \approx \hat{s} \left( \overline{S}, \overline{\Theta} \right) \tag{B.37}$$

where,

$$\hat{s} = \sum_{k=1}^{n} \alpha_k P_k \left( \overline{S}, \overline{\Theta} \right) \tag{B.38}$$

$$\hat{\theta} = \sum_{k=1}^{n} \beta_k P_k \left( \overline{S}, \overline{\Theta} \right) \tag{B.39}$$

$$\hat{r} = \sum_{k=1}^{n} \gamma_k P_k \left( \overline{s}, \overline{\theta} \right) \tag{B.40}$$

The first forms of the surface are

$$\frac{\partial x}{\partial \overline{S}} = \frac{\partial \hat{r}}{\partial \overline{S}} \cos \hat{\theta} + \hat{r} \frac{\partial \cos \hat{\theta}}{\partial \overline{S}}$$
 (B.41)

$$\frac{\partial x}{\partial \overline{\Theta}} = \frac{\partial \hat{r}}{\partial \overline{\Theta}} \cos \hat{\theta} + \hat{r} \frac{\partial \cos \hat{\theta}}{\partial \overline{\Theta}}$$
 (B.42)

$$\frac{\partial y}{\partial \overline{S}} = \frac{\partial \hat{r}}{\partial \overline{S}} \sin \hat{\theta} + \hat{r} \frac{\partial \sin \hat{\theta}}{\partial \overline{S}}$$
 (B.43)

$$\frac{\partial y}{\partial \overline{\Theta}} = \frac{\partial \hat{r}}{\partial \overline{\Theta}} \sin \hat{\theta} + \hat{r} \frac{\partial \sin \hat{\theta}}{\partial \overline{\Theta}}$$
 (B.44)

$$\frac{\partial z}{\partial \overline{S}} \approx \frac{\partial \hat{s}}{\partial \overline{S}} \tag{B.45}$$

$$\frac{\partial z}{\partial \overline{\Theta}} \approx \frac{\partial \hat{s}}{\partial \overline{\Theta}} \tag{B.46}$$

$$\frac{\partial \hat{r}}{\partial \overline{S}} = \frac{\partial \hat{r}}{\partial \overline{s}} \frac{\partial \overline{s}}{\partial \hat{s}} \frac{\partial \hat{s}}{\partial \overline{S}} + \frac{\partial \hat{r}}{\partial \overline{\theta}} \frac{\partial \overline{\theta}}{\partial \hat{\theta}} \frac{\partial \hat{\theta}}{\partial \overline{S}}$$
(B.47)

$$\frac{\partial \hat{r}}{\partial \overline{\Theta}} = \frac{\partial \hat{r}}{\partial \overline{s}} \frac{\partial \overline{s}}{\partial \hat{s}} \frac{\partial \hat{s}}{\partial \overline{\Theta}} + \frac{\partial \hat{r}}{\partial \overline{\theta}} \frac{\partial \overline{\theta}}{\partial \hat{\theta}} \frac{\partial \hat{\theta}}{\partial \overline{\Theta}}$$
(B.48)

$$\frac{\partial \sin \hat{\theta}}{\partial \overline{S}} = \frac{\partial \sin \hat{\theta}}{\partial \hat{\theta}} \frac{\partial \hat{\theta}}{\partial \overline{S}} \tag{B.49}$$

$$\frac{\partial \sin \hat{\theta}}{\partial \overline{\Theta}} = \frac{\partial \sin \hat{\theta}}{\partial \hat{\theta}} \frac{\partial \hat{\theta}}{\partial \overline{\Theta}}$$
 (B.50)

$$\frac{\partial \cos \hat{\theta}}{\partial \overline{S}} = \frac{\partial \cos \hat{\theta}}{\partial \hat{\theta}} \frac{\partial \hat{\theta}}{\partial \overline{S}}$$
 (B.51)

$$\frac{\partial \cos \hat{\theta}}{\partial \overline{\Theta}} = \frac{\partial \cos \hat{\theta}}{\partial \hat{\theta}} \frac{\partial \hat{\theta}}{\partial \overline{\Theta}}$$
 (B.52)

$$\frac{\partial \hat{s}}{\partial \overline{S}} = \sum_{k=1}^{n} \alpha_k \frac{\partial P_k(\overline{S}, \overline{\Theta})}{\partial \overline{S}}$$
 (B.53)

$$\frac{\partial \hat{s}}{\partial \overline{\Theta}} = \sum_{k=1}^{n} \alpha_k \frac{\partial P_k \left( \overline{S}, \overline{\Theta} \right)}{\partial \overline{\Theta}}$$
 (B.54)

$$\frac{\partial \hat{\theta}}{\partial \overline{S}} = \sum_{k=1}^{n} \beta_k \frac{\partial P_k \left( \overline{S}, \overline{\Theta} \right)}{\partial \overline{S}}$$
 (B.55)

$$\frac{\partial \hat{\theta}}{\partial \overline{\Theta}} = \sum_{k=1}^{n} \beta_k \frac{\partial P_k \left( \overline{S}, \overline{\Theta} \right)}{\partial \overline{\Theta}}$$
 (B.56)

and where,

$$\frac{\partial \overline{s}}{\partial \hat{s}} = \frac{2}{\hat{s}_{max} - \hat{s}_{min}} \tag{B.57}$$

$$\frac{\partial \overline{\theta}}{\partial \hat{\theta}} = \frac{2}{\hat{\theta}_{max} - \hat{\theta}_{min}} \tag{B.58}$$

$$\frac{\partial \hat{r}}{\partial \overline{s}} = \sum_{k=1}^{n} \gamma_k \frac{\partial P_k(\overline{s}, \overline{\theta})}{\partial \overline{s}}$$
 (B.59)

$$\frac{\partial \hat{r}}{\partial \overline{\theta}} = \sum_{k=1}^{n} \gamma_k \frac{\partial P_k \left( \overline{s}, \overline{\theta} \right)}{\partial \overline{\theta}}$$
 (B.60)

$$\frac{\partial \cos \hat{\theta}}{\partial \hat{\theta}} = -\sin \hat{\theta} \tag{B.61}$$

$$\frac{\partial \sin \hat{\theta}}{\partial \hat{\theta}} = \cos \hat{\theta} \tag{B.62}$$

The second forms of the surface are

$$\frac{\partial^2 x}{\partial \overline{S}^2} = \frac{\partial^2 \hat{r}}{\partial \overline{S}^2} \cos \hat{\theta} + 2 \left( \frac{\partial \hat{r}}{\partial \overline{S}} \frac{\partial \cos \hat{\theta}}{\partial \overline{S}} \right) + \hat{r} \frac{\partial^2 \cos \hat{\theta}}{\partial \overline{S}^2}$$
 (B.63)

$$\frac{\partial^2 x}{\partial \overline{\Theta}^2} = \frac{\partial^2 \hat{r}}{\partial \overline{\Theta}^2} \cos \hat{\theta} + 2 \left( \frac{\partial \hat{r}}{\partial \overline{\Theta}} \frac{\partial \cos \hat{\theta}}{\partial \overline{\Theta}} \right) + \hat{r} \frac{\partial^2 \cos \hat{\theta}}{\partial \overline{\Theta}^2}$$
 (B.64)

$$\frac{\partial^2 x}{\partial \overline{S} \partial \Theta} = \frac{\partial^2 \hat{r}}{\partial \overline{S} \partial \overline{\Theta}} \cos \hat{\theta} + \frac{\partial \hat{r}}{\partial \overline{\Theta}} \frac{\partial \cos \hat{\theta}}{\partial \overline{S}} + \frac{\partial \hat{r}}{\partial \overline{S}} \frac{\partial \cos \hat{\theta}}{\partial \overline{\Theta}} + \hat{r} \frac{\partial^2 \cos \hat{\theta}}{\partial \overline{S} \partial \overline{\Theta}}$$
(B.65)

$$\frac{\partial^2 y}{\partial \overline{S}^2} = \frac{\partial^2 \hat{r}}{\partial \overline{S}^2} \sin \hat{\theta} + 2 \left( \frac{\partial \hat{r}}{\partial \overline{S}} \frac{\partial \sin \hat{\theta}}{\partial \overline{S}} \right) + \hat{r} \frac{\partial^2 \sin \hat{\theta}}{\partial \overline{S}^2}$$
 (B.66)

$$\frac{\partial^2 y}{\partial \overline{\Theta}^2} = \frac{\partial^2 \hat{r}}{\partial \overline{\Theta}^2} \sin \hat{\theta} + 2 \left( \frac{\partial \hat{r}}{\partial \overline{\Theta}} \frac{\partial \sin \hat{\theta}}{\partial \overline{\Theta}} \right) + \hat{r} \frac{\partial^2 \sin \hat{\theta}}{\partial \overline{\Theta}^2}$$
 (B.67)

$$\frac{\partial^2 y}{\partial \overline{S}\partial \Theta} = \frac{\partial^2 \hat{r}}{\partial \overline{S}\partial \overline{\Theta}} \sin \hat{\theta} + \frac{\partial \hat{r}}{\partial \overline{\Theta}} \frac{\partial \sin \hat{\theta}}{\partial \overline{S}} + \frac{\partial \hat{r}}{\partial \overline{S}} \frac{\partial \sin \hat{\theta}}{\partial \overline{\Theta}} + \hat{r} \frac{\partial^2 \sin \hat{\theta}}{\partial \overline{S}\partial \overline{\Theta}}$$
(B.68)

$$\frac{\partial^2 z}{\partial \overline{S}^2} \approx \frac{\partial^2 \hat{s}}{\partial \overline{S}^2} \tag{B.69}$$

$$\frac{\partial^2 z}{\partial \overline{\Theta}^2} \approx \frac{\partial^2 \hat{s}}{\partial \overline{\Theta}^2} \tag{B.70}$$

$$\frac{\partial^2 z}{\partial \overline{S} \partial \overline{\Theta}} \approx \frac{\partial^2 \hat{s}}{\partial \overline{S} \partial \overline{\Theta}} \tag{B.71}$$

Equations in the second forms are

$$\frac{\partial^{2} \hat{r}}{\partial \overline{S}^{2}} = \frac{\partial^{2} \hat{r}}{\partial \overline{s}^{2}} \left(\frac{\partial \overline{s}}{\partial \hat{s}}\right)^{2} \left(\frac{\partial \hat{s}}{\partial \overline{S}}\right)^{2} + \frac{\partial \hat{r}}{\partial \overline{s}} \frac{\partial^{2} \overline{s}}{\partial \hat{s}^{2}} \left(\frac{\partial \hat{s}}{\partial \overline{S}}\right)^{2} + \frac{\partial \hat{r}}{\partial \overline{s}} \frac{\partial \overline{s}}{\partial \hat{s}} \frac{\partial^{2} \hat{s}}{\partial \overline{s}^{2}} + \frac{\partial^{2} \hat{r}}{\partial \overline{\theta}^{2}} \left(\frac{\partial \hat{\theta}}{\partial \overline{\theta}}\right)^{2} \left(\frac{\partial \hat{\theta}}{\partial \overline{S}}\right)^{2} + \frac{\partial \hat{r}}{\partial \overline{\theta}} \frac{\partial^{2} \overline{\theta}}{\partial \hat{\theta}^{2}} \left(\frac{\partial \hat{\theta}}{\partial \overline{S}}\right)^{2} + \frac{\partial \hat{r}}{\partial \overline{\theta}} \frac{\partial \overline{\theta}}{\partial \hat{\theta}} \frac{\partial^{2} \hat{\theta}}{\partial \overline{\theta}^{2}} \right) \tag{B.72}$$

$$\frac{\partial^{2} \hat{r}}{\partial \overline{\Theta}^{2}} = \frac{\partial^{2} \hat{r}}{\partial \overline{s}^{2}} \left( \frac{\partial \overline{s}}{\partial \hat{s}} \right)^{2} \left( \frac{\partial \hat{s}}{\partial \overline{\Theta}} \right)^{2} + \frac{\partial \hat{r}}{\partial \overline{s}} \frac{\partial^{2} \overline{s}}{\partial \hat{s}^{2}} \left( \frac{\partial \hat{s}}{\partial \overline{\Theta}} \right)^{2} + \frac{\partial \hat{r}}{\partial \overline{s}} \frac{\partial \overline{s}}{\partial \hat{s}} \frac{\partial^{2} \hat{s}}{\partial \overline{\Theta}^{2}} + \frac{\partial^{2} \hat{r}}{\partial \overline{\theta}^{2}} \left( \frac{\partial \hat{\theta}}{\partial \overline{\Theta}} \right)^{2} + \frac{\partial^{2} \hat{r}}{\partial \overline{\theta}^{2}} \left( \frac{\partial \hat{\theta}}{\partial \overline{\Theta}} \right)^{2} + \frac{\partial \hat{r}}{\partial \overline{\theta}} \frac{\partial^{2} \overline{\theta}}{\partial \overline{\theta}^{2}} \left( \frac{\partial \hat{\theta}}{\partial \overline{\Theta}} \right)^{2} + \frac{\partial \hat{r}}{\partial \overline{\theta}} \frac{\partial^{2} \overline{\theta}}{\partial \overline{\theta}^{2}} \left( \frac{\partial \hat{\theta}}{\partial \overline{\Theta}} \right)^{2} + \frac{\partial \hat{r}}{\partial \overline{\theta}} \frac{\partial^{2} \hat{\theta}}{\partial \overline{\theta}^{2}} \right) \tag{B.73}$$

$$\frac{\partial^{2} \hat{r}}{\partial \overline{S} \partial \overline{\Theta}} = \frac{\partial^{2} \hat{r}}{\partial \overline{s}^{2}} \left( \frac{\partial \overline{s}}{\partial \hat{s}} \right)^{2} \frac{\partial \hat{s}}{\partial \overline{S}} \frac{\partial s}{\partial \overline{\Theta}} + \frac{\partial \hat{r}}{\partial \overline{s}} \frac{\partial^{2} \overline{s}}{\partial \overline{S}^{2}} \frac{\partial \hat{s}}{\partial \overline{\Theta}} + \frac{\partial \hat{r}}{\partial \overline{s}} \frac{\partial \overline{s}}{\partial \overline{S}} \frac{\partial \overline{s}}{\partial \overline{\Theta}} + \frac{\partial \hat{r}}{\partial \overline{s}} \frac{\partial \overline{s}}{\partial \overline{S}} \frac{\partial^{2} \hat{s}}{\partial \overline{S}} \frac{\partial^{2} \hat{s}}{\partial \overline{S}} + \frac{\partial^{2} \hat{r}}{\partial \overline{s}} \frac{\partial^{2} \hat{s}}{\partial \overline{S}} \frac{\partial^{2} \hat{s}}{\partial \overline{S}} + \frac{\partial^{2} \hat{r}}{\partial \overline{s}} \frac{\partial^{2} \hat{s}}{\partial \overline{S}} \frac{\partial^{2} \hat{s}}{\partial \overline{S}} \frac{\partial^{2} \hat{s}}{\partial \overline{S}} + \frac{\partial^{2} \hat{r}}{\partial \overline{s}} \frac{\partial^{2} \hat{s}}{\partial \overline{S}} \frac$$

$$\frac{\partial^2 \cos \hat{\theta}}{\partial \overline{S}^2} = \frac{\partial^2 \cos \hat{\theta}}{\partial \hat{\theta}^2} \left( \frac{\partial \hat{\theta}}{\partial \overline{S}} \right)^2 + \frac{\partial \cos \hat{\theta}}{\partial \hat{\theta}} \frac{\partial^2 \hat{\theta}}{\partial \overline{S}^2}$$
(B.75)

$$\frac{\partial^2 \cos \hat{\theta}}{\partial \overline{\Theta}^2} = \frac{\partial^2 \cos \hat{\theta}}{\partial \hat{\theta}^2} \left( \frac{\partial \hat{\theta}}{\partial \overline{\Theta}} \right)^2 + \frac{\partial \cos \hat{\theta}}{\partial \hat{\theta}} \frac{\partial^2 \hat{\theta}}{\partial \overline{\Theta}^2}$$
(B.76)

$$\frac{\partial^2 \cos \hat{\theta}}{\partial \overline{S} \partial \overline{\Theta}} = \frac{\partial^2 \cos \hat{\theta}}{\partial \hat{\theta}^2} \frac{\partial \hat{\theta}}{\partial \overline{S}} \frac{\partial \hat{\theta}}{\partial \overline{\Theta}} + \frac{\partial \cos \hat{\theta}}{\partial \hat{\theta}} \frac{\partial^2 \hat{\theta}}{\partial S \partial \overline{\Theta}}$$
(B.77)

$$\frac{\partial^2 \sin \hat{\theta}}{\partial \overline{S}^2} = \frac{\partial}{\partial \overline{S}} \left( \frac{\partial \sin \hat{\theta}}{\partial \overline{S}} \right) = \frac{\partial^2 \sin \hat{\theta}}{\partial \hat{\theta}^2} \left( \frac{\partial \hat{\theta}}{\partial \overline{S}} \right)^2 + \frac{\partial \sin \hat{\theta}}{\partial \hat{\theta}} \frac{\partial^2 \hat{\theta}}{\partial \overline{S}^2}$$
(B.78)

$$\frac{\partial^2 \sin \hat{\theta}}{\partial \overline{\Theta}^2} = \frac{\partial^2 \sin \hat{\theta}}{\partial \hat{\theta}^2} \left( \frac{\partial \hat{\theta}}{\partial \overline{\Theta}} \right)^2 + \frac{\partial \sin \hat{\theta}}{\partial \hat{\theta}} \frac{\partial^2 \hat{\theta}}{\partial \overline{\Theta}^2}$$
(B.79)

$$\frac{\partial^2 \sin \hat{\theta}}{\partial \overline{S} \partial \overline{\Theta}} = \frac{\partial^2 \sin \hat{\theta}}{\partial \hat{\theta}^2} \frac{\partial \hat{\theta}}{\partial \overline{S}} \frac{\partial \hat{\theta}}{\partial \overline{\Theta}} + \frac{\partial \sin \hat{\theta}}{\partial \hat{\theta}} \frac{\partial^2 \hat{\theta}}{\partial \overline{S} \partial \overline{\Theta}}$$
(B.80)

$$\frac{\partial^2 \hat{s}}{\partial \overline{S}^2} = \sum_{k=1}^n \alpha_k \frac{\partial^2 P_k \left( \overline{S}, \overline{\Theta} \right)}{\partial \overline{S}^2}$$
 (B.81)

$$\frac{\partial^2 \hat{s}}{\partial \overline{\Theta}^2} = \sum_{k=1}^n \alpha_k \frac{\partial^2 P_k \left( \overline{S}, \overline{\Theta} \right)}{\partial \overline{\Theta}^2}$$
 (B.82)

$$\frac{\partial^{2} \hat{s}}{\partial \overline{S} \partial \overline{\Theta}} = \sum_{k=1}^{n} \alpha_{k} \frac{\partial^{2} P_{k} \left( \overline{S}, \overline{\Theta} \right)}{\partial \overline{S} \partial \overline{\Theta}}$$
(B.83)

$$\frac{\partial^2 \hat{\theta}}{\partial \overline{S}^2} = \sum_{k=1}^n \beta_k \frac{\partial^2 P_k \left( \overline{S}, \overline{\Theta} \right)}{\partial \overline{S}^2}$$
 (B.84)

$$\frac{\partial^2 \hat{\theta}}{\partial \overline{\Theta}^2} = \sum_{k=1}^n \beta_k \frac{\partial^2 P_k \left( \overline{S}, \overline{\Theta} \right)}{\partial \overline{\Theta}^2}$$
 (B.85)

$$\frac{\partial^2 \hat{\theta}}{\partial \overline{S} \partial \overline{\Theta}} = \sum_{k=1}^n \beta_k \frac{\partial^2 P_k \left( \overline{S}, \overline{\Theta} \right)}{\partial \overline{S} \partial \overline{\Theta}}$$
 (B.86)

$$\frac{\partial^2 \hat{r}}{\partial \bar{s}^2} = \sum_{k=1}^n \gamma_k \frac{\partial^2 P_k \left( \bar{s}, \bar{\theta} \right)}{\partial \bar{s}^2} \tag{B.87}$$

$$\frac{\partial^2 \hat{r}}{\partial \overline{\theta}^2} = \sum_{k=1}^n \gamma_k \frac{\partial^2 P_k \left( \overline{s}, \overline{\theta} \right)}{\partial \overline{\theta}^2}$$
 (B.88)

$$\frac{\partial^2 \hat{r}}{\partial \bar{s} \partial \bar{\theta}} = \sum_{k=1}^n \gamma_k \frac{\partial^2 P_k \left( \bar{s}, \bar{\theta} \right)}{\partial \bar{s} \partial \bar{\theta}} \tag{B.89}$$

$$\frac{\partial^2 \overline{s}}{\partial \hat{s}^2} = 0 \tag{B.90}$$

$$\frac{\partial^2 \overline{\theta}}{\partial \hat{\theta}^2} = 0 \tag{B.91}$$

$$\frac{\partial^2 \cos \hat{\theta}}{\partial \hat{\theta}^2} = \frac{\partial}{\partial \hat{\theta}} \left( \frac{\partial \cos \hat{\theta}}{\partial \hat{\theta}} \right) = \frac{\partial}{\partial \hat{\theta}} \left( -\sin \hat{\theta} \right) = -\cos \hat{\theta}$$
 (B.92)

$$\frac{\partial^2 \sin \hat{\theta}}{\partial \hat{\theta}^2} = \frac{\partial}{\partial \hat{\theta}} \left( \frac{\partial \sin \hat{\theta}}{\partial \hat{\theta}} \right) = \frac{\partial}{\partial \hat{\theta}} \left( \cos \hat{\theta} \right) = -\sin \hat{\theta}$$
 (B.93)

#### B.2 Gaussian quadrature

Gaussian quadrature rule is an approximation of the integral of a function and it is usually represented by a sum of a weight and a function at specified points within the domain of integration. It yields an exact result for polynomials by a suitable choice of the points  $x_i$  and weights  $w_i$  for i = 1, ..., n. The integration domain for the rule is conventionally taken

as [-1, 1], so the rule is stated as

$$\int_{-1}^{1} f(x) dx \approx \sum_{i=1}^{n} w_i f(x_i).$$
 (B.94)

An integral over an arbitrary interval [a, b] should be changed into an integral over [-1, 1] to apply the Gaussian quadrature rule. This change of interval can be done as the following:

$$\int_{a}^{b} f(x)dx = \frac{b-a}{2} \int_{-1}^{1} f(\frac{b-a}{2}x + \frac{b+a}{2})dx$$
 (B.95)

After applying the Gaussian quadrature rule, the following approximation can be

$$\int_{a}^{b} f(x) dx \approx \frac{b-a}{2} \sum_{i=1}^{n} w_{i} f\left(\frac{b-a}{2} x_{i} + \frac{b+a}{2}\right).$$
 (B.96)

For example, the total cross-sectional area of the vessel ring can be divided by constant finite domains.

$$\int_{0}^{2\pi} h(\theta)r(\theta)d\theta = \sum_{i=1}^{N^{e}} \int_{a}^{b} h(\theta)r(\theta)d\theta$$
 (B.97)

where  $N^e$  is total number of finite intervals over the domain and a and b are the starting and ending position of each finite interval. In this case, total domain length is  $L_0 = 2\pi$ , each finite domain length is  $L = 2\pi/N^e$ , then a = (j-1)L and b = jL for  $j^{th}$  finite domain. In order to use Gaussian quadrants, the finite domain length can be converted to [-1 1]. Therefore,

$$\int_{a}^{b} f(x) dx = \frac{b-a}{2} \int_{-1}^{1} f\left(\frac{b+a}{2} + \frac{b-a}{2}t\right) dt$$
 (B.98)

Using the Gaussian quadrants, the integral can be expressed by a summation of function of Gaussian points and weights. The integration part can be

$$\int_{-1}^{1} f(t)dt = \sum_{j=1}^{N^g} w_j f(t_j)dt$$
 (B.99)

where  $N^g$  is total number of Gaussian points. equation (B.97) can be rewritten as

$$\int_0^{2\pi} h(\theta) r(\theta) d\theta = \sum_{i=1}^{N^e} \sum_{j=1}^{N^g} w_j \left( \frac{b-a}{2} \right) \left\{ h \left( \frac{b+a}{2} + \frac{b-a}{2} \theta_j \right) r \left( \frac{b+a}{2} + \frac{b-a}{2} \theta_j \right) \right\} d\theta$$
(B.100)

Some low-order Gaussian points and weights are listed below.

Number of points, n	Points, $x_i$	Weights, $w_i$
1	0	2
2	$\pm 1/\sqrt{3}$	1
9	0	8/9
3	$\pm\sqrt{15/5}$	5/9

# Appendix C

# Results

### C.1 Information of the aorta sample

In this study, we tested 7 proximal thoracic aortas and 4 distal thoracic aortas were tested. For the convenience of displaying the results, we name each sample and tabulate their information in Table C.1.

Table C.1: Information of all aorta samples

Sample	Longitudinal portion	Circumferential region	Histology
No.	(Prox/Dis)	(A/L/P/R)	sample
1	Prox	A, L, P, R	No
2	Prox	A, L, P, R	Yes
3	Prox	A, L, P, R	Yes
4	Prox	A, L, P, R	Yes
5	Prox	A, L, P, R	Yes
6	Prox	A, L, P, R	Yes
7	Prox	A, L, P, R	Yes
8	Dis	A, L, P, R	No
9	Dis	A, P (L, R for $\Lambda$ =1.35, 1.40)	No
10	Dis	A, P	Yes
11	Dis	A, P	Yes

### C.2 Stress-stretch plots

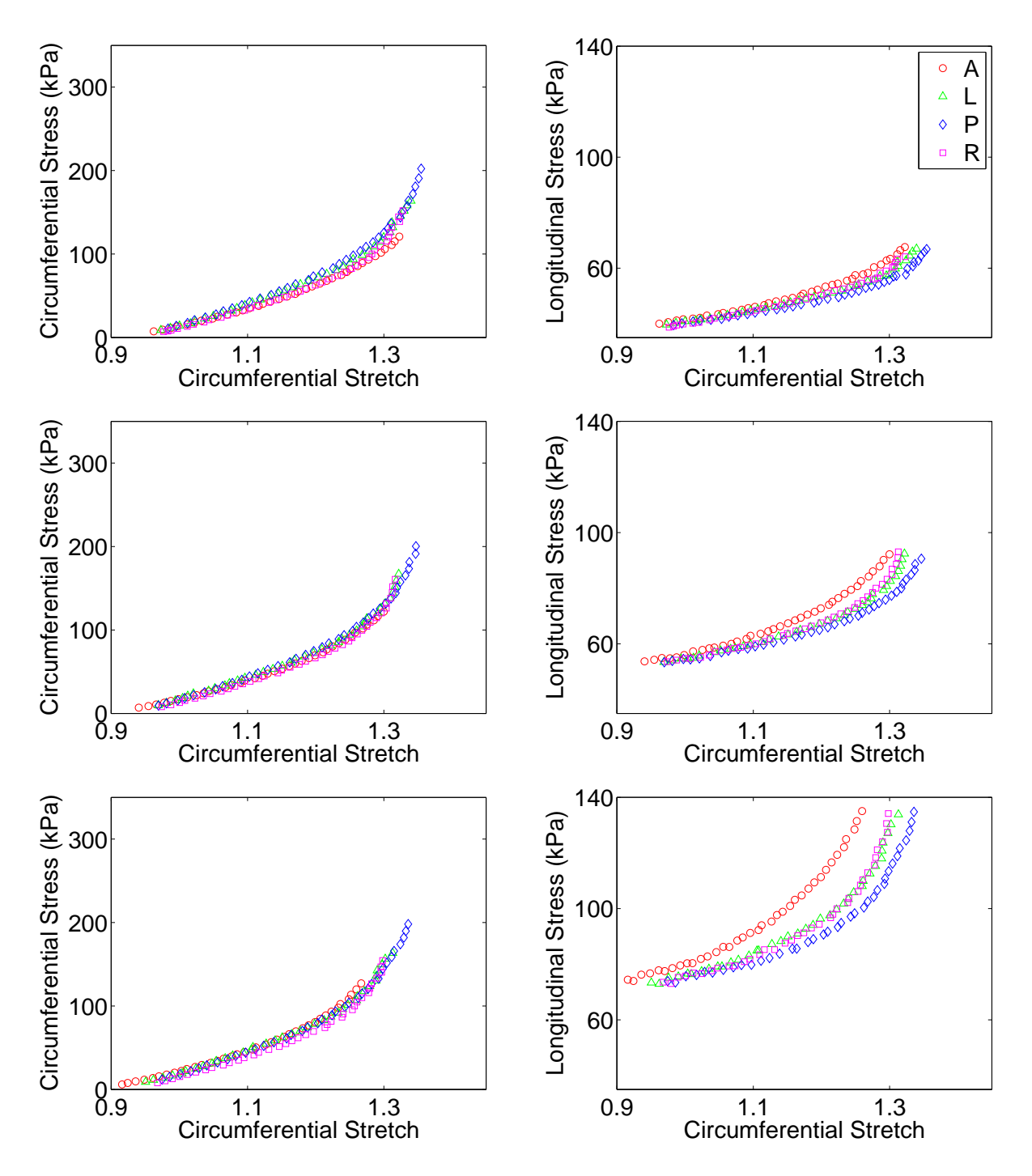


Fig. C.1: Stress-stretch plots for the proximal thoracic aorta at a fixed stretch ratio of 1.35, 1.40, and 1.45 for sample 1

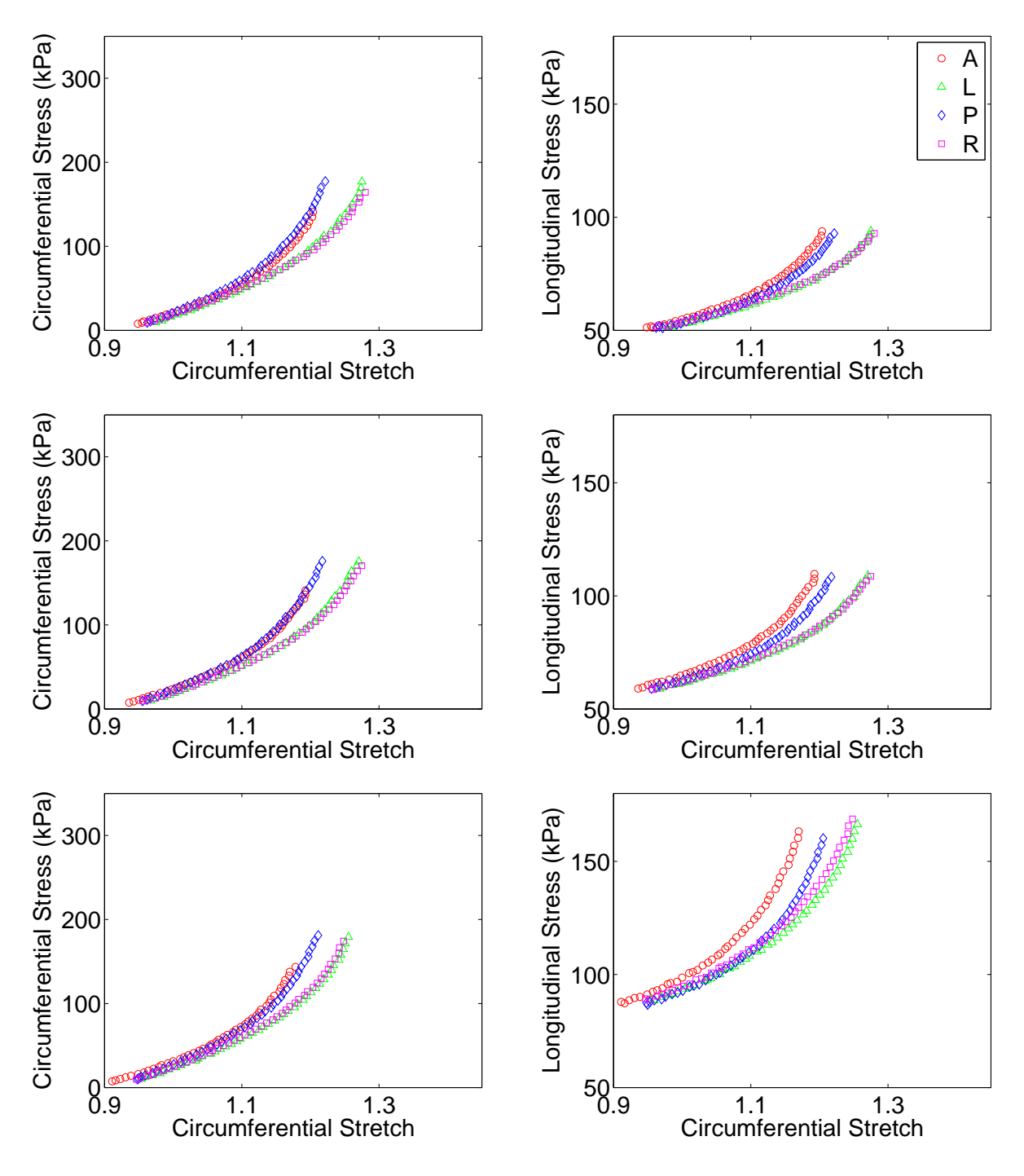


Fig. C.2: Stress-stretch plots for the proximal thoracic aorta at a fixed stretch ratio of 1.35, 1.40, and 1.45 for sample 2

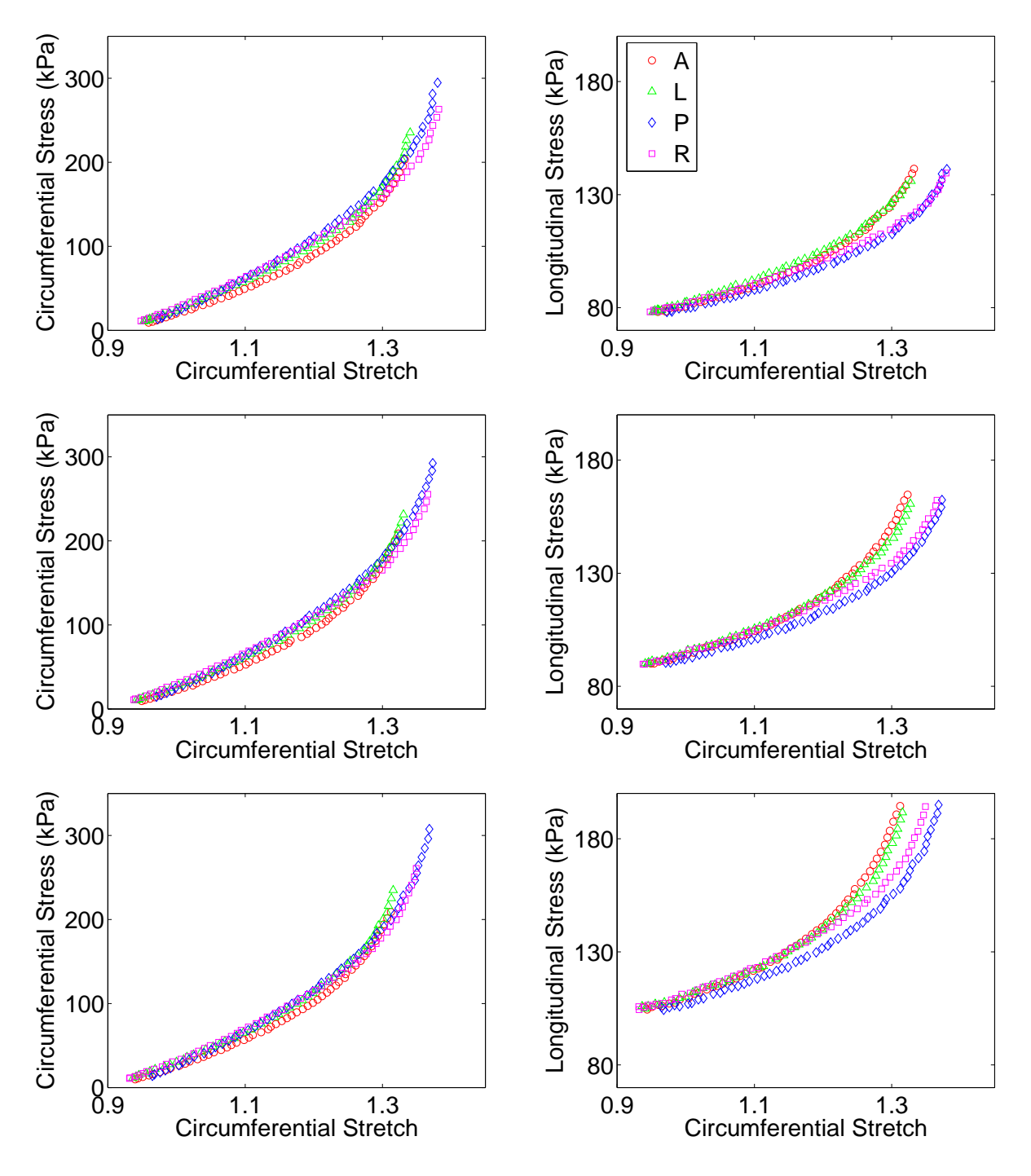


Fig. C.3: Stress-stretch plots for the proximal thoracic aorta at a fixed stretch ratio of 1.35, 1.40, and 1.45 for sample 3

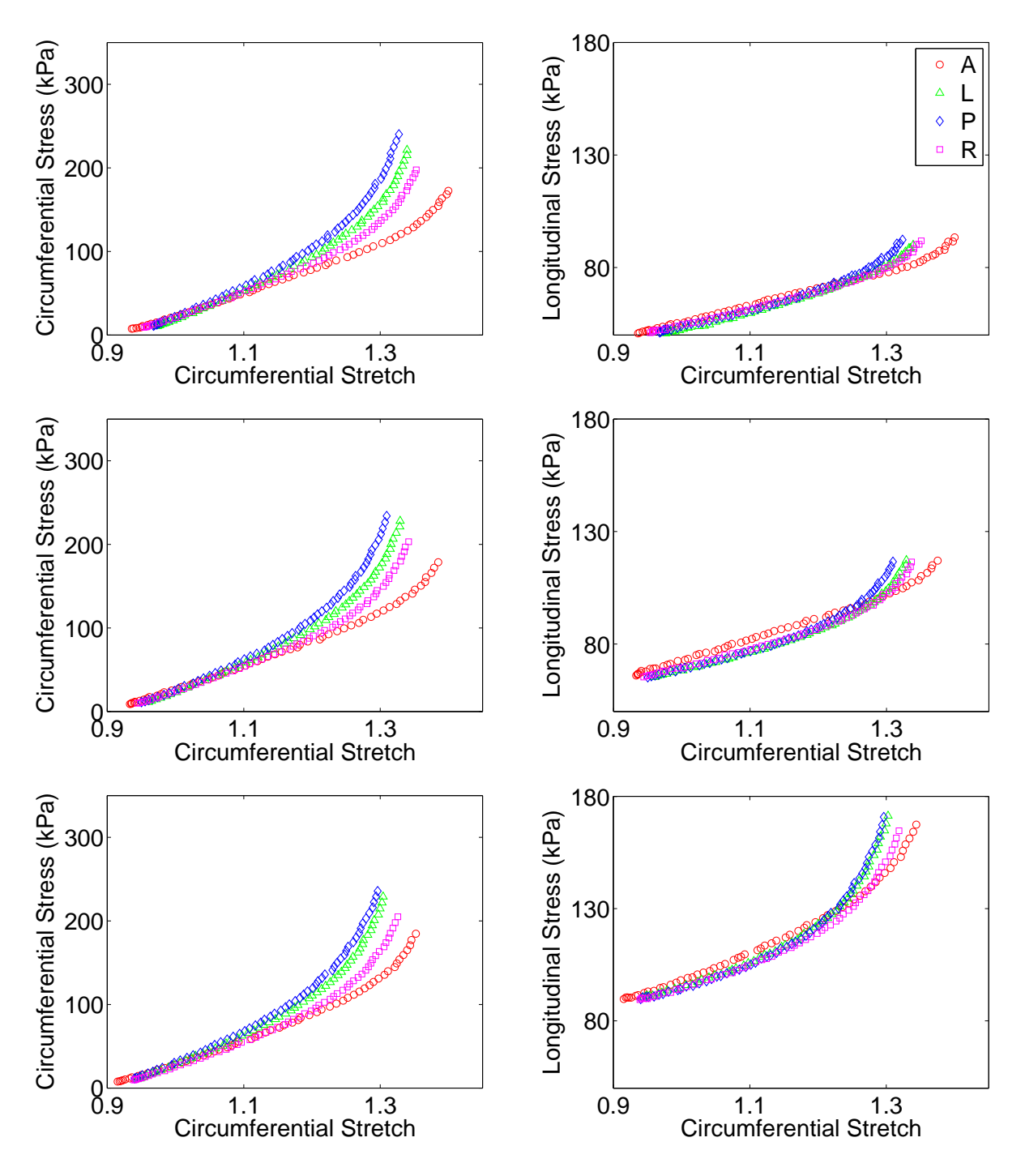


Fig. C.4: Stress-stretch plots for the proximal thoracic aorta at a fixed stretch ratio of 1.35, 1.40, and 1.45 for sample 4

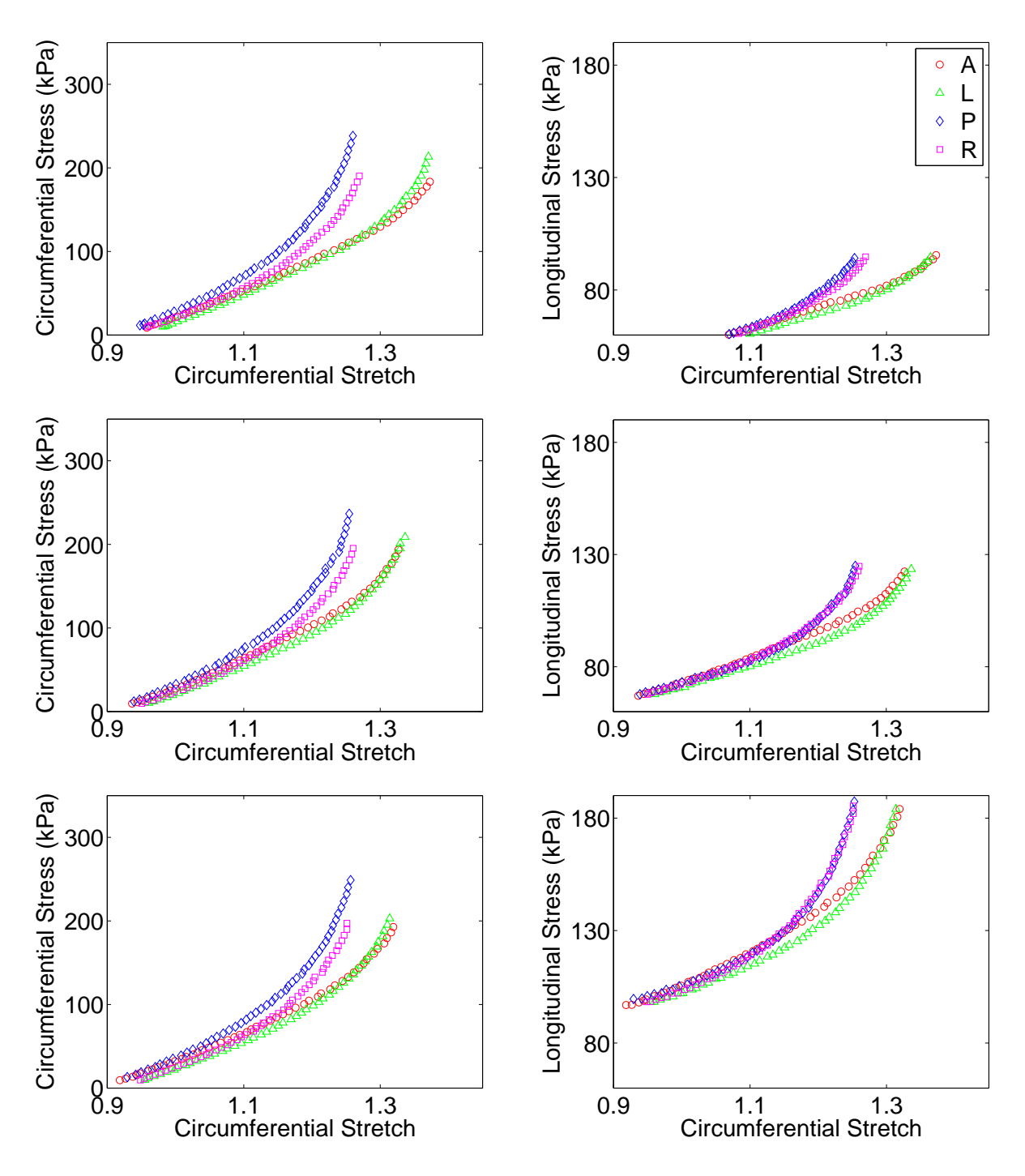


Fig. C.5: Stress-stretch plots for the proximal thoracic aorta at a fixed stretch ratio of 1.35, 1.40, and 1.45 for sample 5

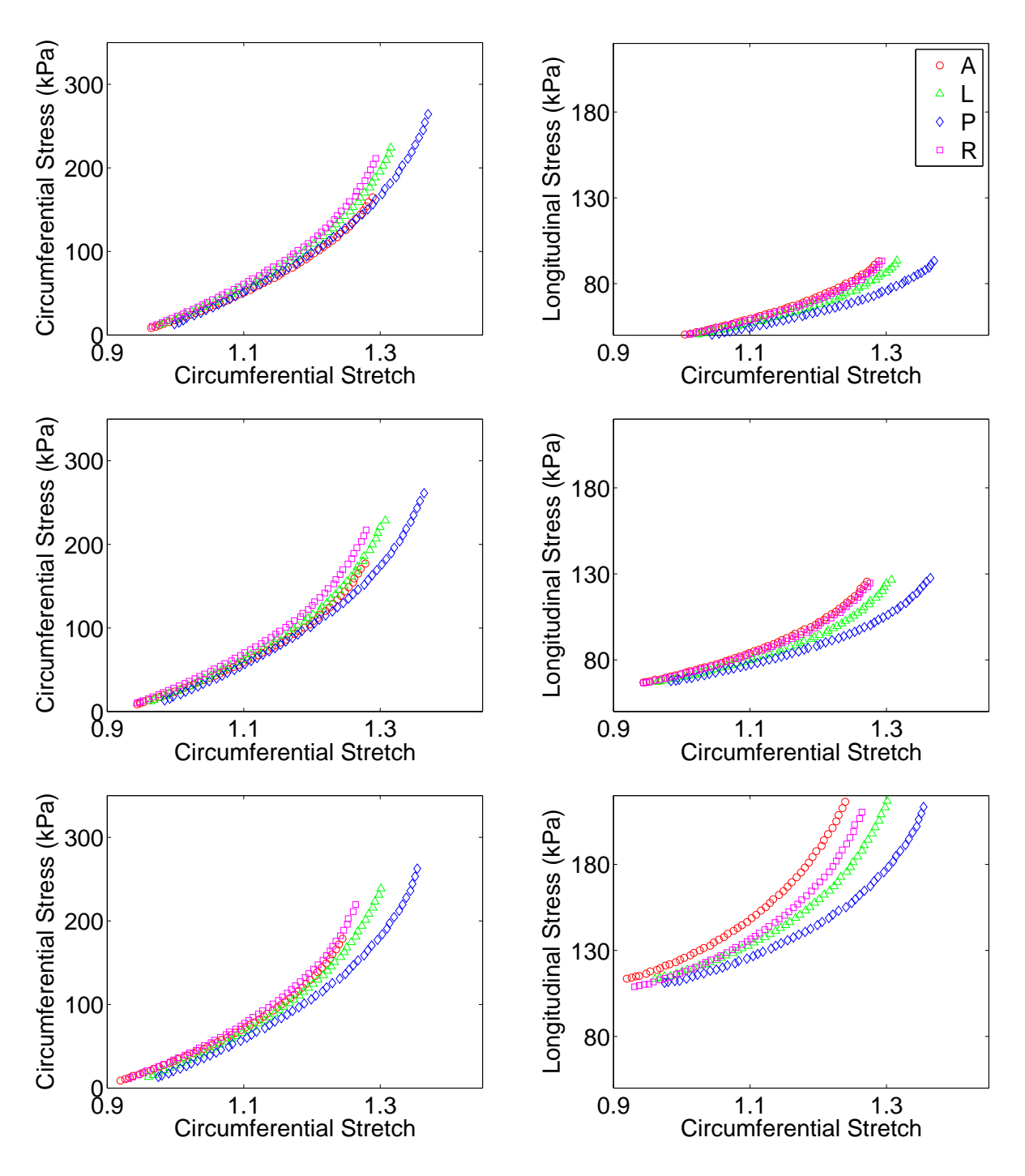


Fig. C.6: Stress-stretch plots for the proximal thoracic aorta at a fixed stretch ratio of 1.35, 1.40, and 1.45 for sample 6

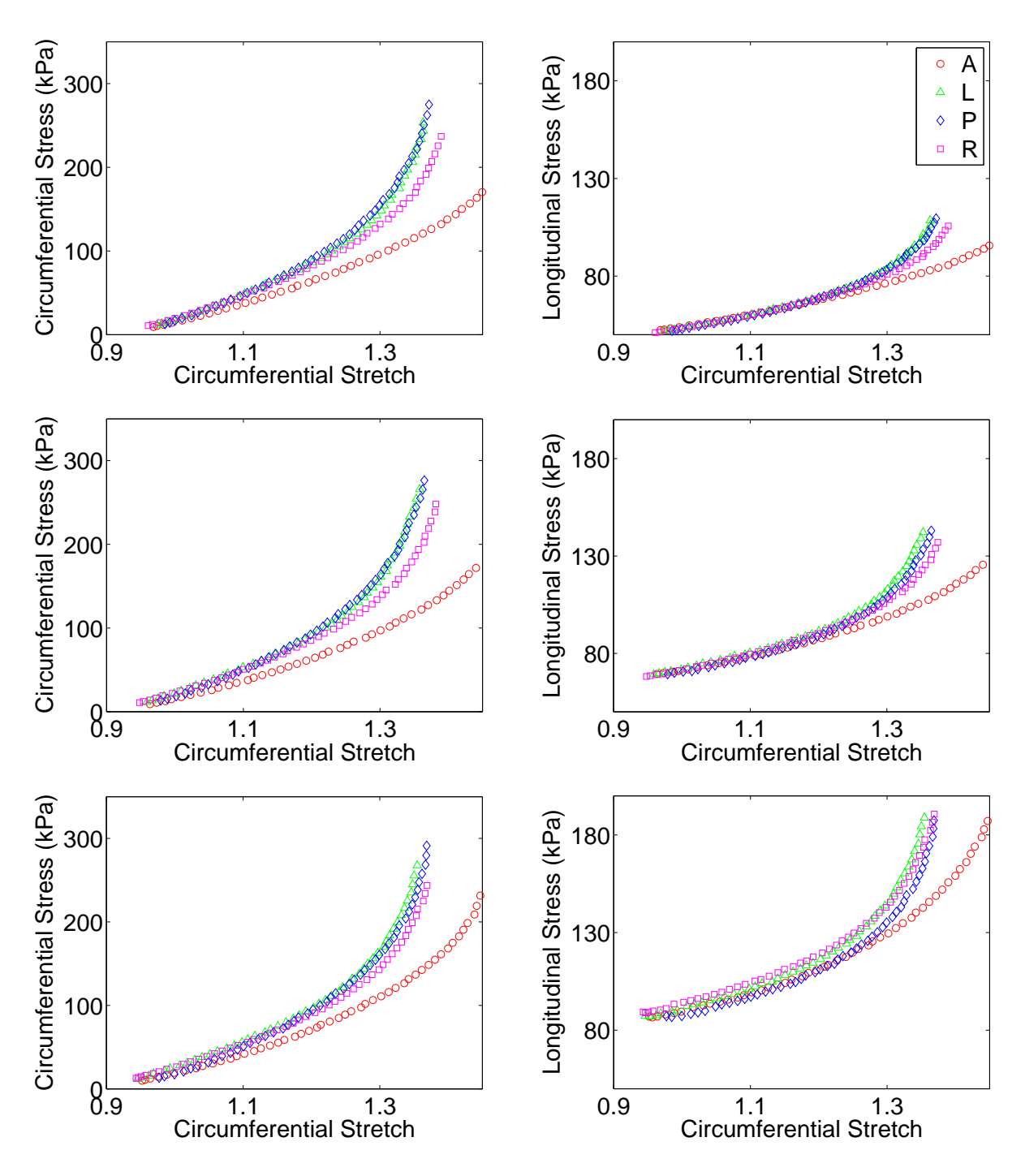


Fig. C.7: Stress-stretch plots for the proximal thoracic aorta at a fixed stretch ratio of 1.35, 1.40, and 1.45 for sample 7

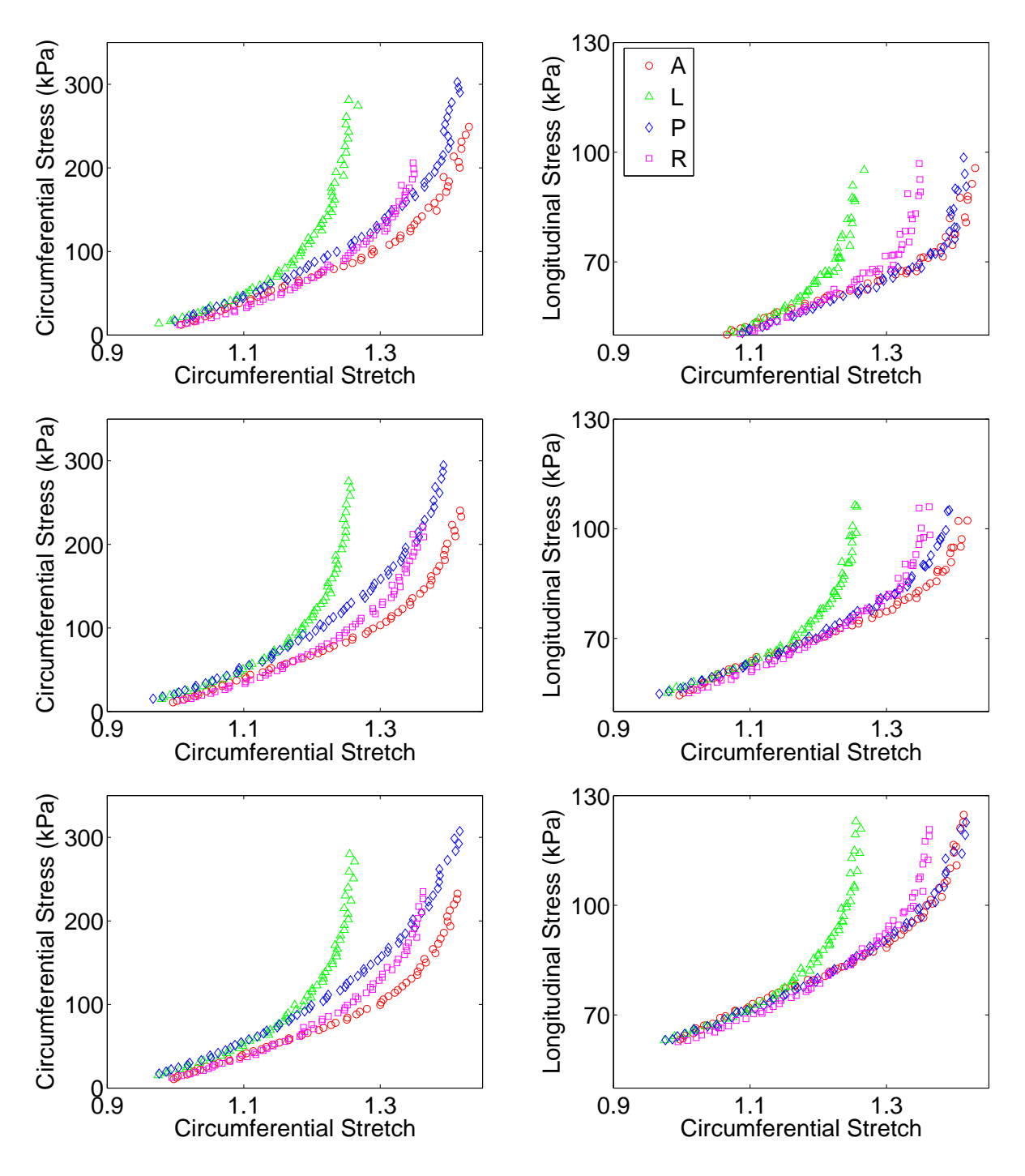


Fig. C.8: Stress-stretch plots for the distal thoracic aorta at a fixed stretch ratio of 1.35, 1.40, and 1.45 sample 8

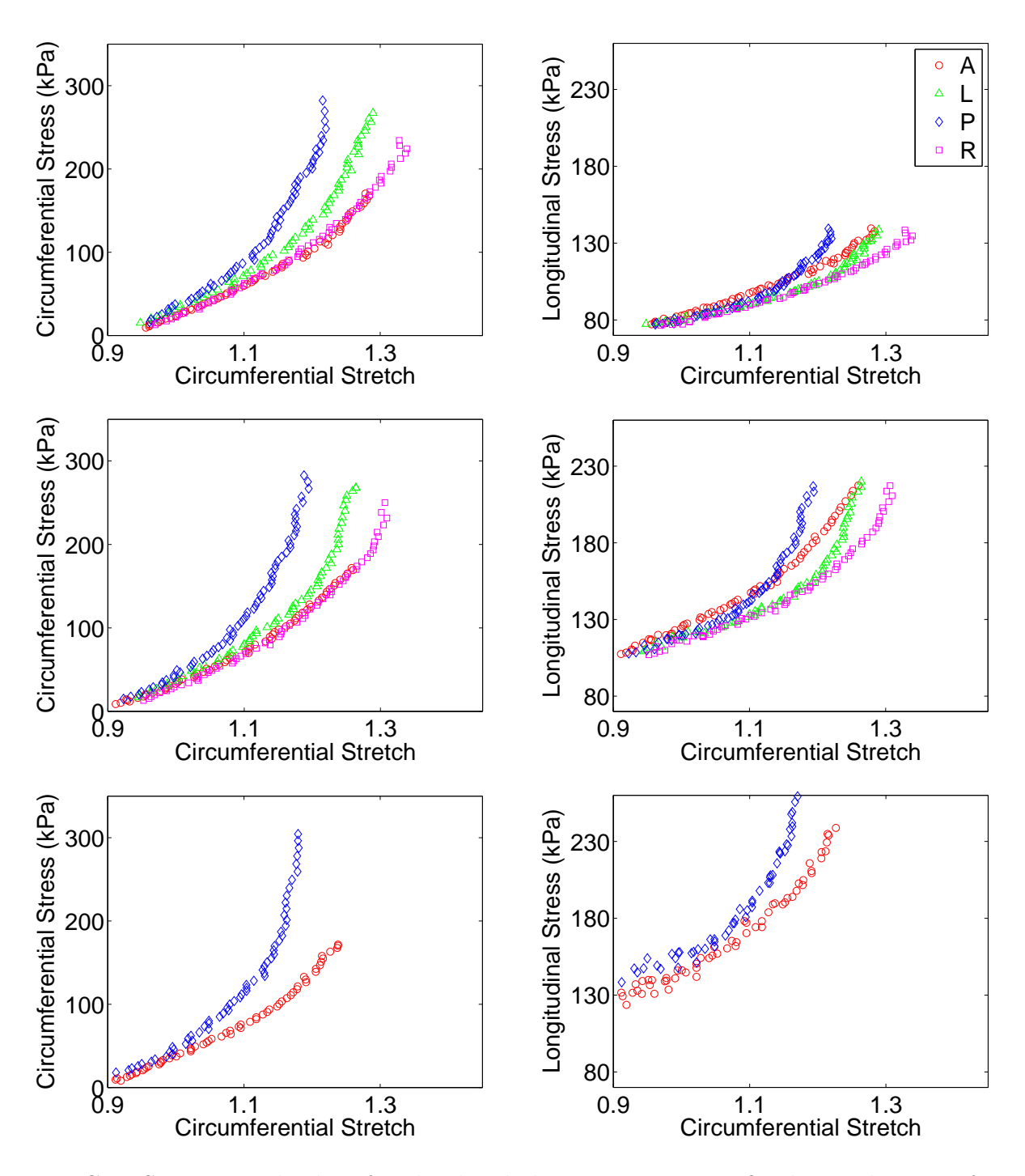


Fig. C.9: Stress-stretch plots for the distal thoracic aorta at a fixed stretch ratio of 1.35, 1.40, and 1.45 sample 9

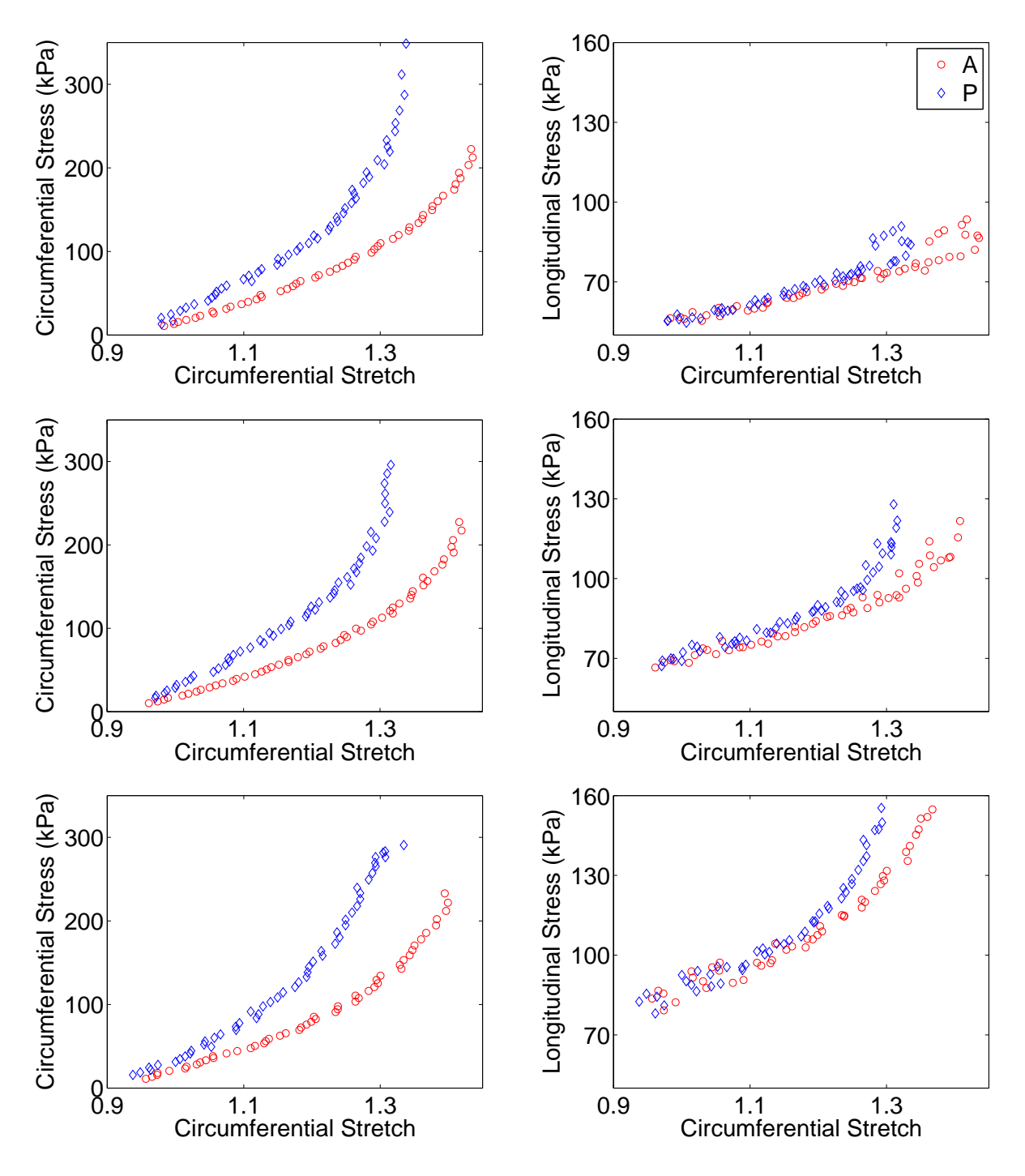


Fig. C.10: Stress-stretch plots for the distal thoracic agrta at a fixed stretch ratio of 1.35, 1.40, and 1.45 sample 10

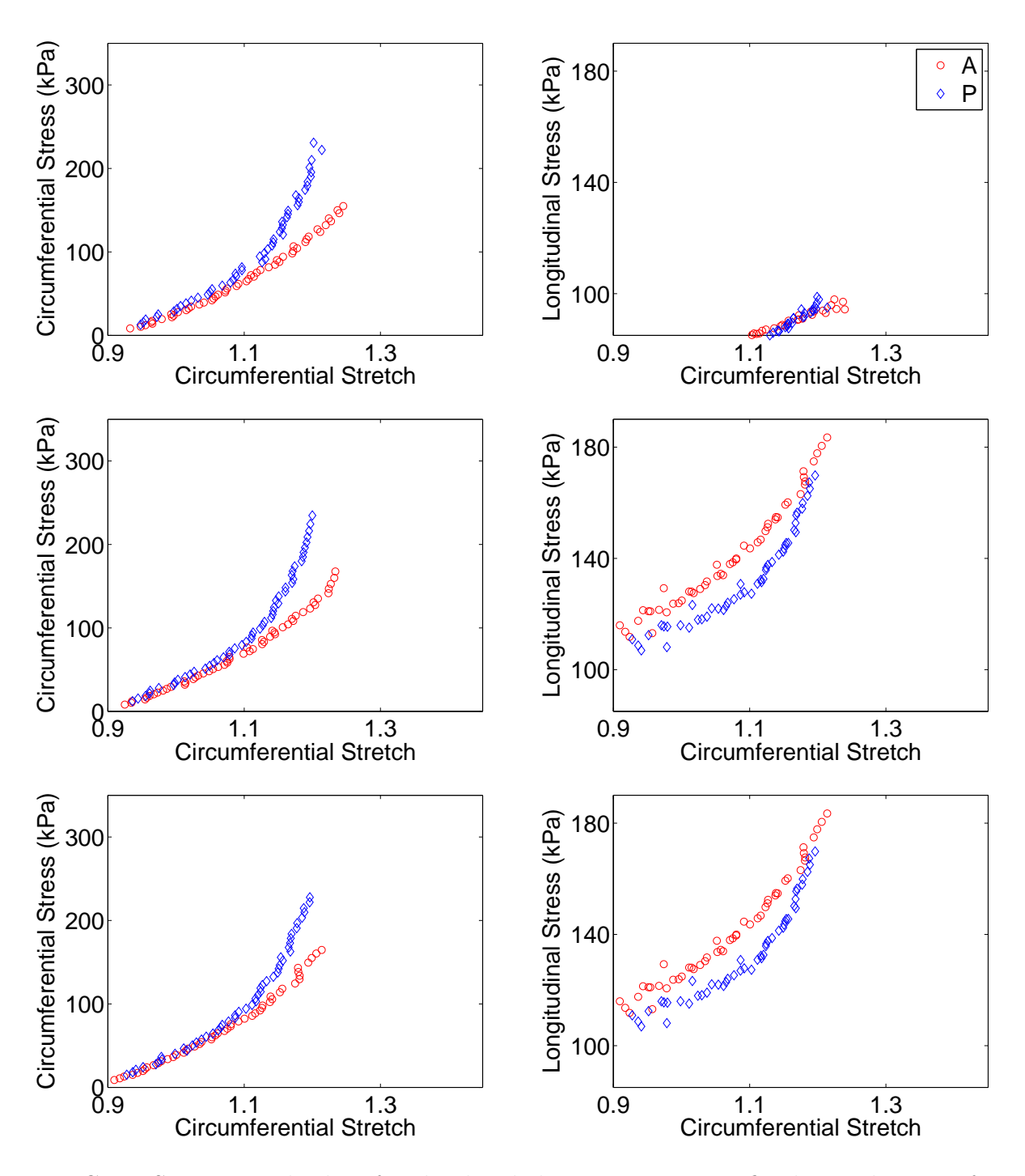


Fig. C.11: Stress-stretch plots for the distal thoracic agrta at a fixed stretch ratio of 1.35, 1.40, and 1.45 sample 11

#### C.3 Stretch, stress, and stiffness

Table C.2: The mean and the standard deviation of the circumferential stretch of the thoracic aorta at the transmural pressure of  $8.00~\rm kPa$  ( $60~\rm mm$  Hg),  $12.00~\rm kPa$  ( $90~\rm mm$  Hg), and  $16.00~\rm kPa$  ( $120~\rm mm$  Hg) for each proximal circumferential region

$\Lambda$ =1.35	8.00 kPa	12.00 kPa	16.00 kPa
Anterior	$1.10 \pm 0.04$	$1.20 \pm 0.06$	$1.29 \pm 0.08$
Left lateral	$1.11 \pm 0.02$	$1.22 \pm 0.03$	$1.30 \pm 0.03$
Posterior	$1.12 \pm 0.03$	$1.22 \pm 0.05$	$1.29 \pm 0.06$
Right lateral	$1.10 \pm 0.02$	$1.21 \pm 0.04$	$1.29 \pm 0.05$
$\Lambda$ =1.40	8.00 kPa	12.00 kPa	16.00 kPa
Anterior	$1.09 \pm 0.04$	$1.19 \pm 0.07$	$1.28 \pm 0.08$
Left lateral	$1.10 \pm 0.02$	$1.21 \pm 0.03$	$1.28 \pm 0.03$
Posterior	$1.11 \pm 0.03$	$1.22 \pm 0.05$	$1.28 \pm 0.06$
Right lateral	$1.10 \pm 0.02$	$1.20 \pm 0.04$	$1.28 \pm 0.05$
$\Lambda$ =1.45	8.00 kPa	12.00 kPa	16.00 kPa
Anterior	$1.07 \pm 0.05$	$1.17 \pm 0.07$	$1.25 \pm 0.08$
Left lateral	$1.09 \pm 0.02$	$1.20 \pm 0.03$	$1.27 \pm 0.03$
Posterior	$1.11 \pm 0.04$	$1.21 \pm 0.05$	$1.28 \pm 0.06$
Right lateral	$1.09 \pm 0.02$	$1.19 \pm 0.04$	$1.27 \pm 0.05$

(a) The proximal thoracic aorta

$\Lambda=1.35$	8.00 kPa	12.00 kPa	16.00 kPa
Anterior	$1.12 \pm 0.07$	$1.23 \pm 0.10$	$1.31 \pm 0.11$
Posterior	$1.13 \pm 0.06$	$1.22 \pm 0.09$	$1.27 \pm 0.10$
$\Lambda$ =1.40	8.00 kPa	12.00 kPa	16.00 kPa
Anterior	$1.11 \pm 0.08$	$1.21 \pm 0.11$	$1.28 \pm 0.11$
Posterior	$1.12 \pm 0.06$	$1.20 \pm 0.08$	$1.25 \pm 0.09$
$\Lambda$ =1.45	8.00 kPa	12.00 kPa	16.00 kPa
Anterior	$1.09 \pm 0.09$	$1.20 \pm 0.11$	$1.27 \pm 0.12$
Posterior	$1.11 \pm 0.06$	$1.20 \pm 0.09$	$1.25 \pm 0.10$

(b) The left and right lateral regions

Table C.3: The mean and the standard deviation of the circumferential stress of the thoracic aorta at the transmural pressure of  $8.00~\rm kPa$ ,  $12.00~\rm kPa$ , and  $16.00~\rm kPa$  for each proximal circumferential region (unit: kPa)

$\Lambda$ =1.35	8.00 kPa	12.00 kPa	16.00 kPa
Anterior	$45 \pm 8$	$82 \pm 16$	$126 \pm 25$
Left lateral	$55 \pm 8$	$100 \pm 16$	$154 \pm 22$
Posterior	$63 \pm 9$	$113 \pm 17$	$172 \pm 29$
Right lateral	$52 \pm 9$	$96 \pm 17$	$146 \pm 29$
$\Lambda$ =1.40	8.00 kPa	12.00 kPa	16.00 kPa
Anterior	$46 \pm 8$	$83 \pm 16$	$128 \pm 25$
Left lateral	$56 \pm 9$	$102 \pm 15$	$155 \pm 24$
Posterior	$64 \pm 9$	$116 \pm 19$	$176 \pm 30$
Right lateral	$53 \pm 8$	$97 \pm 16$	$150 \pm 26$
$\Lambda$ =1.45	8.00 kPa	12.00 kPa	16.00 kPa
Anterior	$46 \pm 9$	$84 \pm 17$	$130 \pm 27$
Left lateral	$53 \pm 8$	$104 \pm 17$	$158 \pm 25$
Posterior	$67 \pm 10$	$120 \pm 21$	$181 \pm 34$
Right lateral	$54 \pm 8$	$99 \pm 18$	$152\pm27$

(a) The proximal thoracic aorta

1 1 2 2	0.00.1.D	12.00 LD	4000 1 D
$\Lambda=1.35$	8.00 kPa	12.00  kPa	16.00 kPa
Anterior	$52 \pm 11$	$95 \pm 20$	$146 \pm 31$
Posterior	$79 \pm 9$	$142 \pm 15$	$204 \pm 26$
Λ=1.40	8.00 kPa	12.00 kPa	16.00 kPa
Anterior	$54 \pm 10$	$97 \pm 19$	$146 \pm 29$
Posterior	$80 \pm 9$	$141 \pm 15$	$203 \pm 21$
$\Lambda$ =1.45	8.00 kPa	12.00 kPa	16.00 kPa
Anterior	$54 \pm 10$	$97 \pm 19$	$148 \pm 30$
Posterior	$82 \pm 10$	$148 \pm 24$	$215 \pm 32$

(b) The distal thoracic aorta

Table C.4: The mean and the standard deviation of the circumferential stiffness of the thoracic aorta at the transmural pressure of 8.00 kPa, 12.00 kPa, and 16.00 kPa for each proximal circumferential region (unit: kPa)

$\Lambda$ =1.35	8.00 kPa	12.00 kPa	16.00 kPa
Anterior	$310 \pm 47$	$416 \pm 104$	$671 \pm 185$
Left lateral	$359 \pm 33$	$523 \pm 99$	$1065 \pm 255$
Posterior	$420 \pm 58$	$634 \pm 91$	$1246 \pm 136$
Right lateral	$347 \pm 50$	$489 \pm 82$	$964 \pm 117$
$\Lambda$ =1.40	8.00 kPa	12.00 kPa	16.00 kPa
Anterior	$310 \pm 47$	$416 \pm 104$	$724 \pm 175$
Left lateral	$360 \pm 33$	$523 \pm 99$	$1118 \pm 230$
Posterior	$420 \pm 58$	$634 \pm 91$	$1304 \pm 188$
Right lateral	$347 \pm 51$	$487 \pm 82$	$1043 \pm 124$
$\Lambda$ =1.45	8.00 kPa	12.00 kPa	16.00 kPa
Anterior	$321 \pm 51$	$441 \pm 84$	$765 \pm 177$
Left lateral	$370 \pm 42$	$552 \pm 98$	$1140 \pm 195$
Posterior	$436 \pm 57$	$674 \pm 67$	$1394 \pm 344$
Right lateral	$362 \pm 54$	$535 \pm 87$	$1109 \pm 153$

(a) The proximal thoracic aorta

$\Lambda$ =1.35	8.00 kPa	12.00 kPa	16.00 kPa
Anterior	$348 \pm 61$	$468 \pm 70$	$989 \pm 418$
Posterior	$525 \pm 84$	$1012 \pm 346$	$2151 \pm 444$
$\Lambda$ =1.40	8.00 kPa	12.00 kPa	16.00 kPa
Anterior	$332 \pm 38$	$513 \pm 23$	$945 \pm 416$
Posterior	$592 \pm 100$	$1018 \pm 245$	$1842 \pm 188$
$\Lambda$ =1.45	8.00 kPa	12.00 kPa	16.00 kPa
Anterior	$345 \pm 54$	$516 \pm 69$	$1039 \pm 394$
Posterior	$563 \pm 95$	$1085 \pm 244$	$1925 \pm 768$

(b) The distal thoracic aorta

Table C.5: The mean and the standard deviation of the pressure-strain elastic modulus of the proximal and distal portions of the thoracic aorta for each proximal circumferential region (unit: kPa)

$\Lambda$ =1.35	Proximal	Distal
Anterior	$52 \pm 19$	$56 \pm 8$
Left lateral	$56 \pm 10$	-
Posterior	$62 \pm 14$	$89 \pm 28$
Right lateral	$54 \pm 9$	-
$\Lambda$ =1.40	Proximal	Distal
Anterior	$52 \pm 19$	$56 \pm 8$
Left lateral	$56 \pm 10$	-
Posterior	$62 \pm 14$	$89 \pm 28$
Right lateral	$54 \pm 9$	-
$\Lambda$ =1.45	Proximal	Distal
Anterior	$52 \pm 19$	$56 \pm 8$
Left lateral	$56 \pm 10$	-
Posterior	$62 \pm 14$	$89 \pm 28$
Right lateral	$54 \pm 9$	_

# C.4 Material parameters

Table C.6: Material parameters for the sample 1

Parameters \ Regions	Anterior	Left lateral	Posterior	Right lateral
$c_1 \text{ (kPa)}$	$3.49 \times 10^2$	$2.73 \times 10^2$	$3.79 \times 10^2$	$2.49 \times 10^2$
$c_2 \text{ (kPa)}$	$9.11 \times 10^{1}$	$1.64 \times 10^2$	$2.62 \times 10^{1}$	$1.01 \times 10^2$
$c_3$	5.79	9.57	28.56	17.64
$c_4$ (Pa)	$2.37 \times 10^{-8}$	$1.11 \times 10^{-15}$	$8.29 \times 10^{-8}$	$7.69 \times 10^{-8}$
$c_5$	$1.67 \times 10^{-7}$	$2.00 \times 10^{-16}$	$1.54 \times 10^{-6}$	1.47
$G_1^e$	1.19	1.35	1.30	1.30
$G_2^{ar{e}}$	1.12	1.07	1.11	1.17
$G_h^{ar{c}}$	1.11	1.09	1.09	1.08
$G_{2}^{e}$ $G_{h}^{c}$ $G_{h}^{m}$	1.10	1.10	1.10	1.10
$\alpha(\circ)$	20.14	10.00	28.80	35.83

Table C.7: Material parameters for the sample 2

Parameters \ Regions	Anterior	Left lateral	Posterior	Right lateral
$c_1(kPa)$	$2.85 \times 10^2$	$2.79 \times 10^2$	$2.96 \times 10^2$	$3.23 \times 10^2$
$c_2(kPa)$	$2.04 \times 10^2$	$3.02 \times 10^2$	$2.72 \times 10^2$	$2.39 \times 10^2$
$c_3$	9.89	8.02	10.68	7.56
$c_4(Pa)$	$2.81 \times 10^{-7}$	$9.54 \times 10^{-13}$	$2.47 \times 10^{-8}$	$5.42 \times 10^{-9}$
$c_5$	$4.78 \times 10^{-6}$	$1.80 \times 10^{-3}$	$4.79 \times 10^{-5}$	14.38
$G_1^e$	1.17	1.28	1.22	1.24
$G_2^{ar{e}}$	1.21	1.15	1.20	1.14
$G_h^{\overline{c}}$	1.09	1.09	1.09	1.10
$G_1^e \ G_2^e \ G_h^c \ G_h^m$	1.10	1.10	1.10	1.10
$\alpha(^{\circ})$	38.99	26.23	39.73	25.42

Table C.8: Material parameters for the sample 3

Parameters \ Regions	Anterior	Left lateral	Posterior	Right lateral
$c_1(kPa)$	$4.97 \times 10^2$	$5.34 \times 10^2$	$5.54 \times 10^2$	$4.65 \times 10^2$
$c_2(kPa)$	$1.13 \times 10^2$	$5.89 \times 10^{1}$	$1.42 \times 10^2$	$1.78 \times 10^2$
$c_3$	3.44	3.074	2.93	1.75
$c_4(Pa)$	$1.74 \times 10^{-10}$	$2.62 \times 10^{-10}$	$2.98 \times 10^{-10}$	$1.09 \times 10^{-9}$
$c_5$	$2.92 \times 10^{-10}$	$5.24 \times 10^{-8}$	0.045	$9.31 \times 10^{-5}$
$G_1^e$	1.09	1.06	1.13	1.14
$G_2^e$	1.24	1.23	1.20	1.24
$G_h^{ar{c}} \ G_h^m$	1.08	1.09	1.09	1.09
	1.10	1.10	1.10	1.10
$\alpha(\circ)$	30.44	43.88	40.12	33.75

Table C.9: Material parameters for the sample 4

Parameters \ Regions	Anterior	Left lateral	Posterior	Right lateral
$c_1 \text{ (kPa)}$	$4.24 \times 10^2$	$3.97 \times 10^2$	$3.02 \times 10^2$	$4.32 \times 10^2$
$c_2 \text{ (kPa)}$	$5.10 \times 10^{1}$	$1.85 \times 10^2$	$3.06 \times 10^2$	$9.60 \times 10^{1}$
$c_3$	0.72	1.13	1.19	2.09
$c_4$ (Pa)	$1.44 \times 10^{-11}$	$9.68 \times 10^{-11}$	$1.59 \times 10^{-10}$	$7.86 \times 10^{-10}$
$c_5$	$1.12 \times 10^{-9}$	1.39	0.04	0.15
$G_1^e$	1.05	1.07	1.13	1.09
$G_2^e$	1.20	1.16	1.17	1.18
$G_h^c$	1.08	1.09	1.09	1.09
$G_h^m$	1.10	1.10	1.10	1.10
$\alpha(\circ)$	27.52	27.18	26.90	34.57

Table C.10: Material parameters for the sample 5

Parameters \ Regions	Anterior	Left lateral	Posterior	Right lateral
$c_1 \text{ (kPa)}$	$4.87 \times 10^2$	$3.34 \times 10^2$	$2.60 \times 10^2$	$2.98 \times 10^2$
$c_2 \text{ (kPa)}$	$1.80 \times 10^2$	$3.64 \times 10^2$	$2.89 \times 10^2$	$2.88 \times 10^{2}$
$c_3$	0.12	0.49	4.50	4.79
$c_4$ (Pa)	$2.69 \times 10^{-10}$	$9.34 \times 10^{-10}$	$1.01 \times 10^{-6}$	$1.31 \times 10^{-9}$
$c_5$	$4.99 \times 10^{-7}$	$2.16 \times 10^{-10}$	$2.80 \times 10^{-7}$	$1.48 \times 10^{-7}$
$G_1^e$	1.12	1.18	1.23	1.19
$G_2^e$	1.15	1.14	1.21	1.17
$G_h^{\overline{c}}$	1.08	1.09	1.08	1.09
$G_h^{ ilde{c}}$ $G_h^m$	1.10	1.10	1.10	1.10
$\alpha(\circ)$	20.89	15.65	42.12	28.77

Table C.11: Material parameters for the sample 6

Parameters \ Regions	Anterior	Left lateral	Posterior	Right lateral
$c_1 \text{ (kPa)}$	$3.96 \times 10^2$	$3.49 \times 10^2$	$2.83 \times 10^2$	$3.36 \times 10^2$
$c_2 \text{ (kPa)}$	$1.98 \times 10^2$	$3.06 \times 10^2$	$3.96 \times 10^2$	$2.63 \times 10^2$
$c_3$	2.57	2.12	1.80	4.20
$c_4$ (Pa)	$6.06 \times 10^{-10}$	$4.81 \times 10^{-10}$	$3.39 \times 10^{-10}$	$7.88 \times 10^{-8}$
$c_5$	$1.53 \times 10^{-8}$	$4.92 \times 10^{-12}$	$9.12 \times 10^{-8}$	$3.18 \times 10^{-7}$
$G_1^e$	1.11	1.18	1.28	1.22
$G_2^{ar{e}}$	1.14	1.06	1.03	1.10
$G_h^{ar{c}} \ G_h^m$	1.10	1.11	1.09	1.08
	1.10	1.10	1.10	1.10
$\alpha(\circ)$	19.58	15.60	10.34	24.48

Table C.12: Material parameters for the sample 7

Parameters \ Regions	Anterior	Left lateral	Posterior	Right lateral
$c_1 \text{ (kPa)}$	$3.73 \times 10^2$	$3.18 \times 10^2$	$3.32 \times 10^2$	$3.15 \times 10^2$
$c_2 \text{ (kPa)}$	$1.98 \times 10^2$	$2.04 \times 10^2$	$2.03 \times 10^2$	$2.15 \times 10^2$
$c_3$	0.84	4.28	4.68	2.82
$c_4$ (Pa)	$9.57 \times 10^{-11}$	$3.02 \times 10^{-9}$	$1.51 \times 10^{-5}$	$ 6.10 \times 10^{-10} $
$c_5$	$1.53 \times 10^{-10}$	0.027883	$1.98 \times 10^{-6}$	$6.21 \times 10^{-6}$
$G_1^e$	1.17	1.23	1.23	1.23
$G_2^{ar{e}}$	1.21	1.18	1.18	1.18
$G_h^{\bar{c}}$	1.09	1.11	1.09	1.12
$G_1^e$ $G_2^e$ $G_h^c$ $G_h^m$	1.10	1.10	1.10	1.10
$\alpha(\circ)$	31.19	32.74	42.98	27.18

Table C.13: Material parameters for the sample 8

Parameters \ Regions	Anterior	Posterior		
$c_1 \text{ (kPa)}$	$2.98 \times 10^2$	$3.22 \times 10^2$		
$c_2 \text{ (kPa)}$	$1.31 \times 10^2$	$1.99 \times 10^2$		
$c_3$	3.01	2.20		
$c_4$ (Pa)	$1.76 \times 10^{-9}$	$1.17 \times 10^{-9}$		
$c_5$	$1.43 \times 10^{-7}$	$1.80 \times 10^{-4}$		
$G_1^e$	1.1	1.24		
$G_2^{ar{e}}$	1.20	1.17		
$G_h^{ar{c}}$	1.07	1.11		
$G_h^{m}$	1.10	1.10		
$\alpha(\circ)$	30.09	50.00		

Table C.14: Material parameters for the sample 9

Parameters \ Regions	Anterior	Posterior
$c_1 \text{ (kPa)}$	$5.99 \times 10^2$	$1.79 \times 10^2$
$c_2 \text{ (kPa)}$	$8.42 \times 10^{1}$	$8.33 \times 10^2$
$c_3$	1.21	1.58
$c_4$ (Pa)	$3.55 \times 10^{-8}$	$4.70 \times 10^{-10}$
$c_5$	$1.56 \times 10^{-5}$	$8.56 \times 10^{-10}$
$G_1^e$	1.02	1.18
$G_2^{ar{e}}$	1.25	1.20
$G_h^{\overline{c}}$	1.10	1.11
$G_h^{\widetilde{m}}$	1.10	1.10
$\alpha(\circ)$	23.62	23.81

Table C.15: Material parameters for the sample 10

Parameters \ Regions	Anterior	Posterior
$c_1 \text{ (kPa)}$	$3.13 \times 10^2$	$3.06 \times 10^2$
$c_2$ (kPa)	$2.41 \times 10^2$	$4.40 \times 10^{2}$
$c_3$	1.32	3.40
$c_4$ (Pa)	$2.45 \times 10^{-14}$	$3.93 \times 10^{-9}$
$c_5$	$9.29 \times 10^{-11}$	$1.11 \times 10^{-16}$
$G_1^e$	1.20	1.37
$G_2^{ar{e}}$	1.20	1.05
$G_h^{ar{c}}$	1.10	1.08
$G_h^{\widetilde{m}}$	1.10	1.10
$\alpha(\circ)$	29.97	17.51

Table C.16: Material parameters for the sample 11

Parameters \ Regions	Anterior	Posterior
$c_1 \text{ (kPa)}$	$4.45 \times 10^2$	$2.82 \times 10^2$
$c_2 \text{ (kPa)}$	$2.14 \times 10^2$	$3.94 \times 10^2$
$c_3$	1.12	7.64
$c_4$ (Pa)	$4.03 \times 10^{-10}$	$4.05 \times 10^{-10}$
$c_5$	$6.50 \times 10^{-9}$	$2.00 \times 10^{-5}$
$G_1^e$	1.06	1.25
$G_2^{ar{e}}$	1.20	1.17
$G_h^{\overline{c}}$	1.09	1.10
$G_h^{\check{m}}$	1.10	1.10
$\alpha(\circ)$	18.47	28.71

# **BIBLIOGRAPHY**

# Bibliography

- American-Heart-Association, 2011. Heart disease and stroke statistics 2011 update: A report from the American heart association. Circulation Journal of the American Heart Association 123, e18—e209.
- Angouras, D., Sokolis, D.P., Dosios, T., Kostomitsopoulos, N., Boudoulas, H., Skalkeas, G., Karayannacos, P.E., 2000. Effect of impaired vasa vasorum flow on the structure and mechanics of the thoracic aorta: Implications for the pathogenesis of aortic dissection. European Journal of Cardio-Thoracic Surgery 17, 468–473.
- Avril, S., Badel, P., Duprey, A., 2010. Anisotropic and hyperelastic identification of *in vitro* human arteries from full-field optical measurements. Journal of Biomechanics 43, 2978–2985.
- Baek, S., Rajagopal, K., Humphrey, J., 2006. A theoretical model of enlarging intracranial fusiform aneurysms. Journal of Biomechanical Engineering 128, 142–149.
- Blondel, W.C.P.M., Didelon, J., Maurice, G., Carteaux, J.P., Wang, X., Stoltz, J.F., 2001. Investigation of 3-D mechanical properties of blood vessels using a new *in vitro* tests system: Results on sheep common carotid arteries. IEEE Transactions on Biomedical Engineering 48, 442–451.
- Cannon, C.P., O'Gara, P.T., 2006. Critical pathways in cardiovascular medicine. Lippincott Williams & Wilkins. second edition.
- Carew, T.E., Vaishnav, R.N., Patel, D.J., 1968. Compressibility of the arterial wall. Circulation Research 23, 61–68.
- Choi, G., Cheng, C., Wilson, N., Taylor, C., 2009. Methods for quantifying three-dimensional deformation of arteries due to pulsatile and nonpulsatile forces: implications for the design of stents and stent grafts. Annals of biomedical engineering 37, 14–33.
- Choudhury, N., Bouchot, O., Rouleau, L., Tremblay, D., Cartier, R., Butany, J., Mongrain, R., Leask, R.L., 2009. Local mechanical and structural properties of healthy and diseased human ascending aorta tissue. Cardiovascular Pathology 18, 83–91.
- Chuong, C., Fung, Y., 1983. Three-dimensional stress distribution in arteries. Journal of biomechanical engineering 105, 268–274.

- Chuong, C.J., Fung, Y.C., 1986. On residual stresses in arteries. Journal of Biomechanical Engineering 108, 189–192.
- Danpinid, A., Luo, J., Vappou, J., Terdtoon, P., Konofagou, E.E., 2010. *In vivo* characterization of the aortic wall stress-strain relationship. Ultrasonics 50, 654–665.
- Davidson, J., Hill, K., Alford, J., 1986. Developmental changes in collagen and elastin biosynthesis in the porcine aorta\* 1. Developmental Biology 118, 103–111.
- Draney, M.T., Arko, F.R., Alley, M.T., Markl, M., Herfkens, R.J., Pelc, N.J., Zarins, C.K., Taylor, C.A., 2004. Quantification of vessel wall motion and cyclic strain using cine phase contrast MRI: *In vivo* validation in the porcine aorta. Magnetic Resonance in Medicine 52, 286–295.
- Draney, M.T., Herfkens, R.J., Hughes, T.J.R., Pelc, N.J., Wedding, K.L., Zarins, C.K., Taylor, C.A., 2002. Quantification of vessel wall cyclic strain using cine phase contrast magnetic resonance imaging. Annals of Biomedical Engineering 30, 1033–1045.
- Everett, W.N., Shih, P., Humphrey, J.D., 2005. A bi-plane video-based system for studying the mechanics of arterial bifurcations. Experimental Mechanics 45, 377–382.
- Feigl, E.O., Peterson, L.H., Jones, A.W., 1963. Mechanical and chemical properties of arteries in experimental hypertension. Journal of Clinical Investigation 42, 1640–1647.
- Fischer, G., Llaurado, J., 1966. Collagen and elastin content in canine arteries selected from functionally different vascular beds. Circulation Research 19, 394–399.
- Fung, Y., 1993. Biomechanics: Mechanical Properties of Living Tissues. Springer. second edition.
- Fung, Y., Fronek, K., Patitucci, P., 1979. Pseudoelasticity of arteries and the choice of its mathematical expression. American Journal of Physiology Heart and Circulatory Physiology 237, H620–H631.
- Genovese, K., 2009. A video-optical system for time-resolved whole-body measurement on vascular segments. Optics and Lasers in Engineering 47, 995–1008.
- Goergen, C., Johnson, B., Greve, J., Taylor, C., Zarins, C., 2007. Increased anterior abdominal aortic wall motion: possible role in aneurysm pathogenesis and design of endovascular devices. Journal of Endovascular Therapy 14, 574–584.
- Groenink, M., Langerak, S.E., Vanbavel, E., van der Wall, E.E., Mulder, B.J.M., van der Wal, A.C., Spaan, J.A.E., 1999. The influence of aging and aortic stiffness on permanent dilation and breaking stress of the thoracic descending aorta. Cardiovascular Research 43, 471–480.
- Gundiah, N., Ratcliffe, M.B., Pruitt, L.A., 2007. Determination of strain energy function for arterial elastin: experiments using histology and mechanical tests. Journal of Biomechanics 40, 586–594.

- Guo, X., Kassab, G.S., 2004. Distribution of stress and strain along the porcine aorta and coronary arterial tree. American Journal of Physiology Heart and Circulatory Physiology 286, H2361–H2368.
- Guo, X., Lanir, Y., Kassab, G.S., 2007. Effect of osmolarity on the zero-stress state and mechanical properties of aorta. American Journal of Physiology Heart and Circulatory Physiology 293, H2328–H2334.
- Guo, X., Lu, X., Kassab, G.S., 2005. Transmural strain distribution in the blood vessel wall. American Journal of Physiology- Heart and Circulatory Physiology 288, H881–H886.
- Halloran, B., Davis, V., McManus, B., Lynch, T., Baxter, B., 1995. Localization of aortic disease is associated with intrinsic differences in aortic structure. Journal of Surgical Research 59, 17–22.
- Han, H.C., Fung, Y.C., 1995. Longitudinal strain of canine and porcine aortas. Journal of Biomechanics 28, 637–641.
- Haskett, D., Johnson, G., Zhou, A., Utzinger, U., Vande Geest, J., 2010. Microstructural and biomechanical alterations of the human aorta as a function of age and location. Biomechanics and Modeling in Mechanobiology 9, 725–736.
- He, C.M., Roach, M.R., 1994. The composition and mechanical properties of abdominal aortic aneurysms. Journal of vascular surgery 20, 6–13.
- Holzapfel, G., Weizsacker, H., 1998. Biomechanical behavior of the arterial wall and its numerical characterization. Computers in Biology and Medicine 28, 377–392.
- Holzapfel, G.A., Gasser, T.C., Ogden, R.W., 2000. A new constitutive framework for arterial wall mechanics and a comparative study of material models. Journal of elasticity 61, 1–48.
- Holzapfel, G.A., Gasser, T.C., Stadler, M., 2002. A structural model for the viscoelastic behavior of arterial walls: Continuum formulation and finite element analysis. European Journal of Mechanics-A/Solids 21, 441–463.
- Hsu, F.P.K., Liu, A.M.C., Downs, J., Rigamonti, D., Humphrey, J.D., 1995. A triplane video-based experimental system for studying axisymmetrically inflated biomembranes. IEEE Transactions on Biomedical Engineering 42, 442–450.
- Hu, J.J., Fossum, T.W., Miller, M.W., Xu, H., Liu, J.C., Humphrey, J.D., 2007. Biomechanics of the porcine basilar artery in hypertension. Annals of Biomedical Engineering 35, 19–29.
- Huang, Y., Guo, X., Kassab, G.S., 2006. Axial nonuniformity of geometric and mechanical properties of mouse aorta is increased during postnatal growth. American Journal of Physiology- Heart and Circulatory Physiology 290, H657–H664.
- Humphrey, J., 1995. Mechanics of the arterial wall: review and directions. Critical Reviews in Biomedical Engineering 23, 1–162.

- Humphrey, J., Rajagopal, K., 2002. A constrained mixture model for growth and remodeling of soft tissues. Mathematical Models and Methods in Applied Sciences 12, 407–430.
- Humphrey, J.D., 2001. Cardiovascular Solid Mechanics: Cells, Tissues, and Organs. Springer, New York.
- Humphrey, J.D., 2008. Vascular adaptation and mechanical homeostasis at tissue, cellular, and sub-cellular levels. Cell Biochemistry and Biophysics 50, 53–78.
- Humphrey, J.D., Kang, T., Sakarda, P., Anjanappa, M., 1993. Computer-aided vascular experimentation: A new electromechanical test system. Annals of Biomedical Engineering 21, 33–43.
- Iliopoulos, D.C., Deveja, R.P., Kritharis, E.P., Perrea, D., Sionis, G.D., Toutouzas, K., Stefanadis, C., Sokolis, D.P., 2009a. Regional and directional variations in the mechanical properties of ascending thoracic aortic aneurysms. Medical Engineering & Physics 31, 1–9.
- Iliopoulos, D.C., Kritharis, E.P., Giagini, A.T., Papadodima, S.A., Sokolis, D.P., 2009b. Ascending thoracic aortic aneurysms are associated with compositional remodeling and vessel stiffening but not weakening in age-matched subjects. The Journal of Thoracic and Cardiovascular Surgery 137, 101–109.
- Isselbacher, E., 2005. Thoracic and abdominal aortic aneurysms. Circulation 111, 816–828.
- Lally, C., Reid, A.J., Prendergast, P.J., 2004. Elastic behavior of porcine coronary artery tissue under uniaxial and equibiaxial tension. Annals of Biomedical Engineering 32, 1355–1364.
- Langewouters, G.J., Wesseling, K.H., Goedhard, W.J.A., 1984. The static elastic properties of 45 human thoracic and 20 abdominal aortas *in vitro* and the parameters of a new model. Journal of Biomechanics 17, 425–435.
- Lillie, M.A., Gosline, J.M., 2007. Mechanical properties of elastin along the thoracic aorta in the pig. Journal of Biomechanics 40, 2214–2221.
- Matsumoto, T., Goto, T., Furukawa, T., Sato, M., 2004. Residual stress and strain in the lamellar unit of the porcine aorta: experiment and analysis. Journal of biomechanics 37, 807–815.
- Menashi, S., Campa, J., Greenhalgh, R., Powell, J., 1987. Collagen in abdominal aortic aneurysm: typing, content, and degradation. Journal of vascular surgery: official publication, the Society for Vascular Surgery [and] International Society for Cardiovascular Surgery, North American Chapter 6, 578–582.
- O'Connell, M.K., Murthy, S., Phan, S., Xu, C., Buchanan, J.A., Spilker, R., Dalman, R.L., Zarins, C.K., Denk, W., Taylor, C.A., 2008. The three-dimensional micro-and nanostructure of the aortic medial lamellar unit measured using 3D confocal and electron microscopy imaging. Matrix Biology 27, 171–181.

- Okamoto, R.J., Wagenseil, J.E., DeLong, W.R., Peterson, S.J., Kouchoukos, N.T., Sundt III, T.M., 2002. Mechanical properties of dilated human ascending aorta. Annals of Biomedical Engineering 30, 624–635.
- Pandit, A., Lu, X., Wang, C., Kassab, G.S., 2005. Biaxial elastic material properties of porcine coronary media and adventitia. American Journal of Physiology - Heart and Circulatory Physiology 288, H2581–H2587.
- Participants, T.U.K.S.A.T., 2002. Long-term outcomes of immediate repair compared with surveillance of small abdominal aortic aneurysms. New England Journal of Medicine 346, 1445–1452.
- Patel, D., Janicki, J., Carew, T., 1969. Static anisotropic elastic properties of the aorta in living dogs. Circulation Research 25, 765–779.
- Peterson, L.H., Jensen, R.E., Parnell, J., 1960. Mechanical properties of arteries in vivo. Circulation Research 8, 622–639.
- van Prehn, J., van Herwaarden, J., Vincken, K., Verhagen, H., Moll, F., Bartels, L., 2009a. Asymmetric aortic expansion of the aneurysm neck: Analysis and visualization of shape changes with electrocardiogram-gated magnetic resonance imaging. Journal of Vascular Surgery 49, 1395–1402.
- van Prehn, J., Vincken, K.L., Sprinkhuizen, S.M., Viergever, M.A., van Keulen, J.W., van Herwaarden, J.A., Moll, F.L., Bartels, L.W., 2009b. Aortic pulsatile distention in young healthy volunteers is asymmetric: Analysis with ECG-gated MRI. European Journal of Vascular and Endovascular Surgery 37, 168–174.
- Purslow, P., 1983. Positional variations in fracture toughness, stiffness and strength of descending thoracic pig aorta. Journal of Biomechanics 16, 947–953.
- Rachev, A., Hayashi, K., 1999. Theoretical study of the effects of vascular smooth muscle contraction on strain and stress distributions in arteries. Annals of biomedical engineering 27, 459–468.
- Raghavan, M.L., Kratzberg, J., Castro de Tolosa, E.M., Hanaoka, M.M., Walker, P., da Silva, E.S., 2006. Regional distribution of wall thickness and failure properties of human abdominal aortic aneurysm. Journal of biomechanics 39, 3010–3016.
- Rezakhaniha, R., Fonck, E., Genoud, C., Stergiopulos, N., 2011. Role of elastin anisotropy in structural strain energy functions of arterial tissue. Biomechanics and Modeling in Mechanobiology 10, 599–611.
- Rhodin, J.A.G., 1980. Architecture of the vessel wall. In: Comprehensive Physiology.
- Roach, M.R., Song, S.H., 1994. Variations in strength of the porcine aorta as a function of location. Clinical and Investigative Medicine. Médecine clinique et experimentale 17, 308–318.

- Saravanan, U., Baek, S., Rajagopal, K.R., Humphrey, J.D., 2006. On the deformation of the circumflex coronary artery during inflation tests at constant length. Experimental Mechanics 46, 647–656.
- Schulze-Bauer, C.A.J., Morth, C., Holzapfel, G.A., 2003. Passive biaxial mechanical response of aged human iliac arteries. ASME Journal of Biomechanical Engineering 125, 395–406.
- Schulze-Bauer, C.A.J., Regitnig, P., Holzapfel, G.A., 2002. Mechanics of the human femoral adventitia including the high-pressure response. American Journal of Physiology Heart and Circulatory Physiology 282, H2427–H2440.
- Schwartz, S., Taljanovic, M., Smyth, S., O'Brien, M., Rogers, L., 2007. CT findings of rupture, impending rupture, and contained rupture of abdominal aortic aneurysms. American Journal of Roentgenology 188, W57–W62.
- Shadwick, R.E., 1999. Mechanical design in arteries. Journal of Experimental Biology 202, 3305–3313.
- Sokolis, D.P., 2007. Passive mechanical properties and structure of the aorta: segmental analysis. Acta Physiologica 190, 277–289.
- Spina, M., Garbisa, S., Hinnie, J., Hunter, J.C., Serafini-Fracassini, A., 1983. Age-related changes in composition and mechanical properties of the tunica media of the upper thoracic human aorta. Arteriosclerosis, Thrombosis, and Vascular Biology 3, 64–76.
- Stergiopulos, N., Vulliemoz, S., Rachev, A., Meister, J.J., Greenwald, S.E., 2001. Assessing the homogeneity of the elastic properties and composition of the pig aortic media. Journal of Vascular Research 38, 237–246.
- Struik, D.J., 1988. Lectures on Classical Differential Geometry. Dover Publications, Inc., New York. second edition.
- Takamizawa, K., Hayashi, K., 1987. Strain energy density function and uniform strain hypothesis for arterial mechanics. Journal of Biomechanics 20, 7–17.
- Thubrikar, M.J., 2007. Vascular Mechanics and Pathology. Springer.
- Thubrikar, M.J., Labrosse, M., Robicsek, F., Al-Soudi, J., Fowler, B., 2001. Mechanical properties of abdominal aortic aneurysm wall. Journal of Medical Engineering & Technology 25, 133–142.
- Thubrikar, M.J., Roskelley, S., Eppink, R., 1990. Study of stress concentration in the walls of the bovine coronary arterial branch. Journal of Biomechanics 23, 15–17.
- Tremblay, D., Cartier, R., Mongrain, R., Leask, R.L., 2010. Regional dependency of the vascular smooth muscle cell contribution to the mechanical properties of the pig ascending aortic tissue. Journal of Biomechanics 43, 2448–2451.
- Vaishnav, R., Young, J., Patel, D., 1973. Distribution of stresses and of strain-energy density through the wall thickness in a canine aortic segment. Circulation Research 32, 577–583.

- Valdez-Jasso, D., Haider, M.A., Banks, H.T., Bia Santana, D., German, Y.Z., Armentano, R.L., Olufsen, M.S., 2009. Analysis of viscoelastic wall properties in ovine arteries. IEEE Transaction on Biomedical Engineering 56, 210–219.
- Vande Geest, J.P., Sacks, M.S., Vorp, D.A., 2006. The effects of aneurysm on the biaxial mechanical behavior of human abdominal aorta. Journal of Biomechanics 39, 1324–1334.
- Vorp, D., Raghavan, M., Webster, M., 1998. Mechanical wall stress in abdominal aortic aneurysm: influence of diameter and asymmetry. Journal of Vascular Surgery 27, 632–639.
- Walker, J., Johnson, B., Fitz, W., Vaccaro, P., Smead, W., Cooperman, M., 1986. Abdominal aortic aneurysms in elderly patients. Vascular and Endovascular Surgery 20, 79–83.
- Wang, C., Garcia, M., Lu, X., Lanir, Y., Kassab, G.S., 2006. Three-dimensional mechanical properties of porcine coronary arteries: A validated two-layer model. American Journal of Physiology - Heart and Circulatory Physiology 291, H1200-H1209.
- Weizsacker, H.W., 1988. Isotropy and anisotropy of the arterial wall. Journal of Biomechanics 21, 447–487.
- Wells, S.M., Langille, B.L., Lee, J.M., Adamson, S.L., 1999. Determinants of mechanical properties in the developing ovine thoracic aorta. American Journal of Physiology Heart and Circulatory Physiology 277, H1385–H1391.
- Yin, F., Fung, Y., 1971. Mechanical properties of isolated mammalian ureteral segments. American Journal of Physiology 221, 1484–1493.
- Zeinali-Davarani, S., Raguin, L.G., Vorp, D.A., Baek, S., . Identification of in vivo material and geometric parameters of a human aorta: toward patient-specific modeling of abdominal aortic aneurysm. Biomechanics and Modeling in Mechanobiology , 1–11.
- Zhang, D., Eggleton, C.D., Arola, D.D., 2002. Evaluating the mechanical behavior of arterial tissue using digital image correlation. Experimental Mechanics 42, 409–416.
- Zhang, W., Herrera, C., Atluri, S.N., Kassab, G.S., 2005. The effect of longitudinal prestretch and radial constraint on the stress distribution in the vessel wall: A new hypothesis. Mechanics and Chemistry of Biosystems 2, 41–52.
- Zhou, J., Fung, Y.C., 1997. The degree of nonlinearity and anisotropy of blood vessel elasticity. Proceedings of the National Academy of Sciences 94, 14255–14260.
- Zou, Y., Zhang, Y., 2009. An experimental and theoretical study on the anisotropy of elastin network. Annals of Biomedical Engineering 37, 1572–1583.
- Zulliger, M., Rachev, A., Stergiopulos, N., 2004a. A constitutive formulation of arterial mechanics including vascular smooth muscle tone. American Journal of Physiology-Heart and Circulatory Physiology 287, H1335–H1343.

Zulliger, M.A., Fridez, P., Hayashi, K., Stergiopulos, N., 2004b. A strain energy function for arteries accounting for wall composition and structure. Journal of Biomechanics 37, 989–1000.